# THEORETICAL PREDICTION OF MATERIALS FOR EFFICIENT CONVERSION OF SOLAR ENERGY

by

PRANAB SARKER

Presented to the Faculty of the Graduate School of

The University of Texas at Arlington in Partial Fulfillment

of the Requirements

for the Degree of

DOCTOR OF PHILOSOPHY

THE UNIVERSITY OF TEXAS AT ARLINGTON

December 2016

Acknowledgements

I would like to express my deepest gratitude to my advisor, Professor Muhammad N. Huda for his guidance through the course of my study and research. In particular, I appreciate our weekly scientific discussions. Thanks to Professor Huda, I had the opportunity to attend different conferences and workshops.

I also would like to extend my thanks to my committee members, Professor Ali R. Koymen, Professor Alex Weiss, Professor Qiming Zhang, and Professor Suresh C. Sharma for their interests in my research work. Further, I am deeply indebted to Professor late A. K. Ray for being in my M.S. thesis committee.

I would also like to appreciate the members of our research groups for being very helpful throughout my research work. Their valuable suggestions during our regular research meetings have enriched my research experience.

Many thanks to, especially Professor Krishnan Rajeshwar and his group members with whom I have been collaborating since the beginning of my research career. Thanks to their useful experimental discussions and insights I learned a great deal.

I am very grateful to my parents and sibling for providing me an encouraging environment for my academic career. Last but not least, special thanks go to my wife, Baishakhi Biswas, for her continuous support, patience and care which helped me achieve this goal.

Finally, I would like to acknowledge the support from the National Renewable Energy Laboratory (NREL) and the U.S. Department of Energy (DOE). This research was conducted using the High Performance Computing Facility (HPCF) at the University of Texas at Arlington and at the Texas Advanced Computing Center (TACC).

November 17, 2015

Abstract

THEORETICAL PREDICTION OF MATERIALS FOR EFFICIENT CONVERSION OF SOLAR ENERGY

Pranab Sarker, PhD

The University of Texas at Arlington, 2015

Supervising Professor: Muhammad N. Huda

Our present work represents a systematic theoretical and computational research to find an affordable material for solar energy application using density functional theory (DFT) and post-DFT such as DFT+U and DFT-HSE06. Here, we predict a new photovoltaic material ($CuSnW_2O_8$) and a new photocatalyst ($ZnSnW_2O_8$). In addition, a new method for predicting the higher power conversion efficiency (PCE) optimized growth conditions will be presented.

It is well known that all physical properties are calculated once crystal structure is known. However, knowing crystal structure is extremely challenging and to date, there is no success has been claimed in the case of a material which is yet to exist. Under this circumstance, an existing method was adopted and extended to a great extent in predicting the crystal structures of new materials. This method invokes global optimization of possible candidates (motif structures) by means of DFT; the motif structures were obtained from existing structures in mineral database through an in-house algorithm. In addition to crystal prediction, determining suitable growth conditions before the material is synthesized is another challenge. To tackle this difficulty, a method has been developed, which includes chemical potential (Gibbs free energy) landscape analysis (CPL) as well as defects calculation.

The DFT-derived opto-electroinc properties and stability analysis of $CuSnW_2O_8$ show that it can be a perfect alternative of currently commercialized solar cell such as silicon (Si) and $CuIn_xGa_{1-x}Se_2$ (CIGS). It possesses band gaps of 1.25 eV (indirect) and 1.37 eV (direct), which were evaluated using the hybrid functional (HSE06) as a post-DFT method. The hole mobility of $CuSnW_2O_8$ was higher than that of Si. Further, optical absorption calculations demonstrate that $CuSnW_2O_8$ is a better absorber of sunlight than other promising solar cells, namely $Cu_2ZnSnS_4$ (CZTS) and CIGS. In addition, it exhibits rigorous thermodynamic stability comparable to $WO_3$. CPL analysis further revealed that $CuSnW_2O_8$ can be synthesized at flexible experimental growth conditions although the co-existence of at least one secondary phase is likely. The formation of Cu vacancies was found to be highly probable, even at Cu-rich growth condition, which could introduce p-type activity in $CuSnW_2O_8$.

Like $CuSnW_2O_8$, $ZnSnW_2O_8$ also exhibited primary features of the PEC process such as moderate band gap (~2.34 eV in DFT-HSE06), proper band edges positions, and higher stability. In addition, the higher optical absorption ability and dispersive band features embodied it a very attractive candidate for PEC process. According to CPL analysis, $ZnSnW_2O_8$ could also be synthesized at flexible experimental growth; however, at least two secondary phases were likely. Defects were found to be less probable at cationic-rich growth conditions in which the probable defects could be the Zn at Sn site and O-vacancy which give rise to n-type activity in $ZnSnW_2O_8$. Finally, the results presented here reveal that our predicted materials could be an effective choice for considering the synthesis of the next general solar cells.

Table of Contents

Acknowledgements ..... ii

Abstract ..... iii

List of Illustrations ..... x

List of Tables ..... xvii

Chapter 1 Introduction ..... 1

Chapter 2 Methodology ..... 7

2.1 Density Functional Theory ..... 7

2.1.1. Historical Background ..... 7

2.1.2. Foundation of Density Functional Theory ..... 9

2.1.2.1 Hohenberg-Kohn (HK) theorems ..... 10

2.2 Computational Techniques ..... 17

2.2.1. The Kohn-Sham (KS) Energy Functional ..... 18

2.2.2. Kohn-Sham (KS) Equations ..... 18

2.2.3. The Exchange Correlation Energy ..... 20

2.2.3.1. Local Density Approximation (LDA) ..... 21

2.2.3.2. Generalized Gradient Approximation (GGA) ..... 22

2.2.4. DFT+U ..... 22

2.2.5. DFT-Hybrid ..... 24

2.2.6. Projector Augmented Wave (PAW) Method ..... 25

2.2.6.1 Formalism ..... 27

2.2.6.2. Approximations ..... 30

2.2.6.3. Expectation Values in PAW ..... 31

2.2.7. Periodic Supercell Approximation ..... 31

2.2.7.1 Bloch's Theorem ..... 31

2.2.7.2 Plane Wave Basis Sets ..... 33
2.3 Computational Details ..... 35
2.4 Physical Properties ..... 36
2.4.1. Formation Enthalpy ..... 36
2.4.2. Cohesive Energy ..... 37
2.4.3. Fragmentation Energy ..... 37
2.4.4. Chemical Potential Landscape ..... 38
2.4.5. Defect Formation Energy ..... 39
2.4.6. Defect Concentration ..... 40
2.4.7. Conductivity Effective Mass ..... 40
2.4.8. Optical Absorption ..... 41
Chapter 3 Crystal Structure Prediction ..... 43
3.1 Introduction ..... 43
3.2 Computational Details ..... 43
3.3 Materials with $AgBiW_2O_8$ Stoichiometry ..... 44
3.3.1 $AgBiW_2O_8$ ..... 44
3.3.2 $CuBiW_2O_8$ ..... 44
3.4 $Sn_2O_3$ ..... 48
3.5 $Cu_2ZnSn(S_{1-x}Se_x)_4$ (CZTSSe) ..... 52
3.6 Conclusion ..... 54
Chapter 4 Thermodynamic Phase Stability and Optimal Growth Conditions ..... 55
4.1 Binary Compound: $SnO_x$ ..... 55
4.1.1. Introduction ..... 55
4.1.2. Computational Details ..... 56
4.1.3. Phase Stability and Optimal Growth Conditions ..... 58

4.1.4. Conclusion ..... 64
4.2. Ternary Compounds ..... 65
4.2.1 $CuBi_2O_4$ ..... 65
4.2.1.1 Introduction ..... 65
4.2.1.2 Computational Details ..... 65
4.2.1.3 Single-Phase stability, Defects, and Effective Growth Conditions ..... 65
4.2.1.4 Conclusion ..... 67
4.2.2 α-$SnWO_4$ ..... 68
4.2.2.1 Introduction ..... 68
4.2.1.2 Computational Details ..... 68
4.2.1.3 Single-Phase stability, Defects, and Effective Growth Conditions ..... 68
4.2.2.4 Conclusion ..... 70
4.3. Quaternary Compound: $Cu_2ZnSnS_4$ (CZTS) ..... 70
4.3.1. Introduction ..... 70
4.3.2. Computational Details ..... 72
4.3.3 Single-phase stability of CZTS ..... 74
4.3.4. Defects formation ..... 79
4.3.5. Role of intrinsic defects on single-phase stability of CZTS ..... 82
4.3.6. High efficient CZTS ..... 85
4.3.6.1 Determination of an effective growth condition ..... 85
4.3.6.2. Prediction of high efficiency pathway ..... 93
4.3.7. Conclusion ..... 96
4.4. Pentarnary Compound: $Cu_2ZnSn(S_{1-x}Se_x)$ (CZTSSe) ..... 97

4.4.1 Introduction ..... 97
4.4.2 Computational Details ..... 101
4.4.3 Single-phase stability ..... 101
4.4.4 Defect calculation ..... 106
4.4.5 High efficient growth conditions and alloy composition ..... 108
4.4.6. Conclusion ..... 114
Chapter 5 New PV Material ($CuSnW_2O_8$) ..... 115
5.1 Introduction ..... 115
5.2 Computational Details ..... 115
5.3 Crystal Structure Prediction ..... 117
5.4 Results ..... 118
5.4.1 Structural Properties ..... 118
5.4.2. Electronic Properties ..... 120
5.4.3. Optical Absorption ..... 122
5.4.4. Thermodynamic Stability ..... 124
5.4.4.1. Bonding Rigidity and Stability against Phase Segregation ..... 124
5.4.4.2. Single-Phase Stability ..... 125
5.4.5. Defects ..... 128
5.4.5.1 p-type activity ..... 129
5.4.5.2 Optical absorption with defects induced CTTO ..... 131
5.5. Conclusion ..... 132
Chapter 6 New PEC Material ($ZnSnW_2O_8$) ..... 134
6.1 Introduction ..... 134
6.2 Computational Details ..... 134
6.3 Crystal Structure Prediction ..... 135

6.4 Results ..... 135
6.4.1 Structural Properties ..... 135
6.4.2 Electronic Properties ..... 137
6.4.3 Optical Absorption ..... 137
6.4.4 Band Edge Positions ..... 139
6.4.5 Stability ..... 141
6.4.5.1. Bonding Rigidity and Stability against Phase Segregation ..... 141
6.4.5.2. Single-phase Stability and Effective Growth Conditions ..... 142
6.5 Conclusion ..... 144
Chapter 7 Conclusion ..... 146
Chapter 8 Future Research ..... 149
Appendix A Electronic Properties of $CuBi_2O_4$ and α-$SnWO_4$ ..... 151
Appendix B A Brief Study of $ANb_xO_y$ (A = Cu and Zn) ..... 154
References ..... 157
Biographical Information ..... 168

List of Illustrations

Figure 1.1 A flowchart of optimizing a solar absorber material for PV and PEC process. ..... 5

Figure 2.1 Correspondence between external potentials $vi$, associated ground states $\Psi 0, vi$ and ground state densities $\mathrm{n}0, vi$, in the case of non-degenerate ground states[25]. .....11

Figure 2.2 Flow-chart depicting a generic Kohn-Sham calculation. .....20

Figure 2.5 A closed N-atom ring. .....32

Figure 3.1 a) Crystal structure and b) XRD of $AgBiW_2O_8$. Two models: (left) ball-and-stick and (right) polyhedra of DFT derived crystal structure are presented in figure a. On the other hand, the two XRDs in figure b correspond to two samples of $AgBiW_2O_8$, which were synthesized in solution combustion synthesis (SCS) and solid state reaction (SSR) methods. .....45

Figure 3.2 a) The polyhedral model of probable crystal of $CuBiW_2O_8$: (left) $CuBi_2O_4$ - derived, Ref.[12] (middle), and (right) Ref. [112]. The K-mesh used for these structures are 13x9x11, 7x11x3, and 9x13x11, respectively. b) The calculated XRDs of three structures in figure a in conjunction with an experimental counterpart of a $CuBiW_2O_8$ sample that was recently synthesized through solid state reaction (SSR) method in Dr. Rajeshwar's lab at UTA. .....47

Figure 3.3 Evolution of different 'Motif Structures' of $Sn_2O_3$. 'nx' (n=2, 3, and 4) indicates that original structures, which had Z=1(Z = No. of formula unit) in the cell, were doubled, tripled, and quadrupled to form motif structures; structures having Z=2 in the cell were doubled only. .....50

Figure 3.4 Crystal structure of $Sn_2O_3$, derived from one of the $SnO_2$ (mp-560417) polymorphs. Sn1 and Sn2 atoms correspond to Sn (IV) and Sn (II) oxidation states in

$Sn_2O_3$, respectively. A 13x15x7 k-point sampling was used for $Sn_2O_3$ in DFT and DFT-D2 geometry optimization. .....50
Figure 3.5 Crystal structures of CZTSSe for three different alloy compositions: (a) x = 0.375, (b) x = 0.5, and (c) x = 0.625. A and B are the two reference points for each composition from which two different S-Se arrangement along positive 'c' can be viewed. .....53
Figure 4.1 The formation of different $SnO_x$ phases with respect to Sn and O growth conditions. Figure b is the magnified version of GZ1in Figure a. It is clear that all the phase transformations are occurring in the relatively O-poor and Sn-rich growth conditions. Figure c is also the magnified version of GZ1 while no vdW correction was incorporated. The broken line represents direct transition from SnO-to-$SnO_x$ or vice versa. .....62
Figure 4.2 The left figure represents the probability of forming different intrinsic defects in $CuBi_2O_4$ with respect to its single-phase growth region (see yellow bounded region at right figure); the yellow region in the left figure was achieved using the chemical potenial landscapre analysis (see ref.[17]). In the right figure, $\Delta\mu_\alpha$ (α = Cu, Bi, and O) axes correspond to growth conditions, from rich ($\Delta\mu_\alpha$ = 0 eV) to poor ($\Delta\mu_\alpha$ = formation enthalpy), of respective species. The values of A, B, and C in the figure are ($\Delta\mu_{cu}$ = -0.33 eV, $\Delta\mu_{Bi}$ = -0.96 eV, $\Delta\mu_O$ = -1.42 eV), ($\Delta\mu_{cu}$ = -1.74 eV, $\Delta\mu_{Bi}$ = -3.10 eV, $\Delta\mu_O$ = 0 eV), and ($\Delta\mu_{cu}$ = -1.60 eV, $\Delta\mu_{Bi}$ = -3.17 eV, $\Delta\mu_O$ = 0 eV), respectively. .....66
Figure 4.3 The defects formation energies and chemical potential landscape analysis of α-$SnWO_4$. The left figure represents the probability of forming different intrinsic defects in α-$SnWO_4$ with respect to its single-phase growth region (see yellow bounded region on the right figure). In the right figure, $\Delta\mu_\alpha$ (α = Sn, W, and O) axes correspond to growth conditions of respective species. .....69

Figure 4.4 Partial density of states of Cu 3d in CZTS with (green broken line; K-mesh: 15x15x9) and without U (red solid line; K-mesh:15x15x9), and HSE06-hybrid (black line; K-mesh: 5x5x3). Due high computational demand, hybrid-DFT calculation was performed with less number of K-points, hence some features of DOS at the valence band are under-estimated; however, the small contribution of Cu 3d empty band at the conduction band minimum is still visible. The extra correlation (exchange) added through U (HSE06-hybrid) lowers the contribution of Cu 3d in the bottom part of the conduction band that manifests the filled shell nature of Cu 3d band better than DFT-only calculations. Inset shows the magnified version of Cu 3d contributions at the bottom of the conduction band in three different methods. ....73

Figure 4.5 The triangles represent chemical potential landscapes for $Cu_2ZnSnS_4$ drawn at different Cu chemical potentials, $\Delta\mu_{Cu}$. Point P (figure (a)) and point Q (figure (d)), correspond to starting and end point growth conditions, respectively for stoichiometric $Cu_2ZnSnS_4$. Point S (figure (f)) corresponds to minimum $\Delta\mu_{Cu}$ at which $V_{Cu}$ becomes spontaneous. ....77

Figure 4.6 Various defect formation energies are shown. Point P, point Q, and point S correspond to three sets of $\Delta\mu_{\alpha}$ values in Figures 4.5a, 4.5d, and 4.5f, respectively. Point R is not shown in figure 4.5, chosen at $\Delta\mu_{Cu}$ = -0.78 eV. See table 4.2 for the values of $\Delta\mu_{\alpha}$ at P, Q, R, and S. ....79

Figure 4.7Chemical potential landscapes of non-stoichiometric $Cu_2ZnSnS_4$ that contain one $Cu_{Zn}$ defect per supercell (64 atoms). Grey bounded regions (GBR1 and GBR2) in the figures represent the occurrence of one secondary phase (ZnS or $Cu_2SnS_3$) along with $Cu_2ZnSnS_4$. ....84

Figure 4.8 Chemical potential landscapes of non-stoichiometric $Cu_2ZnSnS_4$ that contain a $V_{cu}$ defect per supercell (64 atoms). Grey bounded regions (GBR1) in the figures

represent the occurrence of one secondary phase (ZnS) along with $Cu_2ZnSnS_4$. .....89
Figure 4.9 The measured $V_{oc}$ and $J_{sc}$ for different CZTSSe samples ( 9.1% -12.6%). This figure was produced using data of $V_{oc}$ and $J_{sc}$ available in Ref. [121,197,201,202] $J_{sc}$ values have been multiplied by 100 for better visibility. It is obvious from the figure that the progression of $V_{oc}$ and $J_{sc}$ in most of CZTSSe samples is inverse to each other.....98
Figure 4.10 Chemical potential landscapes of CZTSSe for three different alloys: x = 0.375, 0.5 (a), and 0.625(c). Cu (poor) and S (rich) growth conditions are fixed on each plane in the triangles. Each yellow bounded region on those Cu-poor/Se-rich planes corresponds to single-phase growth zone of respective CZTSSe; area of which is commensurate with the respective CZTSSe's single-phase stability; the more Se in the composition, higher the stability. Figure (d) was drawn considering a single defect ($V_{Cu}$) in CZTSSe (x = 0.375) supercell (64 atoms). Unlike CZTS, the single-phase stability of CZTSSe remains intact even with the presence of a single-defect; other alloys exhibit similar feats which, however, were omitted here to avoid redundancy of figures.....104
Figure 4.11 Defects formation energies of various defects in CZTSSe for its different alloys. The probability of forming defects in the figure was determined with respect to single-phase growth zones in Figure 4.4.2(a-c). The defects which have formation energies higher than 3 eV were not shown. From the figure, it is obvious that defects are evident in the single-phase CZTSSe, no matter the growth condition is. .....106
Figure 4.12 The formation of CZTSSe and its different secondary phases with respect to S ($\Delta\mu_S$) and Se ($\Delta\mu_{Se}$) growth conditions while keeping cationic growth conditions fixed: (a) all cations-rich and (b) all cations-poor. The diagonal line represents stable formation

of CZTSSe while all other arrow ended lines in (a) indicate the formation of secondary phases. Each arrow corresponding to inequality sign in Equation (4.27) indicates unbound $\Delta\mu_{S/Se}$ poor value of respective phase. The unbounded values were chosen to extrapolate the co-existence of secondary phases (intersecting points with diagonal) with CZTSSe at given growth conditions for the primary phase. The single-phase of CZTSSe was indicated by the broken line. Figure (b) represents a high efficient growth conditions at which no secondary phases form. .....109

Figure 4.13 Anionic defect formation energies of CZTSSe for three different composition alloys (x = 0.375, 0.5, and 0.625) at fixed cationic growth conditions. All three cationic growth conditions $\Delta\mu_{\alpha}$ (α = Cu, Zn, and Sn) were fixed as equally poor as to produce $\Delta H$ ($V_{S/Se}$) ≥ 1 eV in Equation 4.27a-c. The poor values of $\Delta\mu_{Se}$ and $\Delta\mu_{S}$ at S-rich and Se-rich growth conditions respectively are presented in Table 4.4. P, Q, and R the optimal values to avoid anionic defects for each x.....112

Figure 5.1 Evolution of motif structures from existing structures. “nx” (n=2 and 4) indicates that original structures were doubled and quadrupled to form motif structures. "⊗” corresponds to all possible different arrangements among the cations in a unit cell.....117

Figure 5.2 Theoretical XRDs of three DFT+U possible structures of $CuSnW_2O_8$. .....118

Figure 5.3 Crystal structure of $CuSnW_2O_8$: (top) ball-and-stick model and (bottom) polyhedral model.....120

Figure 5.4 The DFT+U and DFT-HSE06: a) electronic band structures and b) projector density of states (p-DOS). The Fermi level was set to 0 eV. The overall features of band structures and p-DOS in both methods were found to be similar except band gaps which can be attributed to the difference in adopted empirical corrections in two different post-DFT methods. .....121

Figure 5.5 DFT+U optical absorption spectrum: red, green, and blue lines represent the absorption of CTTO, CZTS, and CIGS, respectively the used K-meshes for those were 7×13×15, 9×9×5, and 13×13×7, respectively. .....123
Figure 5.6 Chemical potential landscape of CTTO in two different Cu growth conditions: (a) Cu-rich and (b) Cu-poor. Yellow-bounded regions represent the range of growth conditions of all chemical species to form CTTO-$WO_3$, as well as the stability of this mixed phase: the larger the spread, the higher the stability. .....127
Figure 5.7 The DFT+U defects formation energy in CTTO at two different growth conditions: Cu-rich and Cu-poor. .....129
Figure 5.8 Band structures of three defects: (a) $V_{Cu}$, (b) $Sn_{Cu}$, and (c) $Sn_{Cu}$+$V_{Cu}$-induced CTTO. .....130
Figure 5.9 The DFT+U optical absorption spectra of pristine and defect-induced CTTO. It is seen that the absorption spectra of pristine and defects-induced CTTO have similar features except the very early absorption in $Sn_{Cu}$-CTTO. The first two early rises in the $Sn_{Cu}$ absorption spectrum correspond to the transition between occupied and unoccupied states around the conduction band edge, which do not contribute to PV efficiency. A 7×11×13 K- point sampling was used to produce the absorption spectrum of pristine CTTO, while it was 5×5×5 for those of defect-induced CTTO.....131
Figure 6.1 The DFT+U optimized crystal structure of $ZnSnW_2O_8$. Figure a represents two different models of the unit cell of 24 atoms: (left) ball-and-stick and (right) polyhedra. A 2x1x2 supercell of 96 atoms in the polyhedra model is shown in figure b, which contains hollows in the long-ranged periodicity. .....136
Figure 6.2 The DFT+U and DFT-HSE06: a) electronic band structures and b) projector density of states (p-DOS). The Fermi level was set to 0 eV. The overall features of band structures and p-DOS in both methods were found to be similar except band gaps which

can be attributed to the difference in adopted empirical corrections in two different post-DFT methods. ....138
Figure 6.3 The DFT+U optical absorption spectrum of pristine-$ZnSnW_2O_8$. ....139
Figure 6.4 The relative band edges positions of $ZnSnW_2O_8$ and different metal-tungstates with respect to $WO_3$. ....140
Figure 6.5 Chemical potential landscape of $ZnSnW_2O_8$ in two different W growth conditions: (a) W-rich and (b) W-poor. Yellow-bounded region represents a growth region which can be suitable for synthesizing $ZnSnW_2O_8$ with least detrimental defects. However, $ZnWO_4$ and ZnO are highly probable to be co-existed with the primary phase in this region. ....143

List of Tables

Table 3.1 A comparison between DFT+U energetics, volumes, and lattice constants of three probable structures of $CuBiW_2O_8$.....48

Table 3.2 vdW-DFT predicted energies, volumes, and lattice parameters of few most probable structures of $Sn_2O_3$. The formation enthalpies, $\Delta Hf$ were calculated with respect to bulk Sn and molecular $O_2$ phases following the method described in reference.[12]The '(n = an integer)' in the fourth column represents the ranking of the corresponding free energy; the stability of each probable structures runs from most to lowest with the ascending order of n. .....51

Table 4.1 A comparison of structural and band gap attributes of SnO between calculated (with vdW correction) and experimental results.....57

Table 4.2 The values of chemical potentials for cations, $\Delta\mu_\alpha$ ($\alpha$ = Cu, Zn, Sn, and S), at points P, Q, R, and S with respect to figure 4.5.....80

Table 4.3 The values of $\Delta\mu_\alpha$ ($\alpha$ = Cu, Zn, Sn, and S) at different points shown in Figures 4.7 and 4.8.....92

Table 4.4 Defect formation energies at all cations-equally-poor and anions rich/richer growth conditions. .....111

Table 5.1 DFT+U formation enthalpies ($\Delta H_f$) and volumes of few most probable structures for $CuSnW_2O_8$. The value of $\Delta H_f$ presented here for StructurePredictor (SP) structure is the lowest among all SP generated structures. All $\Delta H_f$ were calculated following the reference.[12].....119

# Chapter 1

## Introduction

Accelerating the discovery of new functional materials in the proliferation of novel technologies such as solar energy, high-$T_c$ superconductivity, and spintronics has been an imperative but extremely challenging task to the scientific community. The traditional experiment-only way of developing new materials is neither cost- nor time-effective, and often requires a stroke of luck.[1] In contrast, systematic and successful theoretical predictions in this regard not only do the discovery faster, but also at minimal cost. For my dissertation, as a computational condensed matter physicist, I embrace the challenge to discover a new affordable material for solar energy application.

Even though all cultural, scientific and technological advancements so far have been empowered by fossil fuels - oil, coal, and natural gas - directly or indirectly, the continuous emission of greenhouse gases, while burning fossil fuels, in the atmosphere, most notably $CO_2$, have put our habitable earth into a vulnerable position. Therefore, for environmental remediation, the immediae need to have an affordable alternative of it is irrefutable at present days. While other approaches such as wind and ocean energies, and neuclear power plants incur either higher cost or environmental safety concerns, converting the inexhaustible solar energy into current (PV approach) or into fuel such as hydrogen (PEC approach) have been unanimously accepted as the most pragmatic ways of replacing the use of fossil fuels. However, both of these conversion processes require semiconductors with specific characteristics for a cost-effective, eco-friendly, and efficient conversion process, which neither exists in nature nor has been engineered successfully thus far. To solve this issue, the discovery of the new suitable semiconductors has been essential, which has been pursued in the current dissertation research.

Note that it is possible to easily make more than a hundred of millions binary, ternary, and quaternary compounds out of all the materials available in the periodic table. Predicting a new solar absorber material out of those numerous combination is not only extremely challenging but also an arduous task, and a systemic approach therefore is must-needed. An efficient approach in this regard is 'Materials by Design' which itself has different variations such as inverse band structure methods,[2] and data mining;[1,3,4] both of these methods screen out possible candidates of the prospective material through classical approaches such as genetic algorithm and data mining. Therefore, the successes in those predictions are less guaranteed. Here, we attempt a different approach that takes a selected compound composition as an input and then determines its structural and opto-electronic properties, stability, and optimal growth conditions through density functional theory. Since the efficiency of this method depends on the given input, an educated input based on quantum mechanical knowledge is needed for the best performance. In my dissertation, it will be demonstrated that a new material discovery can be faster and cost-effective if the input compound is chosen carefully.

To design (select) an optimal compound (input) one must pay attention to the targeted properties such as band gap and higher stability, for the considered application. For sustainable and affordable PV/PEC process the first two targeted characteristics of a material are to be non-toxic and earth abundant semiconductors. Further, those semiconductors must possess moderate band gaps (1-1.5 eV for PV[5] and 1.8-2.2 eV for PEC processes), suitable band edge position (for PEC processes only), higher optical absorption ability, and higher stability. In addition to those, the presence of p-type activity and higher carrier mobility in a semiconductor is desirable for maximum efficiency. Taking all these criteria into consideration we design a solar material, expecting to have all the aforementioned characteristics in that material. In designing new materials, we focus on

W-based oxides in the form of $ABW_2O_8$. Three reasons for pursuing a W-based oxide as a suitable solar material are the following: i) non-toxicity and Earth abundance of both W and O, ii) relatively delocalized nature of W 5d (compared to 3d) orbital around the conduction band edge in W-based oxides—e.g., $WO_3$, $CuWO_4$, $Bi_2W_2O_9$, and so on—demonstrating strong sunlight absorption in those materials, and iii) robust stability[6] of those oxides even at different aqueous media over a relatively wide $P^H$ ($P^H$ <8) range. Despite the fact that γ-$WO_3$ is the most stable W oxide, it possesses a band gap of 2.70 eV, which is higher than what is required for PV/PEC process. However, several pathways can be taken to reduce the larger band gap of a binary oxide. For example, suitable cations can be alloyed with γ-$WO_3$,[7–12] which is pursued in the present work. The selection of two other cations to form a desired W-based quaternary oxide was accomplished through three steps: i) choose elements that conform to the needs of a cost-effective and ecofriendly solar energy application, ii) keep elements whose atomic orbital contributions to band gap reduction in their respective $WO_3$-derived phases are known, and finally, iii) select those elements that provide beneficial attributes such as p-type activity and higher carrier mobility for improved solar-to-current/hydrogen conversion. A quaternary W-based oxide predicted through the method above is expected to have the desired electronic properties as well as higher stability like $WO_3$.

Once the new material is designed, my work encompasses (i) predicting crystal structures, (ii) determination of electronic and optical properties, (iii) carrying out static stability analysis at thermodynamic equilibrium conditions. Crystal structure which uniquely determines all physical properties of a material is needed to be predicted accurately at the very beginning. The successful determination of crystal structure of the predicted mateial ensures the success in predicting its optimal PV or photocatalytic attributes. However, theoretical crystal structure prediction is termed as one of the

"continuing scandals" in the physical sciences.[13] Crystal structure prediction was believed fundamentally impossible like predicting earthquake until 2003 albeit the chemical composition or stoichiometry are known [14]. With the advent of high efficient computers and advancement of computational physics, it is possible to predict stable atomic arrangement of a new material, without even being synthesized, quantitatively with minimal time and cost[115]. There are many systematic approaches[16] to predict crystal structure successfully have been devised so far, however, no exemplary success of it to date is citable especially, for the materials which are yet to be synthesized. Most of the approaches are either empirical, biased to historical knowledge such as data mining approach or limited to symmetrical geometry of structures. One of the approaches that is non-empirical, not bounded only on historical knowledge, and even applicable to asymmetric structures is to explicit calculation of the (free) energy of all possible structures using "computation optimization". However, this approach often requires having a large set of all possible structures for optimization to determine the thermodynamically stable crystal structure of a material successfully. Note that the structures having exact stoichiometry and atomic coordination but differ, at least, either in atomic arrangement or in lattice parameters are treated as possible structures. In our present work, we embrace "computation optimization" approach using DFT to predict the thermodynamically stable crystal structure of a new material with desired elemental component. A credible crystal structure determination of a new material may require DFT optimization of all possible structures that the material can possess. We define each possible crystal structures as 'Motif Structure' of the predicted material. All these motif structures can be found through a comprehensive mineral database search considering topological symmetry, covalent and ionic radii proximity of atoms, coordination numbers, oxidation states of the ions, etc. Hence, our set of possible or motif structures

encompasses an unbiased, systematic, and more general scheme to predict crystal structure. A major part of our present work is to determine the possible stable structure of the predicted material that had been accomplished with the help of database search methodology as outlined here within the context of DFT. The predicted structures are then exposed to density of states (DOS), band structure, optical absorption calculations, and further analysis, including stability, necessary to quantify PV/photocatalytic attributes. If the newly designed material satisfies all the required criteria, we predict that one as our desired material. Otherwise, a new search of A or/and B would be taken as input and the optimization process as shown in Figure 1.1 would go on and on until the desired material is found. Following the approach mentioned above we have predicted $CuSnW_2O_8$ and $ZnSnW_2O_8$ as our predicted PV material and photocatalyst, respectively. The justification of selecting cations A and B in respective $ABW_2O_8$ will be given in Chapters 5 and 7.

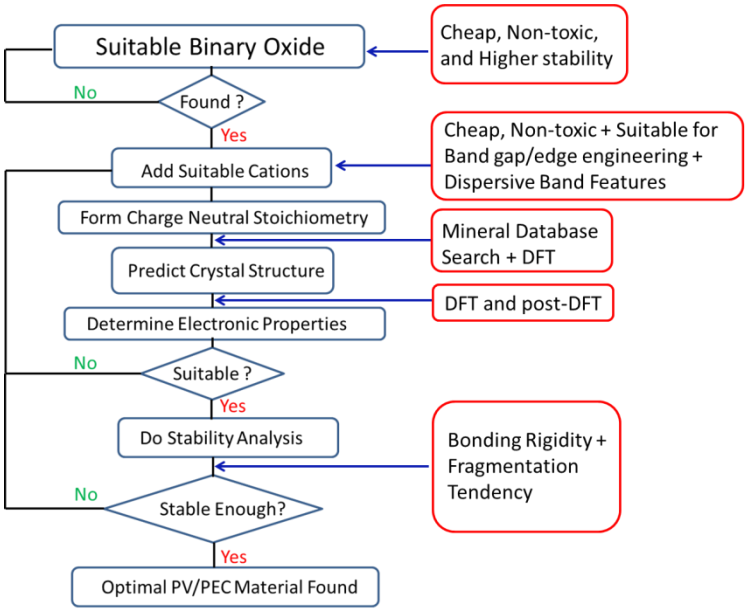


Figure 1.1 A flowchart of optimizing a solar absorber material for PV and PEC process.

Soon after the new affordable material is predicted, the next challenge is to synthesize it. During the synthesis process, defects are inherent in a material. Further, unwanted phases may co-exist with primary material if the growth conditions are not well chosen. These defects/mixed-phases enhance or degrade the materials' properties. A suitable choice of growth conditions during the synthesis process can maximize the efficiency of the material of interest; however, determining such a high efficient growth conditions often involves trial-and-error. An effective prediction in this regard would not only do ensure the higher efficiency of the desired material, but also save time and cost. To tackle the second challenge, I have developed a method[17] using chemical potential analysis that predicts an effective growth condition to achieve relatively higher PV/photocatalytic efficiency from the predicted material.

# Chapter 2

# Methodology

## 2.1 Density Functional Theory

One of the basic problems in theoretical physics and chemistry is the description of the structure and dynamics of many-electron systems. Density functional theory (DFT) is an extremely successful quantum mechanical modeling method used in physics and chemistry to investigate the electronic structure (principally the ground state) of many-body systems, in particular atoms, molecules, and the condensed phases. The main idea of DFT is to describe an interacting system of fermions via its density and not via its many-body wave function. For N electrons in a solid, which obey the Pauli principle and repulse each other via the Coulomb potential, the basic variable of the system depends only on three -- the spatial coordinates x, y, and z -- rather than 3N degrees of freedom. With this theory, the ground state properties of a many-electron system can be determined by using functionals, i.e. functions of another function, which in this case is the spatially dependent electron density, $n[\psi(\vec{r})]$. Hence the name density functional theory comes from the use of functionals of the electron density. DFT is among the most popular and versatile methods available in condensed-matter physics, computational physics, and computational chemistry. Its applicability ranges from atoms, molecules and solids to nuclei and quantum and classical fluids.

### *2.1.1. Historical Background*

Thomas and Fermi[18,19] were the first [20] to contemplate a model for the electron many-body problem based uniquely on the electron density $n(\vec{r})$. The basic idea of the theory is to find the energy of electrons in a spatially uniform potential as a function of density. Then one uses this function of the density locally even when the electrons are in

the presence of an external potential. The Thomas-Fermi energy functional is composed of three terms,

$$E^{TF}[n] = T^{TF}[n] + \int n(\vec{r}) v_{ext}(\vec{r}) d\vec{r} + \frac{1}{2} \iint d\vec{r} d\vec{r}' \frac{e^2 n(\vec{r}) n(\vec{r}')}{|\vec{r} - \vec{r}'|} \tag{2.1}$$

The first term in Equation (2.1) is the electronic kinetic energy associated with a system of non-interacting electrons in a homogeneous electron gas. This form is obtained by integrating the kinetic energy density of a homogeneous electron gas [21,22] $t_0[n]$,

$$T^{TF}[n] = \int t_0[n(\vec{r})] d\vec{r} \tag{2.2}$$

where $t_0[n(\vec{r})]$ is obtained by summing all of the free-electron energy states $\varepsilon = \frac{\hbar^2 k^2}{2m}$ up to the Fermi wave vector $k_F = [3\pi^2 n(\vec{r})]^{1/3}$. Finally,

$$T^{TF}[n] = \int \frac{\hbar^2}{2m} \frac{3}{5} (3\pi^2)^{2/3} n(\vec{r})^{5/3} (\vec{r}) \tag{2.3}$$

The second term is the classical electrostatic energy of attraction between the nuclei and the electrons, where $v_{ext}(\vec{r})$ is the static Coulomb potential arising from the nuclei,

$$v_{ext}(\vec{r}) = -\sum_{j=1}^{N} \frac{e^2 Z_j}{|\vec{r} - \vec{R}_j|} \tag{2.4}$$

Finally, the third term represents the electron-electron interactions of the system approximated by the classical Coulomb repulsion between electrons, known as the Hartree energy.

To obtain the ground state density and energy of a system, the Thomas-Fermi energy functional must be minimized subject to the constraint that the number of electrons is conserved. This type of constrained minimization problem, which occurs frequently within many-body methods, can be performed using the technique of Lagrange

multipliers. In general terms, the minimization of a functional $F[f]$, subject to the constraint $C[f]$, leads to the following stationary condition,

$$\delta\,(F[f] - \mu C[f]) = 0 \tag{2.5}$$

Where $\mu$ is a constant known as the Lagrange multiplier. Minimizing the above equation leads to the solution of the corresponding Euler equation,

$$\delta F[f]/\delta f - \mu\,\delta C[f]/\delta f = 0 \tag{2.6}$$

When Thomas-Fermi energy functional incorporates the exchange term of the following form,

$$\varepsilon_{xc} = -\int \frac{3}{4}\left(\frac{3}{\pi}\right)^{1/3} e^2\, n(\vec{r})^{4/3}(\vec{r}) \tag{2.7}$$

the theory is called Thomas-Fermi-Dirac [23].

*2.1.2. Foundation of Density Functional Theory*

Due to the severe shortcomings of Thomas-Fermi method [23] such as inability to predict molecular binding, failure to demonstrate the electrons' distribution into different shells, better accuracy only for nearly uniform charge distribution etc., it was hard to be imagined that an exact theory could be based on the density. However, almost forty years later, Hohenberg and Kohn proved in a seminal paper[24] that this was indeed possible. In two remarkably powerful theorems they formally established the electron density as the central quantity describing electron interactions contained in a many-electron wave function, and so devised the formally exact ground state method known as density functional theory (DFT). Hence, the starting point of any discussion of DFT is the Hohenberg-Kohn (HK) theorems.

2.1.2.1 Hohenberg-Kohn (HK) theorems

The Hohenberg-Kohn theorems relate to any system consisting of electrons moving under the influence of an external potential $v_{ext}(\boldsymbol{r})$. Stated simply they are as follows:

***Theorem 1:*** *The external potential* $v_{ext}(\boldsymbol{r})$ *, and hence the total energy, is a unique functional of the electron density. In other words, the electron density determines the external potential (to within an additive constant) uniquely.*

**Proof:**

In the original Hohenberg-Kohn paper, this theorem is proven for densities with non-degenerate ground states [8]. This extension of this proof to degenerate ground states is also valid. The proof in both cases is elementary, and by contradiction. Let us first consider non-degenerate case.

**Non-degenerate Ground States**

Let us define the set of all external potentials $v_{ext}(\boldsymbol{r})$, $\mathbb{V}$ such that

$$\mathbb{V} = \left\{ v_{ext}(\boldsymbol{r}) \;\middle|\; \begin{array}{c} with:\ v_{ext}(\boldsymbol{r})\ multiplicative\ , \\ corresponding\ \ |\ \Psi_0 > exists\ and \\ is\ non-degenerate, v'_{ext}(\boldsymbol{r}) \neq v_{ext}(\boldsymbol{r}) + const. \end{array} \right\} \tag{2.8}$$

for which Schrödinger equation

$$\hat{H}\ |\ \Psi_k > \ = \ E_k\ |\ \Psi_k > \tag{2.9}$$

leads to a non-degenerate eigenstate $|\ \Psi_0 >$.

The set of all external potentials $v_{ext}(\boldsymbol{r})$, $\mathbb{V}$ leads to a set non-degenerate ground eigenstates $|\ \Psi_0 >$, $\mathcal{G}$ such that

$$\mathcal{G} = \left\{ |\ \Psi_0 > \;\middle|\; \begin{array}{c} with:\ \ |\ \Psi_0 > ground\ state\ corresponding\ to \\ one\ element\ of\ \mathbb{V}\ , \\ |\ \Psi'_0 > \neq e^{i\varphi}\ |\ \Psi_0 > \\ with\ \varphi\ being\ some\ global\ phase \end{array} \right\} \tag{2.10}$$

And the set $\mathcal{N}$ of all ground state densities obtained from some element of $\mathcal{G}$ is defined as

$$\mathcal{N} = \{ \mathrm{n}_0 \mid \mathrm{n}_0(\boldsymbol{r}) = < \Psi_0 \mid \hat{n}(\boldsymbol{r}) \mid \Psi_0 >, \ \mid \Psi_0 > \in G \} \tag{2.11}$$

Where, $\mathrm{n}_0(\boldsymbol{r}) = < \Psi_0 \mid \hat{n}(\boldsymbol{r}) \mid \Psi_0 >$

$$= N \sum_{\sigma_1,\ldots,\sigma_N} \int d^3 r_1 \ldots\ldots d^3 r_N \ \mid (\boldsymbol{r_1 \sigma_1}, \boldsymbol{r_2 \sigma_2}, \ldots\ldots, \boldsymbol{r_N \sigma_N} \mid \Psi_0 >|^2$$

Correspondence between the elements of $\mathbb{V}$, $\mathcal{G}$ and $\mathcal{N}$ can be thought as the following two maps (shown in Figure 2.1)

**A:** $\mathbb{V} \rightarrow \boldsymbol{\mathcal{G}}$

and **B:** $\boldsymbol{\mathcal{G}} \rightarrow \boldsymbol{\mathcal{N}}$

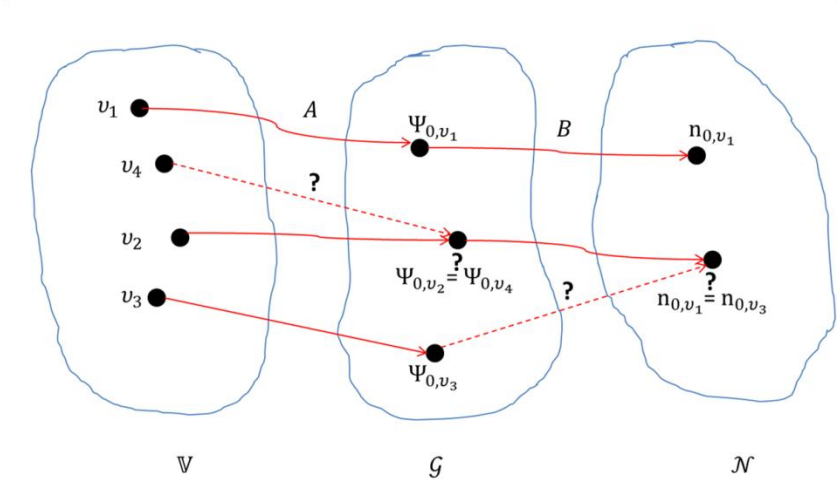


Figure 2.1 Correspondence between external potentials $v_i$, associated ground states $\Psi_{0,v_i}$ and ground state densities $\mathrm{n}_{0,v_i}$, in the case of non-degenerate ground states[25].

It is sufficient to show that map **A** and map **B** are unique in order to proof first Hohenberg-Kohn theorem in the non-degenerate case.

The proof of uniqueness for map **A** consists in demonstrating the validity of the following two statements:

(i) For given $v_{ext}(\boldsymbol{r})$ there exists only one $|\Psi_0>$ in $\boldsymbol{\mathcal{G}}$, i.e. there is no $v_{ext}(\boldsymbol{r})$ which is mapped onto two elements of $\boldsymbol{\mathcal{G}}$. This statement is trivial due to the restriction to non-degenerate ground states.

(ii) There is no $|\Psi_0>$ which is simultaneously ground state for two different potentials $v_{ext}(r)$ and $v'_{ext}(r)$ which differ by more than a constant. The standard proof of this statement is based on *a reductio ad absurdum*[25].

Let us assume that $|\Psi_0>$ is simultaneously ground state for two different potential $v_{ext}(\boldsymbol{r})$ and $v'_{ext}(\boldsymbol{r}) \neq v_{ext}(\boldsymbol{r}) + const$ thus satisfies two Schrödinger equations,

$$\hat{H}\,|\Psi_0> = \left[\hat{T} + \hat{V}_{ext} + \hat{W}\right]|\Psi_0> \;=\; E_0\,|\Psi_0> \tag{2.12}$$

$$\hat{H}'\,|\Psi_0> = \left[\hat{T} + \hat{V}'_{ext} + \hat{W}\right]|\Psi_0> \;=\; E'_0\,|\Psi_0> \tag{2.13}$$

$\hat{T}$= kinetic energy operator

$$\hat{T} = \sum_{i=1}^{N} \frac{(-i\hbar\nabla_i)^2}{2m} \tag{2.14}$$

$\widehat{V}_{ext}$ is the operator that accounts the interaction of the particles with external sources characterized by a given, time independent potential $v_{ext}(\boldsymbol{r})$

$$\widehat{V}_{ext} = \sum_{i=1}^{N} v_{ext}(\boldsymbol{r_i}) = \int d^3r v_{ext}(\boldsymbol{r_i})\,\widehat{n}(\boldsymbol{r}) \tag{2.15}$$

In practical applications $v_{ext}(\boldsymbol{r})$ is given by

$$\hat{V}_{n-e} = -\sum_{\alpha=1}^{k}\sum_{i=1}^{N} \frac{Z_\alpha e^2}{|\boldsymbol{R}_\alpha - \boldsymbol{r}_i|} \tag{2.16}$$

Where $\boldsymbol{R}_\alpha$ denotes the Cartesian coordinates of nucleus $\alpha$ and $\boldsymbol{r}_i$ denotes the position of electron $i$

$\widehat{W}$= a particle-particle interaction operator

$$=\sum_{i,j=1}^{n} w(\boldsymbol{r_i}, \boldsymbol{r_j}) = \frac{1}{2}\sum_{i,j=1;i\neq j}^{n} w(\boldsymbol{r_i}, \boldsymbol{r_j}) \tag{2.17}$$

The basic DFT formalism is independent of the form of $w$ keeping it same throughout discussion.

The subtraction of Equation (2.12) and Equation (2.13) yields

$$\left[\hat{V}_{ext} - \hat{V}'_{ext}\right] | \Psi_0 > \; = [E_0 - E_0'] | \Psi_0 > \tag{2.18}$$

The wavefunction $\Psi_0(\boldsymbol{r_1\sigma_1}, \ldots\ldots, \boldsymbol{r_N\sigma_N})$ does not vanish for all points $\boldsymbol{r_i}$. Thus, one obtains

$$\sum_{i=1}^{N} [v_{ext}(\boldsymbol{r_i}) - v'_{ext}(\boldsymbol{r_i})] = E_0 - E_0' \tag{2.19}$$

Keeping N −1 of the $\boldsymbol{r_i}$ fixed, and letting the remaining position vary, Eq. (2.15) leads to a contradiction (as the right-hand side is constant, while $v_{ext}(\boldsymbol{r})$ and $v'_{ext}(\boldsymbol{r})$ are assumed to differ by more than a constant). Consequently, the map **A** is unique: there is a one-to-one correspondence between the potential $v_{ext}(\boldsymbol{r})$ and the resulting ground state$| \Psi_0 >$ (up to some additive constant in $v_{ext}(\boldsymbol{r})$).

In order to demonstrate the uniqueness of **B**, one has to show that two different $| \Psi_0 > \in G$ cannot lead to the same ground state density $n_0$. The proof again relies on *reductio ad absurdum*.

Assume that $n_0$ is obtained from two different elements of $| \Psi_0 >$ and $| \Psi'_0 >$. From the Ritz variational principle one then obtains an inequality for the ground state energy,

$$E_0 = < \Psi_0 | \hat{H} | \Psi_0 > \; < \; < \Psi'_0 | \hat{H} | \Psi'_0 > \tag{2.20}$$

$$E_0 < \; < \Psi'_0 | \hat{H} | \Psi'_0 > \tag{2.21}$$

Where $\hat{H}$ is the unique Hamiltonian leading to $|\Psi_0>$ (due to the uniqueness of map A) and the strict inequality originates from the non-degeneracy $|\Psi_0>$ and $|\Psi'_0>$. After manipulation

$$E_0 < \quad <\Psi'_0|\hat{H}'|\Psi'_0> + <\Psi'_0|\hat{H}-\hat{H}'|\Psi'_0> \tag{2.22}$$

Or,
$$E_0 < \quad E'_0 + <\Psi'_0|\left(\hat{T}+\hat{V}_{ext}\right)-\left(\hat{T}+\hat{V}'_{ext}\right)|\Psi'_0> \tag{2.23}$$

Or,
$$E_0 < \quad E'_0 + <\Psi'_0|\ \hat{V}_{ext}-\hat{V}'_{ext}|\Psi'_0> \tag{2.24}$$

Or,
$$E_0 < \quad E'_0 + <\Psi'_0|\ \hat{V}_{ext}-\hat{V}'_{ext}|\Psi'_0> \tag{2.25}$$

Or,
$$E_0 < \quad E'_0 + <\Psi'_0|\int d^3r\, v_{ext}(r_i)\,\hat{n}(r) - \int d^3r\, v'_{ext}(r_i)\,\hat{n}'(r)|\Psi'_0> \tag{2.26}$$

Or,
$$E_0 < E'_0 + \int d^3r\,[v_{ext}(r_i)<\Psi'_0|\ \hat{n}(r)\ |\Psi'_0> - v'_{ext}(r_i) <\Psi'_0|\ \hat{n}'(r)|\Psi'_0>] \tag{2.27}$$

Using the multiplicative form of $\hat{V}_{ext}$ Equation (2.15) and the assumption that both states lead to the same density $n_0$, one obtains

Or,
$$E_0 < \quad E'_0 + \int d^3r\,[v_{ext}(r_i)\mathrm{n}_0(r) - v'_{ext}(r_i)\mathrm{n}_0(r)] \tag{2.28}$$

Or,
$$E_0 < \quad E'_0 + \int d^3r\,\mathrm{n}_0(r)[v_{ext}(r_i) - v'_{ext}(r_i)] \tag{2.29}$$

Interchanging primed and unprimed quantities,

$$E'_0 < E_0 + \int d^3r\,\mathrm{n}_0(r)[v'_{ext}(r_i) - v_{ext}(r_i)] \tag{2.30}$$

Upon addition of Eqs. (2.29) and (2.30), one ends up with a contradiction,

$$E_0 + E_0' < \quad E_0' + E_0 \tag{2.31}$$

One therefore concludes that the map B is also unique: there is a one-to-one correspondence between $| \Psi_0 >$ and $n_0$.

Hence, $v_{ext}$, $| \Psi_0 >$ and $\mathrm{n}_0$ determine each other uniquely.

$$v_{ext}(\boldsymbol{r}) \Leftrightarrow | \underset{\uparrow}{\Psi_0} > \Leftrightarrow \underset{\uparrow}{\mathrm{n}_0}(\boldsymbol{r}) = \quad < \Psi_0 | \hat{n}(\boldsymbol{r}) | \Psi_0 > \tag{2.32}$$

unique (up to some constant in $v_{ext}$)

*Theorem 2***:** *The density that minimizes the total energy functional is the exact ground state density. If one find the functional* $E[n]$*, then the true ground state density* $n(\boldsymbol{r})$ *minimizes it being subjected only to the constraint that*

$$\int d^3r\, n(\boldsymbol{r}) = N$$

For any positive definite trial density,

$$n_0'(r) \neq n_0(r) \;\text{ such that } \int d^3r\, n'(\boldsymbol{r}) = N$$

$$E[n_0] < E[n_0'] \;\Leftrightarrow\; E_0 = \min_{n \in \mathcal{N}} E[n]$$

i.e., the ground state energy can be obtained variationally.

**Proof**:

Let $\Psi_0$ be the wavefunction associated with the correct ground state. The variational principle asserts,

$$< \Psi_0[n(\boldsymbol{r})] | \hat{T} + \widehat{W} + \widehat{V}_{ext} | < \Psi_0[n(\boldsymbol{r})] < \tag{2.33}$$

$$< \Psi'_0[n'(\boldsymbol{r})] | \hat{T} + \widehat{W} + \widehat{V}_{ext} | \Psi'_0[n'(\boldsymbol{r})] >$$

Define the functional

$$F[n] \coloneqq \; < \Psi[n] | \hat{T} + \widehat{W} | \Psi[n] > \tag{2.34}$$

The energy functional $E[n(\boldsymbol{r})]$ alluded to in the first Hohenberg-Kohn theorem can be written in terms of the external potential $v_{ext}(\boldsymbol{r})$ in the following way,

$$E[n(\boldsymbol{r})] = F[n] + \int d^3r\, v_{ext}(\boldsymbol{r}) n(\boldsymbol{r}) \tag{2.35}$$

These lead to

$$F[n_0(\boldsymbol{r})] + \int d^3r\, v_{ext}(\boldsymbol{r}) n_0(\boldsymbol{r}) < F[n_0'(\boldsymbol{r})] + \int d^3r\, v_{ext}(\boldsymbol{r}) n_0'(\boldsymbol{r}) \tag{2.36}$$

$$E[n_0(\boldsymbol{r})] < E[n_0'(\boldsymbol{r})] \tag{2.37}$$

Where,

$$E[n_0(\boldsymbol{r})] = \min_{\mathrm{n}} E[n(\boldsymbol{r})] \tag{2.38}$$

Hence, the variational principle of the second Hohenberg-Kohn theorem is obtained.

The most intriguing feature of this proof is that the functional $F[n]$ is universal for all system of $N$ particles and does not depend upon the external potential $v_{ext}(\boldsymbol{r})$ i.e., if one could minmizes this functional with respect to ground state density, it would solve all many-body problems for all external potentials $v_{ext}(\boldsymbol{r})$. The possibility to determine the ground state density of a many-particle system is given by a variational equation

$$\frac{\delta}{\delta n}\left\{E[n] - \mu\left(\int d^3r\, n(\boldsymbol{r}) - N\right)\right\} |_{n(\boldsymbol{r})=n_0(\boldsymbol{r})} = 0 \tag{2.39}$$

$$\frac{\delta}{\delta n}\left\{F[n] + \int d^3r v_{ext}(\boldsymbol{r}) n(\boldsymbol{r}) - \mu\left(\int d^3r\, n(\boldsymbol{r}) - N\right)\right\} |_{n(\boldsymbol{r})=n_0(\boldsymbol{r})} = 0 \tag{2.40}$$

$$\frac{\delta F[n]}{\delta n} |_{n(\boldsymbol{r})=n_0(\boldsymbol{r})} + v_{ext}(\boldsymbol{r}) = \mu \tag{2.41}$$

Where, $F[n] \coloneqq \ < \Psi[n] \mid \hat{T} + \widehat{W} \mid \Psi[n] > \ = Universal\, part$

We can identify the constant μ as the chemical potential of the system, since $\mu = \frac{\delta E[n]}{\delta n}$. One adds to it any particular set of nuclei, in the form of the external potential $v_{ext}(\boldsymbol{r})$, and then has only to find the function $n(\boldsymbol{r})$ that minimizes it in order to solve the full complexities of Schrodinger's equation. The exact density is such that it makes the functional derivative of $F$ exactly equal to the negative of the external potential (up to a constant). If we had an adequate approximation to $F[n]$ for our purposes, it would be possible to solve the equation for $E[n]$ directly. Unfortuntely, no adequate approximation is available for $F[n]$

## 2.2 Computational Techniques

For many body system the Hohenberg-Kohn theorems states that knowledge of the ground state density is sufficient to determine all ground state observables. In addition, the ground state energy functional $E[n]$ allows the determination of the ground state density itself via the variational equation discussed in the previous section. Although the Hohenberg-Kohn theorems are extremely powerful, do not give any hint concerning the explicit form of $E[n]$ (or $F[n]$) and therefore, do not offer a way of computing the ground-state density of a system in practice. About one year after the seminal DFT paper Hohenberg and Kohn devised a simple method for carrying-out DFT calculations that retains the exact nature of DFT and replaces the many-body problem by an exactly equivalent set of self-consistent one-electron equations. This method is described next.

*2.2.1. The Kohn-Sham (KS) Energy Functional*

Unfortunately, the Hohenberg-Kohn theorem provides no guidance as to the form of $E[n]$, and therefore the utility of DFT depends on the discovery of sufficiently accurate approximations. In order to do this, the unknown functional, $E[n]$, is rewritten as the Hartree total energy plus another, but presumably smaller, unknown functional, called the exchange-correlation $(XC)$ functional, $E_{XC}[n]$. The Kohn-Sham (KS) total-energy functional for a set of doubly occupied electronic states $\psi_i$ can be written as

$$E[n(\boldsymbol{r})] = T_s[n] + E_{ei}[n] + E_H[n] + E_{ii}[n] + E_{XC}[n] \tag{2.42}$$

Here $T_s[n]$ denotes the single particle kinetic energy, $E_{ei}[n]$ is the Coulomb interaction energy between electrons and nuclei, $E_{ii}[n]$ arises from the interaction of the nuclei with each other, and $E_H[n]$ is Hartee component of the electron-electron energy with density ,

$$E_H[n] = \frac{e^2}{2}\int \frac{n(\boldsymbol{r})n(\boldsymbol{r}')}{|\boldsymbol{r}-\boldsymbol{r}'|}\, d^3\boldsymbol{r}\, d^3\boldsymbol{r}' \tag{2.43}$$

including self-interaction energy of the electrons. Where $n(\boldsymbol{r})$ is the electron density given by

$$n(\boldsymbol{r}) = 2\sum_i |\psi_i(\boldsymbol{r})|^2 \tag{2.44}$$

As mentioned, $E_{XC}[n]$ is an unknown functional.

Only the minimum value of Kohn-Sham (KS) energy functional has physical meaning. At the minimum, Kohn-Sham (KS) energy functional is equal to the ground-state energy of the system of electrons with the ions in positions $\{\mathbf{R}_I\}$.

*2.2.2. Kohn-Sham (KS) Equations*

It is necessary to determine the set of wave functions $\psi_i$ that minimize the Kohn-Sham (KS) energy functional. These are given [10] by self-consistent solutions to the

Kohn-Sham (KS) equations[26] which represent a mapping of the interacting many-electron system onto a system of non-interacting moving in an effective potential due to all other electrons. Kohn-Sham system is simply a fictitious system of non-interacting electrons, chosen to have the same density as the physical system. Then its wave functions are given by

$$\left[\frac{\hbar^2}{2m}\nabla^2 + V_{eff}\right]\psi_i(\boldsymbol{r}) = \varepsilon_i\psi_i \tag{2.45}$$

This is a single-electron equations where $\psi_i$ is the wave function of electronic state $i$, $\varepsilon_i$ is the Kohn-Sham eigenvalue, and $V_{eff}$ is the effective potential due to $N-1$ electrons in the Kohn-Sham system,

$$V_{eff} = V_{ion}(\boldsymbol{r}) + V_H(\boldsymbol{r}) + V_{XC}(\boldsymbol{r}) \tag{2.46}$$

The celebrated Kohn-Sham (KS) equations resulting from insertion of

$$\left[\frac{\hbar^2}{2m}\nabla^2 + V_{ion}(\boldsymbol{r}) + V_H(\boldsymbol{r}) + V_{XC}(\boldsymbol{r})\right]\psi_i(\boldsymbol{r}) = \varepsilon_i\psi_i \tag{2.47}$$

$$H_{KS}\psi_i(\boldsymbol{r}) = \varepsilon_i\psi_i \tag{2.48}$$

have to be solved in a s elf-consistent fashion. Where $H_{KS}$ is the Hamiltonian for a Kohn-Sham system,

$$H_{KS} = \frac{\hbar^2}{2m}\nabla^2 + V_{ion}(\boldsymbol{r}) + V_H(\boldsymbol{r}) + V_{XC}(\boldsymbol{r}) \tag{2.49}$$

Here, $V_{ion}(\boldsymbol{r})$ is the total electron-ion potential, $V_H(\boldsymbol{r})$ is the Hartee potential of electrons given by

$$V_H(\boldsymbol{r}) = e^2\int \frac{n(\boldsymbol{r}')}{|\boldsymbol{r}-\boldsymbol{r}'|}\, d^3\boldsymbol{r}' \tag{2.50}$$

and the exchange-correlation potential, $V_{XC}(\boldsymbol{r})$, is given formally by the functional derivative

$$V_{XC}(\boldsymbol{r}) = \frac{\delta E_{XC}(\boldsymbol{r})}{\delta n(\boldsymbol{r})} \tag{2.51}$$

The Kohn-Sham (KS) equations must be solved self-consistently i.e., a density must be found such that it yields an effective potential that when inserted into the Schrodinger-like equations yields wavefunctions that reproduce it . A flow chart that depicts the self-consistent solutions of KS equations is shown in Figure 2.2. Thus, instead of having to solve a many-body Schrodinger equation, using DFT we have the far easier problem of determining the solution to a series of single particle equations, along with a self-consistency requirement . The sum of the single-particle Kohn-Sham eigenvalues does not give the total electronic energy because this overcounts the effect of electron-electron interaction in the Hartee energy and in the exchange-correlation energy.

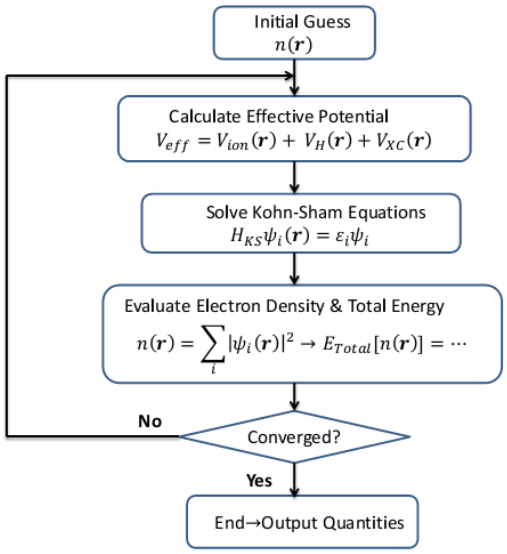


Figure 2.2 Flow-chart depicting a generic Kohn-Sham calculation.

*2.2.3. The Exchange Correlation Energy*

If the exchange-correlation energy functional were known exactly, taking the functional derivative with respect to the density would produce an exchange-correlation

potential that included the effects of exchange and correlation exactly. No analytical form has yet been identified and therefore, an approximation must be used. The Hohenberg-Khon theorem provides some motivation for using approximate methods to describe the exchange-correlation energy as a function of electron density. The simplest method of describing the exchange-correlation energy of an electronic system is to use the local-density approximation[27].

2.2.3.1. Local Density Approximation (LDA)

In the local-density approximation the exchange-correlation energy of an electronic system is constructed by assuming that the exchange-correlation energy per electron at a point $\boldsymbol{r}$ in the electron gas, $\varepsilon_{XC}(\boldsymbol{r})$, is equal to the exchange-correlation energy per electron in a homogeneous electron gas that has the same density as the electron gas at point $\boldsymbol{r}$. In the LDA, $E_{XC}(\boldsymbol{r})$ is written as

$$E_{XC}[n(\boldsymbol{r})] = \int \varepsilon_{XC}(n(\boldsymbol{r}))\, n(\boldsymbol{r}) d^3\boldsymbol{r} \tag{2.52}$$

and

$$\frac{\delta E_{XC}(\boldsymbol{r})}{\delta n(\boldsymbol{r})} = \frac{\partial[\varepsilon_{XC}(n(\boldsymbol{r}))n(\boldsymbol{r})]}{\partial n(\boldsymbol{r})} \tag{2.53}$$

with $\varepsilon_{XC}(\boldsymbol{r}) = \varepsilon_{XC}^{hom}[n(\boldsymbol{r})]$.

where $\varepsilon_{XC}^{hom}[n(\boldsymbol{r})]$ is approximated by a local function of the density, usually that which reproduces the known energy of the uniform electron gas. The local-density approximation assumes that the exchange-correlation energy functional is purely local and, in principle, ignores corrections to the exchange-correlation energy at a point $\boldsymbol{r}$ due to nearby inhomogeneities in the electron density.

A straightforward generalization of the LDA to include electron spin is local spin-density approximation (LSDA)

$$E_{XC}[n_\uparrow, n_\downarrow] = \int \varepsilon_{XC}(n_\uparrow, n_\downarrow)\, n(\boldsymbol{r}) d^3\boldsymbol{r} \tag{2.54}$$

2.2.3.2. Generalized Gradient Approximation (GGA)

Generalized gradient approximations (GGAs), where the local gradient as well as the density is used in order to incorporate more information about the electron gas in question, favor density inhomogeneity more than LSDA does. In GGA, $\varepsilon_{XC}(n(\boldsymbol{r}))$ is replaced by $\varepsilon_{XC}(n(\boldsymbol{r}), |\nabla n(\boldsymbol{r})|)$ to take the account of inhomogeneity for a slowly varying density. Generalized gradient approximations (GGA) [28] [29] has the following form:\

$$E_{XC}[n_\uparrow, n_\downarrow] = \int \varepsilon_{XC}(n_\uparrow, n_\downarrow, \nabla n_\uparrow, \nabla \boldsymbol{n}_\downarrow)\, n(\boldsymbol{r}) d^3\boldsymbol{r} \tag{2.55}$$

In comparison with LDA and LSDA, GGAs have many advantages[28,30–36]. For example, GGAs significantly improve the ground state properties of light atoms and molecules, clusters and solids composed of them. Unlike the LSDA the correct bcc ground state of $Fe$ is obtained through GGAs. Structural properties are generally improved, although GGAs sometimes lead to overcorrection of the LDA errors in lattice parameters.

2.2.4. DFT+U

In solid, both $d$ – and $f$ -states have tendency to retain their atomic character while the valence $s$ - and $p$-states tend to form bands. Both LDA and GGA descriptions for $s$ - and $p$-states are well agreement with the experimental observations. However, it has been a common practice that both LDA and GGA can not predict the behavior of highly localized and atomic-like $d$ – and $f$ – states accurately in many compounds especially which contain rare-earth or late transition metal elements [25]. For many

transition metal oxides, where a sizeable band gap is observed experimentally, both LDA and GGA predict metallic ground states and itinerant $d$ –states or underestimate the band gap significantly. These descrepencies are inherited in the calculation primarily due to the lack of proper treatment of the self-interaction correction (SIC) of the electrons [47]. The improper treatments of band gap and $d$ or $f$ –states can be improved by a decomposition of the complete Hilbert space into two subsystems, following the Anderson model[37]: (i) the localized $d$ -or $f$ -states for which a more explicit, orbital-dependent treatment of all Coulomb effects is required, and (ii) the $s$ - and $p$-states which are well described by the LDA (or GGA). The technical implementation of this concept in DFT is the LDA (or GGA)+ U method where U is known as Hubbard parameter[38 394041] . For its derivation the only assumption required is that the $d$ -or $f$ -states are localized within well-separated atomic spheres, so that the bulk states are well represented by a superposition of the corresponding atomic states only. The Hubbard parameter $U$ is defined as [42]

$$U = E(d^{n+1}) + E(d^{n-1}) - 2E(d^n) \tag{2.56}$$

i.e., the Coulomb energy cost to place the two electrons at the same site. In all model Hamiltonians the U parameter is treated as a constant which only depends on the type of atom and its environment in the crystal through the screening (or renormalization) effects but not on the configuration of the localized electrons. The new functional[39] is [4243]:

$$E^{DFT+U} = E^{DFT}\,[n(\boldsymbol{r})] + E^{U}[\{n_m^{I\sigma}\}] - E^{dc}[\{n^{I\sigma}\}] \tag{2.57}$$

where $n_m^{I\sigma}$ are the atomic-orbital occupations for the atom $I$ experiencing the "Hubbard correction" term, $E^{DFT}\,[n]$ is a standard approximate DFT functional, $E^{U}[n_m^{I\sigma}]$ is Hubbard correction term, and the last term in the above equation $E^{dc}[\{n^{I\sigma}\}]$ is called the "double counting" term subtracted explicitly to avoid the double counting of energy contribution of these orbitals included in $E^{U}[\{n_m^{I\sigma}\}]$ and, in some average way, in $E^{DFT}\,[n(\boldsymbol{r})]$ (LDA or GGA functionals). The DFT + U functional introduced in the above

eqution contains only a minimal set of on-site interaction parameters that takes account the effect only associated to on-site Coulomb repulsion and therefore, neglect the proper treatment of magnetic (exchange) interaction. These effects can be compensated, or alternatively can be mimicked redefining the $U$ parameter as $U^{eff} = U - J$[44] where $J$ denotes the Stoner exchange parameter. Taking both on-site Coulomb and proper magnetic (exchange) interactions into the consideration the total energy functional of DFT+ U can be written as [45]

$$E^{DFT+U} = E^{DFT}[n(\boldsymbol{r})] + E^{U}\left[\{n_{mm'}^{I\sigma}\}\right] \tag{2.58}$$

Where $E^{U}\left[\{n_{mm'}^{I\sigma}\}\right]$ is the simplified form of the Hubbard correction to the energy functional [45]

$$E^{U}\left[\{n_{mm'}^{I\sigma}\}\right] = E^{U}\left[\{n_{mm'}^{I}\}\right] - E^{dc}[\{n^{I\sigma}\}] \tag{2.59}$$

$$= \frac{U^{I}}{2}\sum_{I,\sigma}\sum_{i}\lambda_{i}^{I\sigma}(1-\lambda_{i}^{I\sigma})$$

$$with\ 0 \le \lambda_{i}^{I\sigma} \le 1$$

In the above equation, $U^{I}$ is the Coulomb repulsion parameter on atomic site $I$. This is how the new functional $E^{U}\left[\{n_{mm'}^{I\sigma}\}\right]$ compensates the known deficiencies of LDA or GGA for atomic systems. However, the price is paid appeared obvious in the above equation that $E^{U}\left[\{n_{mm'}^{I\sigma}\}\right]$ favors only partial occupation of the localized orbitals and vanishes for fully occupied $(\lambda \approx 1)$ or completely empty $(\lambda \approx 0)$ orbitals. This is the basic physical effect built in the DFT + U functional.

*2.2.5. DFT-Hybrid*

This method of approximation incorporates exact exchange from Hartree Fock with exchange-correlation term from LDA or GGA. Hybrid functionals are better than DFT

in determining band gap, vibrational properties, static and dynamic dielectric function and also magnetic properties. Hybrid functional are step forward compared to LDA and GGA but still it is not a universal improvement and not as cost effective as standard DFT calculation.

There are many hybrid functionals in use such as B3LYP, HSE, and MO6. In our study we use HSE06[46–48] functional.

$$E_{XC}^{HSE} = \alpha E_X^{SR}(\mu) + (1-\alpha)E_X^{PBE,SR}(\mu) + E_X^{PBE,LR}(\mu) + E_C^{PBE} \quad (2.60)$$

where $E_C^{PBE}$ is the PBE functional for the correlation energy, SR and LR denotes short range and long range part of the electron-electron interaction respectively. The mixing coefficient α was set to ¼ i.e only 25% of exact exchange was used in the present work. For screening parameter, μ = 0.2 $Å^{-1}$ was used as required in HSE06 functional.

### 2.2.6. Projector Augmented Wave (PAW) Method

In order to solve the electronic structure problem within the DFT formalism, the Kohn-Sham equations are to be solved in some efficient numerical way. The key problem is to expand electron orbitals used to express the single particle density in K-S equation in terms of any converged basis set that accounts different behavior of wave functions of real materials in different regions of space. Atomic wave functions of real materials, which are the eigenstates of the atomic Hamiltonian and are all mutually orthogonal to each other, are fairly smooth in the bonding region, however, oscillates rapidly close to the nucleus owing to the large attractive potential of the nucleus. In order to maintain the orthogonal property of atomic wave functions, which is required by the exclusion principle, the valence wave functions oscillate rapidly in the core region since the core wave functions are well localized around the nucleus. This arises difficulty in solving K-S

equations within the DFT formalism numerically to describe the bonding region to a high degree of accuracy while accounting for the large variations in the atom center requiring a very large basis set, or a very fine mesh. Numerous methods have been developed to solve the resulting single particle K-S equation treating core and valence electrons in a different way, possibly obtaining numerical advantages.

One common approach is to use frozen-core approximation that treats core states are invariant in the different chemical environments. Pseudopotential, which exploits frozen-core approximation, replaces the strong ionic potential experienced by core electrons with an effective, smooth and weaker potential. This pseudopotential acts on a set of pseudo wave functions rather true valence wave functions in such a way to reproduce the true effect on the valence electrons outside the core region. This approximation allows one to solve Kohn-Sham equations only for the valence electrons reducing computational cost, however, makes harder to calculate properties that rely on the core region e.g., electric field gradients, hyperfine parameters, etc. Another major drawback is that the procedure to generate good pseudopotentials is not well controlled.

Another approach is the so called class of “all-electron” methods (AE), in which the strong ionic potential in core region is no longer replaced with an effective, smooth and weaker potential. Hence, full information about real wave functions in the core region is available compared to pseudopotential approach. One of the most important of such methods is the Augmented-Plane-Wave method (APW) [4950], in which the space is partitioned in two regions: a spherical one around each atom in which the wavefunction is expanded onto a local basis in order to reproduce the great variations, and an interstitial region in which another basis is chosen (plane waves for instance) and connected to the first local basis. A modification of APW which provides a flexible and accurate band structure method is known as Liner-APW (LAPW) [37].

The projector augmented wave method (PAW) [51] is a technique used in ab initio electronic structure calculations. It is a generalization of the pseudopotential and linear augmented-plane-wave methods, and allows for density functional theory calculations to be performed with greater computational efficiency. It is an all electrons (AE) method for ab-initio molecular dynamics that provides the full wave functions that are not directly accessible with the pseudopotential approach, and the potential is determined properly from the full charge densities. PAW avoids transferability problems of pseudopotentials and provides theoretical basis for pseudopotentials. Like APW (or LAPW), PAW method transforms the rapidly oscillating wavefunctions in the core region into smooth wavefunctions which are more computationally convenient.

2.2.6.1 Formalism

The trick in PAW method is to divide the wave functions into two parts: i) a partial-wave expansion within an atom-centered sphere and ii) envelope functions outside the spheres. The partial waves are the solution of radial Schrödinger equation times spherical harmonics for the isolated atom and exhibits orthogonally to the core states if needed. On other hand, the envelope function is expanded into plane waves or some other convenient basis set. However, both envelope function and partial-wave expansions are continuous at boundary of the sphere.

In PAW method, a linear transformation operator $\hat{T}$ maps the physically relevant AE wave functions, which are orthogonal to the core states, onto the computationally convenient Pseudo (PS) wave functions or vice versa. The PS wave functions will be identified with the envelop functions of the linear method[52] or the Pseudopotential approach. This approach is somewhat reminiscent of a change from the Schrödinger picture to the Heisenberg picture.

Linear transformation from pseudo wave functions to AE wave functions

$$|\Psi\rangle = \hat{T}|\Psi_l^{ps}\rangle \tag{2.61}$$

where $l$ is a quantum state label, consisting of a band index and possibly a spin and $k$-vector index. The linear transformation operator

$$\hat{T} = 1 + \hat{T}_R \tag{2.62}$$

where $\hat{T}_R$ is non-zero only within some spherical augmentation region $\Omega_R$ enclosing atom $R$ and unity outside this region where AE and PS wave functions coincide with each other. The augmentation spherical regions are chosen such a way that there is no overlap between the spheres. Around each atom, it is useful to expand the pseudo wave function into pseudo partial waves:

$$|\Psi_l^{ps}\rangle = \sum_{iR} {c_{li}}^R |\phi_{li}^{ps\,R}\rangle \text{ within } \Omega_R \tag{2.63}$$

The corresponding AE wave function is of the form

$$|\Psi\rangle = \hat{T}|\Psi_l^{ps}\rangle \tag{2.64}$$

$$|\Psi\rangle = \hat{T}\sum_{iR} {c_{li}}^R |\phi_{li}^{ps\,R}\rangle \tag{2.65}$$

$$|\Psi\rangle = \sum_{iR} {c_{li}}^R |\phi_{li}^R\rangle \text{ within } \Omega_R \tag{2.66}$$

with ${c_{li}}^R$ same as in pseudo partial wave expansions. Hence, we can express the AE wave function as

$$\begin{aligned} |\Psi\rangle = \left(1 + \hat{T}_R\right)|\Psi_l^{ps}\rangle &= |\Psi_l^{ps}\rangle + \hat{T}_R|\Psi_l^{ps}\rangle \\ &= |\Psi_l^{ps}\rangle + \left(\hat{T} - 1\right)\Big|\sum_{iR} {c_{li}}^R |\phi_{li}^{ps\,R}\rangle \\ &= |\Psi_l^{ps}\rangle + \sum_{iR} {c_{li}}^R |\phi_{li}^R\rangle - \sum_{iR} {c_{li}}^R |\phi_{li}^{ps\,R}\rangle \end{aligned} \tag{2.67}$$

where the expansion coefficients for the partial wave expansions have to be determined. Because the operator $\hat{T}$ is linear, the coefficients ${c_{ni}}^R$ are linear functions of pseudo wave functions and thus, can be written as an inner product with a set of so-called projector functions, $|p_i^{ps}\rangle$

$$ {c_{li}}^R = \langle p_i^{ps} |\, \Psi_{li}^{ps\,R} \rangle \tag{2.68} $$

where $\langle p_i^{ps} | \phi_{lj}^{ps\,R} \rangle = \delta_{ij}$ and $\sum_i |\phi_{li}^{ps\,R}\rangle\langle p_i^{ps}| = 1$

The most general form for the projector functions is

$$ |p_i^{ps}\rangle = \sum_j \left(\{\langle f_k | \phi_{lm}^{ps\,R}\rangle\}\right)_{ij}^{-1} \langle f_j| \tag{2.69} $$

where $|f_j\rangle$ form an arbitrary, linearly independent set of functions. The projector functions are localized within $\Omega_R$ if the functions $|f_j\rangle$ are localized. The final form of the linear transformation operator can be written as

$$ \hat{T} = 1 + \sum_{iR} \left(|\phi_{li}^R\rangle - |\phi_{li}^{ps\,R}\rangle\right) \langle p_i^{ps}| \tag{2.70} $$

which allows one to obtain AE Kohn-Sham wave function as

$$ |\Psi\rangle = |\Psi_l^{ps}\rangle + \sum_{iR} \left(|\phi_{li}^R\rangle - |\phi_{li}^{ps\,R}\rangle\right) \langle p_i^{ps} | \Psi_l^{ps}\rangle \tag{2.71} $$

explicitly separating the extended-space and the atom-centered contributions. A schematic representation of PAW method is shown in Figure 2.4. The first term can be evaluated on a plane wav or any convenient basis set, while the last two terms are evaluated on fine radial grids.

In summary, PAW transformation has three properties:

i) Projector functions are localized inside the augmentation spheres i.e., $p_i^{ps\,R}(r) = 0 \; for \; r > \; R_a$

ii) AE orbitals and pseudo orbitals are equal outside the augmentation

spheres

$$\phi_{li}^{R} = \phi_{li}^{ps\,R}, r > R_a \quad (2.72)$$

iii) Projector functions are orthogonal to pseudo orbitals, i.e., $\langle p_i^{ps} | \phi_{lj}^{ps\,R} \rangle = \delta_{ij}$

The partial waves $\phi_{li}^{R}$, which are used as an atomic basis for the all-electron wavefunctions within the augmentation sphere, are constructed as radial solutions of the Schrodinger equation for the isolated atom.

2.2.6.2. Approximations

Like other electronic structure methods some approximations are needed to make PAW method a practical scheme within the DFT formalism. These approximations are:

- Frozen Core

  The frozen core approximation assumes that the core states are invariant under the different chemical environments and localized in the augmentation spheres. No projector functions are needed to define for the core states.

- Finite number of projectors

  The number of projector functions is obviously finite. Typically two projectors per angular momentum are used.

- Truncated angular momentum expansions
- Overlapping augmentation spheres

2.2.6.3. Expectation Values in PAW

we can obtain physical quantities, represented as the expectation value (A) of some operator A, from the PS wave functions $|\Psi_l^{ps}\rangle$ either directly as $\langle\Psi|A|\Psi\rangle$ after transformation to the true AE wave functions $|\Psi\rangle = \hat{T}|\Psi_l^{ps}\rangle$ or as the expectation value $\langle A\rangle = \langle\Psi_l^{ps}|A^{ps}|\Psi_l^{ps}\rangle$ of PS operator $A^{ps} = \hat{T}^{\dagger} A\,\hat{T}$ in the Hilbert space of the PS wave functions. Similarly we can evaluate the total energy directly as a functional of the PS wave functions. The ground-state PS wave functions can be obtained from

$$\frac{\partial E[\hat{T}|\Psi_l^{ps}\rangle]}{\partial\langle\Psi_l^{ps}|} = \epsilon\,\hat{T}^{\dagger}\,\hat{T}|\Psi_l^{ps}\rangle \tag{2.73}$$

Expectation values in PAW:

**Total energy:**
$$E = E_l^{ps} + \sum\nolimits_a (E_l^{R\,a} - E_l^{ps\,a}) \tag{2.74}$$

**Electron density:**
$$n(\boldsymbol{r}) = n_l^{ps}(r) + \sum[n_l^{R\,a}(\boldsymbol{r} - \boldsymbol{R}^a) - n_l^{ps\,a}(\boldsymbol{r} - \boldsymbol{R}^a)] \tag{2.75}$$

2.2.7. Periodic Supercell Approximation

Although Kohn-Sham equations reduce the interacting many-electron Schrödinger equation into an effective single-problem, however, solving infinite number of non-interacting Schrödinger equation with infinite basis set computationally is formidable task. This cumbersome task can be simplified performing calculation on the periodic supercell approximation and applying Bloch's theorem to the electronic wave functions.

2.2.7.1 Bloch's Theorem

Bloch's theorem states that in a periodic solid each electronic wave function can be written as the product of a periodic unit cell part and a wave like part,

$$\psi_i(\boldsymbol{r}) = f_i(\boldsymbol{r}) e^{i\boldsymbol{k}.\boldsymbol{r}} \tag{2.76}$$

where $f_i(\boldsymbol{r})$ periodic unit cell part i.e., $f_i(\boldsymbol{r}) = f_i(\boldsymbol{r} + \boldsymbol{l})$. $f_i(\boldsymbol{r})$ can be expanded using a discrete basis set of plane waves such as

$$f_i(\boldsymbol{r}) = \sum_{\boldsymbol{G}} c_{i,\boldsymbol{G}}\, e^{i\boldsymbol{G}.\boldsymbol{r}} \tag{2.77}$$

where $\boldsymbol{G}$ are the reciprocal lattice vectors defined by $\boldsymbol{G}.\boldsymbol{l} = 2\pi m$ for all $\boldsymbol{l}$ where $\boldsymbol{l}$ is a lattice vector of the crystal and m is an integer.

Hence, each electronic wave function can be written as

$$\psi_i(\boldsymbol{r}) = \sum_{\boldsymbol{G}} c_{i,\boldsymbol{K}+\boldsymbol{G}}\, e^{i(\boldsymbol{G}+\boldsymbol{k}).\boldsymbol{r}} \tag{2.78}$$

or equivalently

$$\psi_i(\boldsymbol{r} + \boldsymbol{l}) = \sum_{\boldsymbol{G}} c_{i,\boldsymbol{K}+\boldsymbol{G}}\, e^{i(\boldsymbol{G}+\boldsymbol{k}).(\boldsymbol{r}+\boldsymbol{l})} \tag{2.79}$$

$$\psi_i(\boldsymbol{r} + \boldsymbol{l}) = e^{i\boldsymbol{k}.\boldsymbol{l}} \sum_{\boldsymbol{G}} c_{i,\boldsymbol{K}+\boldsymbol{G}}\, e^{i\boldsymbol{k}.\boldsymbol{r}}\, e^{i\boldsymbol{G}.(\boldsymbol{r}+\boldsymbol{l})} \tag{2.80}$$

$$\psi_i(\boldsymbol{r} + \boldsymbol{l}) = e^{i\boldsymbol{k}.\boldsymbol{l}} f_i(\boldsymbol{r} + \boldsymbol{l})\, e^{i\boldsymbol{k}.\boldsymbol{r}} = e^{i\boldsymbol{k}.\boldsymbol{l}} f_i(\boldsymbol{r})\, e^{i\boldsymbol{k}.\boldsymbol{r}} \tag{2.81}$$

$$\psi_i(\boldsymbol{r} + \boldsymbol{l}) = e^{i\boldsymbol{k}.\boldsymbol{l}}\, \psi_i(\boldsymbol{r}) \tag{2.82}$$

Imposing periodic boundary condition envisioning the lattice (Figure 2.5) to be in the form of a closed N-atom ring, one must have

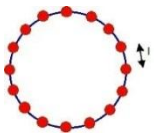

Figure 2.3 A closed N-atom ring.

$$\psi_i(\boldsymbol{r} + \boldsymbol{Nl}) = \psi_i(\boldsymbol{r}) \tag{2.83}$$

which in turn requires

$$e^{\boldsymbol{ik.Nl}} = 1 \tag{2.84}$$

Or, $$k = \frac{2\pi n}{Nl} \ldots\ldots\ldots\ldots n = 0, \pm 1, \pm 2, \pm 3, \ldots\ldots, \pm\frac{N}{2} \tag{2.85}$$

Bloch's representation with periodic boundary condition points out that the number of occupied electronic states is finite, at each k-point, even for infinite periodic systems. This advantage turns out the problem of computing an infinite number of wave functions to one of computing finite number wave functions at infinite number of k-points. Moreover, states with similar $k$ vector are identical which allows one to replace electronic wave functions over a region of $k$ space by the wave functions at a single $k$ point. In that case, only finite number of appropriate sampled set of k-points is required inside the first Brilluoin zone to calculate the electronic potential and therefore determine the total energy of the solid. This advantage reduces computational cost significantly.

2.2.7.2 Plane Wave Basis Sets

According Bloch's theorem it is possible to expand an electronic wave function at each $k$ point interms of a discrete plane wave basis set. In quantum mechanics, an electronic wave function belongs to an infinite-dimensional Hilbert space. Thus in principle, given an electronic wave function $\psi_i(\boldsymbol{r})$, an infinite number of basis plane waves is required in order to reproduce it. However, the infinite number of plane wave basis set can be reduced considering only the plane waves which have kinetic energies less than a particular cutoff energy i.e., $\frac{\hbar^2}{2m}|\boldsymbol{K} + \boldsymbol{G}|^2 \leq E_{cut}$. This choice of a particular

cutoff energy $E_{cut}$, which produces a finite basis set, is reasonable since the coefficients $c_{i,\boldsymbol{G}+\boldsymbol{K}}$ in Bloch's theorem (equation) with smaller kinetic energies are typically more important than those with higher kinetic energies. With plane wave basis set KS equations take following simpler form

$$\sum_{G'}[\frac{\hbar^2}{2m}|\boldsymbol{K}+\boldsymbol{G}|^2\delta_{GG'}+V^{eff}(G-G')]\,c_{i,\boldsymbol{K}+\boldsymbol{G}'}=\varepsilon_i c_{i,\boldsymbol{K}+\boldsymbol{G}'} \tag{2.86}$$

In this form, kinetic energy is diagonal, and effective potential is expressed in Fourier space. The number of elements in Hamiltonian matrix is limited by the choice of $E_{cut}$.

The salient features of a plane-wave basis are:

1. Only $E_{cut}$ is needed to control the convergence of the result.

2. Orthonormality and no dependence on atomic positions, i.e. no basis-set superposition error and Pulay forces.

3. Very efficient to compute integrals and derivatives in reciprocal space which makes the calculation of the matrix elements of the Hamiltonian easier and faster.

Despite these computational friendly features, plane wave basis sets have some drawbacks, especially for isolated systems, where the large number of plane waves is required. A large number of plane waves for a well-converged calculation increases computational cost. Plane waves, in fact, cannot take advantage of the vacuum to reduce the size of the basis. In order to conveniently reduce $E_{cut}$, smooth pseudopotentials must be employed. Furthermore efficient parallelization is problematic due to the mathematics of delocalized plane waves. The required Fourier transforms are actually very difficult to parallelize.

## 2.3 Computational Details

The present calculations were performed within the framework of the standard frozen-core projector augmented-wave (PAW)[53,54] method using density functional theory (DFT) as implemented in Vienna *ab initio* simulation package (VASP)[55,56] code. Exchange and correlation potentials were treated in the generalized gradient approximation (GGA) as parameterized by Perdew-Burke-Ernzerhof (PBE).[28,57] It is well known that underestimation of electron localization is a major failure of both local and semi-local DFT calculations, in particular, for systems with localized $d$ and $f$ electrons.[58–60] This failure manifests in the general trend of DFT to underestimate the band gaps and to produce incorrect metallic solutions for some 3d based metal oxides. This shortcoming of DFT-GGA needs to be corrected in a computationally cost effective manner since defect formation energies are affected by the incorrect band gap calculations. Several post-DFT methods are available to improve the band gap calculations such as hybrid DFT[61–66], self-interaction corrected (SIC) density functionals[67], dynamical mean-field theory[68], reduced density matrix functional theory[69], the screened exchange (sX) method[70], GW[66,71–73], or quantum Monte Carlo[74]; however they are computationally demanding. Moreover, popular methods like hybrid DFT does not guarantee to position defect levels correctly while intending to reproduce the experimental band gap by parameterization.[75] Due to the heavy computational demand of the present work, it is desirable to embrace a post-DFT method that is computationally cost-effective as well as shows improved band gap over DFT. Under these circumstances, an on-site Coulomb correlation through the Hubbard-based *U* correction parameter[39,43,58] can be the best option as post-DFT method to reduce the band gap error and predict other electronic properties. In the present work, we have used $U_{eff}$ = 6 eV, ($U_{eff}$ = U-J=7-1= 6 eV, J =

Stoner exchange parameter) that externally provides Coulomb correlation to the desired orbital of the considered atoms.

The basis sets were expanded with plane-waves with a kinetic energy cut-off of 400 eV. The density-of-states (DOS) plots were generated with the tetrahedron method.[76] The ion positions and volumes were always relaxed without any symmetry constraint to allow the internal geometry and the shape of the lattice to be changed freely until the force on each of the ion was 0.01 eV/Å or less. The Monkhorst–Pack[77] k-point sampling was used for ionic relaxation. For visualization of the crystal structures, VESTA (Visualization for Electronic and Structural Analysis)[78,79] was used. The k-mesh details for different cells and the computational specifications which differ from above will presented in respective chapters and sections.

## 2.4 Physical Properties

### 2.4.1. Formation Enthalpy

The formation enthalpy of a compound represents the amount of energy required to form its stable composition at thermodynamic equilibrium. The formation enthalpy of a given bulk phase defined as

$$\Delta H_f = E_{solid} - n_\alpha \sum_\alpha E_\alpha^{bulk/molecule} \tag{2.87}$$

where, $E_{solid}$ is the total energy of a given bulk phase, and $E_\alpha^{bulk}$ represents the energy per atom of a constituent species α in its standard elemental phase. For example, $E_{Cu}^{bulk}$ corresponds to the energy per atom with respect to FCC phase of Cu. $n_\alpha$ is the number of

atoms of species α present per unit formula of the given compound. For oxygen, we have considered its molecular (dimer) form i.e., $E_O^{molecule} = E_O^{dimer}$.

2.4.2. Cohesive Energy

The cohesive energy is a measure of cohesion of atoms in solid aggregates manifesting the thermal stability of solids. Hence, the cohesive energy is the solid state analog of the atomization energy or the energy needed to break a solid apart into isolated atoms i.e.,

$$E_{cohesive} = E_{solid} - \sum_{\alpha_i} E_{a_i}^{isolated} \tag{2.88}$$

where $\alpha_i$ represents the different atoms that constitute the solid. It is well known, all stable arrangements of atoms in solids are such that the potential energy is minimum. The cohesive energy, which corresponds to the attractive part of the potential energy, tells that lower the cohesive energy, stronger the bonding between the atoms in solid aggregate.

2.4.3. Fragmentation Energy

The successful synthesis of a compound depends on the stability against its decomposition into different competitive phases such as pure elemental or secondary phases or combination all phases. Although formation enthalpy gives an estimate about the materials' stability with respect pure elemental phases, it does not give any hint as to the stability against its fragmentation into other possible competitive phases. The fragmentation of a compound (p) with respect to secondary/elemental phases (s) is defined as

$$\Delta H_{frag,p} = \Delta H_{f,p} - \sum_{s_i} \Delta H_{f,s} \quad (2.89)$$

2.4.4. Chemical Potential Landscape

A chemical potential landscape, wherein the desired material is thermodynamically stable, can be defined as a region spanned by chemical potentials of the constituent atomic species of that material. In equilibrium, these chemical potentials must satisfy the following to form a stable desired crystal

$$\sum_{\alpha=1}^{l} n_\alpha \Delta\mu_\alpha = \Delta H_{f,p}$$

where both $\alpha$ and $n_\alpha$ have the same meanings as defined before. $\Delta H_{f,p}$ is the formation enthalpy of the primary compound as defined in equation (4) (here the subscript 'p' refers to 'primary' as the targeted material).

The number of competitive secondary phases increases as the number of cations in a compound increases. These secondary phases split the chemical potential landscape up into different domains. The domains bounded by possible secondary phases determine the single-phase formation and degree of stability of a desired compound at particular growth condition. Larger bounded region implies higher stability of the material under consideration and more flexibility in tuning the growth conditions. For $\alpha = l\ (l > 1)$, chemical potentials of other $(l-1)$ species have to be varied keeping chemical potential of one species fixed. To avoid a secondary phase,

$$\sum_{\beta=1}^{l} n_\beta \Delta\mu_\beta < \Delta H_{f,s}$$

where $\Delta H_{f,s}$ is the formation enthalpy of a secondary phase (here the subscript 's' refers to 'secondary'); β corresponds to different atomic species in a secondary phase; $n_\beta$ is the number of atoms of the species β present per unit formula of each secondary phase. For example, CuS is one of the probable secondary phases for CZTS, where l = 2 (Cu and S) for CuS, and $n_\beta$ =1 for both Cu and S. To avoid the co-existence of CuS

$$\Delta\mu_{Cu} + \Delta\mu_S < \Delta H_{f,CuS}$$

2.4.5. Defect Formation Energy

The method to calculate total energy with periodic boundary conditions for a system that contains a defect has been devised based on the assumption that the interaction among the periodic image defects between the neighboring cells is negligible. This assumption is incorporated in the context of "supercell approximation" in which a defect is occurred in a periodic supercell. The formation energy for a defect δ in a charge-neutral state is[80–83]

$$\Delta H(\delta) = E(\delta) - E(host) + \sum_\alpha m_\alpha \mu_\alpha$$

where E(δ) and E(host) correspond to the total energies of the compound with and without defect δ, respectively. The index α represents different atomic species that constitute the solid; $m_\alpha$ is the number of α atoms removed (added) from (to) the system for the defect δ. $m_\alpha$ =1 if an atom of species α is removed from the system while $m_\alpha$ = -1 if an atom of species α is added to the system. $\mu_\alpha$ is the chemical potential of species α

$$\mu_\alpha = \mu_\alpha^0 + \Delta\mu_\alpha$$

where $\mu_\alpha^0$ is the reference chemical potential of the constituent species α in its standard elemental phase, e.g. the standard phases of the metals Cu and Zn are FCC structures; Sn has metallic standard phase, alpha–Sn; and alpha–S ($S_8$) is standard solid

phase of S. $\Delta\mu_\alpha$ determines α-rich/α-poor growth condition with respect to a bulk phase and is bounded by

$$\Delta H_f \leq n_\alpha \Delta\mu_\alpha \leq 0$$

where, $\Delta H_f$ is the formation enthalpy of a given bulk phase defined as

$$\Delta H_f = E_{solid} - n_\alpha \sum_\alpha E_\alpha^{bulk}$$

where, $E_{solid}$ is the total energy of a given bulk phase, and $E_\alpha^{bulk}$ represents the energy per atom of a constituent species α in its standard elemental phase. For example, $E_{Cu}^{bulk}$ corresponds to the energy per atom with respect to FCC phase of Cu. $n_\alpha$ is the number of atoms of species $\alpha$ present per unit formula of the given compound. $n_\alpha\Delta\mu_\alpha = 0$ corresponds to extreme α-rich growth conditions where atoms of species a are readily available; whereas, $n_\alpha\Delta\mu_\alpha = \Delta H_f$ corresponds to extreme α-poor growth condition manifesting the scarcity of a species atoms in the surroundings.

2.4.6. Defect Concentration

The equilibrium concentration of a defect δ at charge state q in crystal can be given[80]

$$c(\delta, q) = N_{sites}\, g_q \exp(-\Delta H(\delta,q)/K_B T \quad (2.90)$$

where $K_B$ = Boltzmann constant

T = temperature

$\Delta H(\delta,q)$ = formation energy at T = 0 K

$N_{sites}$ = is the number of possible atomic sites at which the defect may be formed.

$g_q$ = degeneracy factor, which equals the number of possible configurations for electrons occupying the defect levels and changes with the charge state q.

2.4.7. Conductivity Effective Mass

A conductivity mass ($m_c$) is defined[84] by means of ratio $\frac{\hbar k}{m_c} = v$. For a general band

$$v = \frac{1}{\hbar}\frac{\partial \epsilon}{\partial k_i} = \sum_j (\frac{1}{m_c})_{ij}\, \hbar k_j \tag{2.91}$$

If tensor in diagonal

$$(\frac{1}{m_c})_{ii} = \frac{1}{\hbar^2}\frac{1}{k_i}\frac{\partial^2 \epsilon}{\partial k_i^2} \tag{2.92}$$

2.4.8. Optical Absorption

In the present work, we have studied the optical absorption as one of the most important optical property for PV/PEC process. In treating a solid, it is necessary to consider contributions to the absorption from various electronic energy band processes such as intraband, interband. However, we restrict ourselves to the interband processes because intraband processes are less important to semiconductors.[85] All the semiconductors have a fundamental absorption edge in the near-infrared, visible or ultraviolet spectral region. The absorption edge is caused while electrons absorbing photon make an interband transition from an occupied state in the valence band to an unoccupied state in the conduction band. The probability of interband transition across the band gap in semiconductor is governed by a parameter called absorption coefficient, which is given by[85–87]

$$\alpha(\omega) = \frac{2\omega k_{ii}(\omega)}{c} \tag{2.93}$$

Where $\omega$ is the frequency of absorbed light, $c$ be the speed of light, and $k_{ii}(\omega)$ is the extinction coefficients which are directly related to the diagonal components of frequency dependent complex dielectric tensors, $\epsilon_{ii}$ and have the following expression[86–88]

$$k_{ii}(\omega) = \frac{1}{\sqrt{2}}\left[\{(Re\ \epsilon_{ii})^2 + (Im\ \epsilon_{ii})^2\}^{1/2} - Re\ \epsilon_{ii}\right]^{1/2} \tag{2.94}$$

Once the ground state was determined, frequency dependent dielectric matrix had been evaluated using VASP 5.2. and above which calculates directly [89] imaginary part using the equation :

$$Im\ \epsilon_{ij}(\omega) = \frac{4\pi^2 e^2}{\Omega} \lim_{q\to 0} \frac{1}{q^2} \sum_{c,v,\boldsymbol{k}} 2\omega_{\boldsymbol{k}} \delta\left(\epsilon_{c\boldsymbol{k}} - \epsilon_{v,\boldsymbol{k}} - \omega\right) \times \left\langle u_{c\boldsymbol{k}+\boldsymbol{e_i q}} \middle| u_{v\boldsymbol{k}} \right\rangle \left\langle u_{c\boldsymbol{k}+\boldsymbol{e_j q}} \middle| u_{v\boldsymbol{k}} \right\rangle^* \quad (2.95)$$

and real part with the usual Kramers-Kronig transformation

$$Re\ \epsilon_{ij}(\omega) = 1 + \frac{2}{\pi} P \int_0^\infty \frac{\left[Im\ \epsilon_{ij}(\omega')\right]\omega'}{\omega'^2 - \omega^2 + i\eta} d\omega' \quad (2.96)$$

where P denotes the principle value and $\eta$ is the complex shift.

# Chapter 3

## Crystal Structure Prediction

### 3.1 Introduction

All the motif structures (possible candidates for global optimization) in the present study were found from existing structures in mineral database.[1,90] Additionally, StructurePredictor[1,90] software generated structures were also considered for global optimization The existing structures were of the forms from similar stoichiometry to different ones of higher/lower order compounds. Several manipulations of existing structures produced the unit cells (motif structures) of the desired stoichiometry. Those motif structures were then exposed to DFT calculation, and the lowest energy structure was considered as the possible crystal structure for the material of interest. See References[12,91,92] for the details of crystal structure modeling of the materials considered below.

### 3.2 Computational Details

We have used DFT (+U for 3d comprising compounds) for global optimizations of all motif structures. In addition, we employed van der Waals (vdW) correction to $Sn_2O_3$. It is well-known that the contributions from long-range non-bonded dispersion interactions between the layers in layered structures are non-negligible. Only DFT or hybrid-DFT or Hartree-Fock methods are unable[93–95] in taking account those interaction precisely in layered structures.[96–99] Since $Sn_2O_3$ was previously reported to layered structure, vdW correction was further considered to compensate the failure of DFT. Among many existing flavors of vdW correction, a method introduced by Grimme[100] and implemented in VASP as DFT-D2 has been a popular choice for a wide class of systems due to its satisfactory results in conjunction with computational efficiency.[101–105] The ion positions

and volumes were always relaxed without any symmetry constraint to allow the internal geometry and the shape of the lattice to be changed freely until the force on each of the ion was 0.01 eV/Å (0.001 eV/Å for vdW -DFT[92]) or less. The Monkhorst–Pack[106] k-point sampling was used for geometry optimization. For visualization of the crystal structures, VESTA (Visualization for Electronic and Structural Analysis) was used.

## 3.3 Materials with $AgBiW_2O_8$ Stoichiometry

### *3.3.1 $AgBiW_2O_8$*

With our total energy DFT calculations, the wolframite (*P 2/c*, S. G. 13, Z=2) structure in Figure 3.1a was found to be the most stable. The X-ray diffraction (XRD) of the latest experimental result[91] (see Figure 3.1b) further confirms the wolframite crystal structure of $AgBiW_2O_8$.

### *3.3.2 $CuBiW_2O_8$*

In our earlier work,[12] we have predicted $CuBiW_2O_8$ as a suitable photocatalyst. The crystal structure of it is also predicted from existing through mineral database search. Our DFT+U calculation determined $CuWO_4$ derived structure, as shown in Figure 3.2a, as the probable crystal structure of $CuBiW_2O_8$. In a search for previously published literature on $CuBiW_2O_8$, we have found with only one experimental article[107] published over twenty years ago, and no theoretical work at all. All the calculations at that time were done in VASP 5.2 and the predicted structure was found to be 0.001 eV higher than the experimental counterpart.

Since the crystal structure determines electronic properties of a material uniquely, and the reference structure is limited to one, the quest for finding further lower

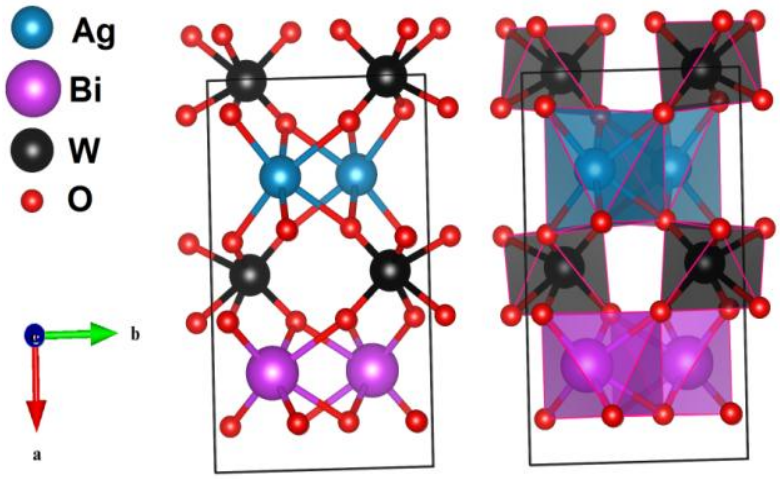


(a)

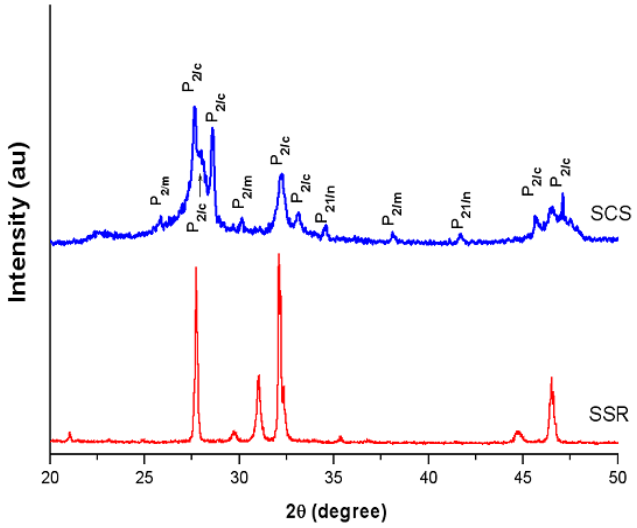


(b)

Figure 3.1 a) Crystal structure and b) XRD of $AgBiW_2O_8$. Two models: (left) ball-and-stick and (right) polyhedra of DFT derived crystal structure are presented in figure a. On the other hand, the two XRDs in figure b correspond to two samples of $AgBiW_2O_8$, which were synthesized in solution combustion synthesis (SCS) and solid state reaction (SSR) methods.

energy structure(s) of $CuBiW_2O_8$ was continued, which produced a structure energetically 0.004 eV lower than the experimental structure. This latest predicted structure was $CuBi_2O_4$ (mp-560165)-derived (note that mp-560165 was recently assigned to new structure and the older structure no longer exists in the Material Project database). The motif structure in this case was generated i) by replacing two Bi atoms along 'a' axis by two W atoms and ii) removing one Bi and Cu (farther from the corner along the edge) atom. Note that later optimizations of latest motif structures were carried out in both VASP 5.2 and 5.3.3. Although $CuBi_2O_4$ (mp-560165)-derived structures found to be most stable irrespective of VASP versions, the order of the stability of other two structures were switched, despite the fact that the energy difference were still nominal (see Table 3.1). Since the energy difference is very small for all three probable structures, any structure can be the outcome in the synthesis process. Further, the small difference in energy may fall within the accuracy of the theoretical methods used in the present calculations. A comparison between energetics and structural attributes of these probable structures was presented in Table 3.1.

Recently, $CuBiW_2O_8$ has been synthesized in our experimental collaborator's (Dr. Krishnan Rajeshwar, Department of Chemistry and Biochemistry, UTA) laboratory; solid state reaction (SSR) method was employed in synthesizing that. The details of the experimental investigation will be presented elsewhere. The XRD of this newly synthesized sample in conjunction with that of three DFT+U optimized possible structures is presentenced in Figure 3.2b. It is seen that the calculated XRD of $CuBi_2O_4$ -derived structure mostly corresponds to its experimental counterpart. This validates our crystal structure prediction on $CuBiW_2O_8$. Despite that fact dissimilarities were observed in those XRD's which could be attributed to presence of secondary phases in the synthesized sample. The quest for achieving a pure single-phase of $CuBiW_2O_8$ is going on in our

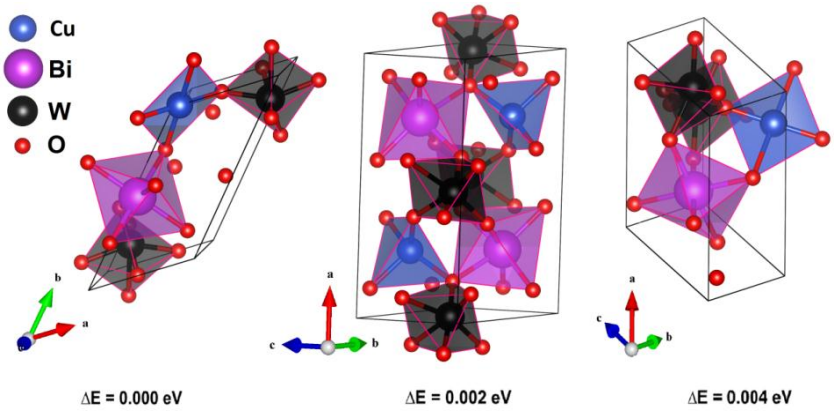


(a)

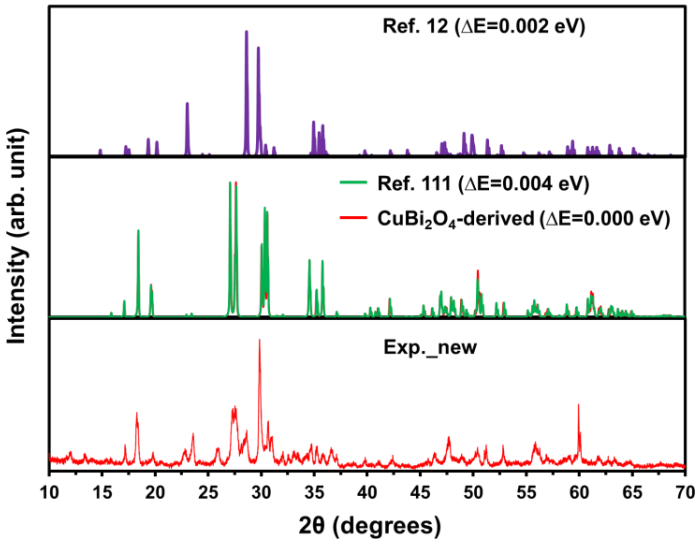


(b)

Figure 3.2 a) The polyhedral model of probable crystal of $CuBiW_2O_8$: (left) $CuBi_2O_4$ - derived, Ref.[12] (middle), and (right) Ref. [107]. The K-mesh used for these structures are 13x9x11, 7x11x3, and 9x13x11, respectively. b) The calculated XRDs of three structures in figure a in conjunction with an experimental counterpart of a $CuBiW_2O_8$ sample that was recently synthesized through solid state reaction (SSR) method in Dr. Rajeshwar's lab at UTA.

Table 3.1 A comparison between DFT+U energetics, volumes, and lattice constants of three probable structures of $CuBiW_2O_8$.

| Structure | Formula Unit, Z | Energy Difference/Z eV | Volume/Z Å$^3$ | Lattice Parameters | | | | | |
|---|---|---|---|---|---|---|---|---|---|
| | | | | a | b | c | α | β | γ |
| | | | | Å | | | degrees | | |
| $CuBi_2O_4$ -derived | 1 | 0.000 | 156.65 | 5.012 | 7.76 | 6.14 | 90.6 | 65.8 | 51.0 |
| Ref.[12] | 2 | 0.002 | 151.56 | 5.064 | 5.97 | 5.02 | 90.0 | 92.9 | 90.0 |
| Ref. [107] | 1 | 0.004 | 156.53 | 6.912 | 5.01 | 6.14 | 65.8 | 54.6 | 69.9 |

collaborator's lab. Note that first reported synthesized structure (Ref. [107]) has the highest energy among all, however, its XRD matches with that of the lowest energy structure, despite the difference in their lattice parameters. This means that these two structures are locally isotropic e.g. Cu in both structures forms planner $CuO_4$ and further, ∠O-Cu-O are same. In contrast, the second lowest energy structure[12] which has different XRD from others also has different ∠O-Cu-O, in which Cu forms pyramidal $CuO_4$ tetrahedra.

## 3.4 $Sn_2O_3$

Although the existence of $Sn_2O_3$ has been reported for more many years,[108] unfortunately, to date, the crystal structures of it is not unambiguously determined. Recently, probable monoclinic crystal structures it been predicted.[109,110] Due to the absence of atomic configurational information in the literatures, the predicted structure[109,110] could not be compared. The predicted structures, although show good agreement with each other, are different from the first proposed triclinic structure by Murken et al.[111] A good agreement between theoretical and experimental XRDs of $Sn_2O_3$ has been claimed,[109] however, crystal systems, lattice parameters, and number of

formula unit in the cell differ significantly in two cases. Despite this fact, Sn atom in the predicted structure exhibits a mixed-valence state which is consistent with experimental result.[112] Under such circumstances, we intend to predict or at least verify the crystal structures of $Sn_2O_3$. For this task, more than 250 motif structures were considered for DFT followed by vdW-DFT optimization. The pathway to form motif structures for $Sn_2O_3$ is shown in Figure 3.3. and the formation of unit cells from existing structures has been explained in reference.[12,92]For the convenience of computation, initially, only DFT was employed for structural relaxation of probable structures of $Sn_2O_3$. Then DFT-derived few most probable structures were exposed to empirical vdW correction. Based on the lowest energy calculated by DFT, the ground state structure was predicted.

After optimization, $SnO_2$ (mp-560417) derived structure was determined as lowest energy structure for $Sn_2O_3$ (see Figure 3.4), which was derived by removal of middle layer of four O atoms from mp-560417. The energies, volumes, and lattice parameters of few most DFT-vdW predicted probable structures are shown in Table 3.2. StructurePredictor generated structures possess energies higher than those of structures presented in Table 3.2, and hence, were not presented therein. The lowest energy structure is energetically close to SnO (mp-545820) motif structure and same to reference;[109] all these three structures have monoclinic symmetry. Moreover, the predicted structure in the present study belong to same space group (S.G. 14, $P2_1/c$) as the previously predicted structures.[109,113] The only difference between those is the orientation of the axes; the 'c' axis (β) in our structure corresponds to 'a' axis ($180^o$ - β) in reference[109,113] or vice versa. Therefore, our work verifies the predicted structure as the crystal structure of $Sn_2O_3$ with small deviations in lattice parameters. As for the two lowest energy structures the energy difference is only 0.031 eV,[92] we further calculate the Gibbs free energies (G) of those at room temperature (T = 300 K) using the thermodynamic

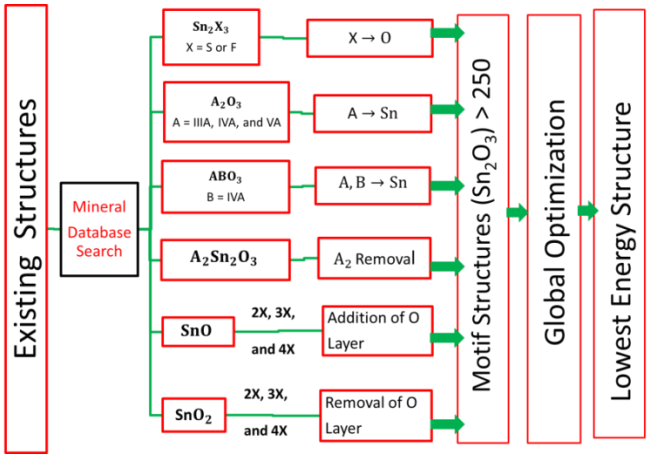


Figure 3.3 Evolution of different 'Motif Structures' of $Sn_2O_3$. 'nx' (n=2, 3, and 4) indicates that original structures, which had Z=1(Z = No. of formula unit) in the cell, were doubled, tripled, and quadrupled to form motif structures; structures having Z=2 in the cell were doubled only.

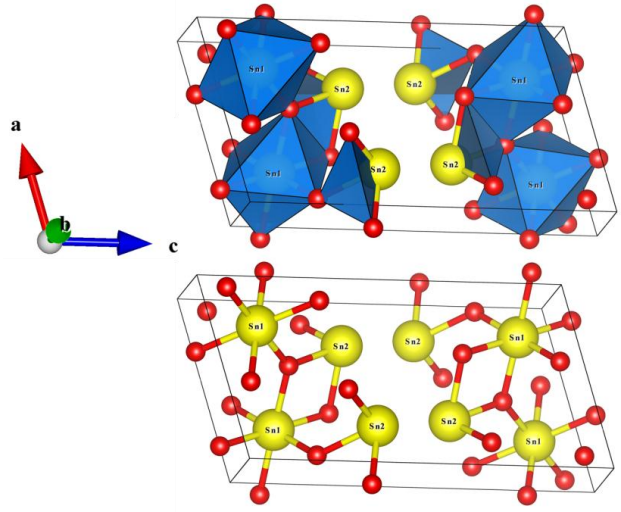


Figure 3.4 Crystal structure of $Sn_2O_3$, derived from one of the $SnO_2$ (mp-560417) polymorphs. Sn1 and Sn2 atoms correspond to Sn (IV) and Sn (II) oxidation states in $Sn_2O_3$, respectively. A 13x15x7 k-point sampling was used for $Sn_2O_3$ in DFT and DFT-D2 geometry optimization.

Table 3.2 vdW-DFT predicted energies, volumes, and lattice parameters of few most probable structures of $Sn_2O_3$. The formation enthalpies, $\Delta H_f$ were calculated with respect to bulk Sn and molecular $O_2$ phases following the method described in reference.[12] The '(n = an integer)' in the fourth column represents the ranking of the corresponding free energy; the stability of each probable structures runs from most to lowest with the ascending order of n.

| Existing Structures | | Polymorphs in 'Materials Project' Database | Formula unit (Z) | $\Delta H_f$/Z (eV) | Vol./ Z ($Å^3$) | Relaxed lattice parameters | | | | | |
|---|---|---|---|---|---|---|---|---|---|---|---|
| | | | | | | A (Å) | B (Å) | C (Å) | α (°) | β (°) | γ (°) |
| $ASnO_3$ (A=) | Ti | mp-754246 | 6 | -9.170 (7) | 81.73 | 5.41 | 5.38 | 19.38 | 90.00 | 90.00 | 120.00 |
| | Cd | mp-754329 | | | | | | | | | |
| | Ca | mp-4190 | | | | | | | | | |
| | Mn | mp-25005 | | | | | | | | | |
| $CdGeO_3$ | | mp-8275 | | | | | | | | | |
| $A_2O_3$ (A=) | Al | mp-7048 | 4 | -8.951 (8) | 76.60 | 3.25 | 14.13 | 7.57 | 61.58 | 90.00 | 90.00 |
| | Ga | mp-886 | | | | | | | | | |
| $SnO_2$ | | mp-560417 | 4 | -9.486 (1) | 75.60 | 5.77 | 4.87 | 11.21 | 90.00 | 106.20 | 90.00 |
| | | mp-12978 | | -9.382 (3) | 74.95 | 9.65 | 5.37 | 5.78 | 90.00 | 90.00 | 90.00 |
| | | mp-856 | | -9.279 (5) | 75.50 | 4.80 | 9.54 | 6.60 | | | |
| | | mp-550172 | | -9.279 (5) | 75.50 | 6.60 | 9.53 | 4.80 | | | |
| | | mp-697 | | -9.375 (6) | 71.11 | 10.40 | 5.22 | 5.24 | | | |
| SnO | | mp-545820 | 4 | -9.455 (2) | 74.87 | 4.88 | 5.78 | 10.67 | 84.83 | 90.00 | 90.00 |
| Ref.[109] | | | 4 | -9.486 (1) | 75.61 | 11.08 | 4.87 | 5.77 | 90.00 | 76.20 | 90.00 |

equation, G = H-TS. Here H is the enthalpy which corresponds to formation enthalpies, $\Delta H_f$ of $Sn_2O_3$ in Table 3.2; S is the entropy which was calculated using Phonopy.[114]

The entropy S was calculated from phonon frequency (force constants were determined by finite displacement method) within harmonic approximation on a sampling mesh (31x31x31) in the reciprocal space. It was found that the energy difference (0.031 eV) and stability order of those structures do not alter even at room temperature. This confirms that $SnO_2$ (mp-560417) will remain as the most stable structure even with the presence of thermal vibration.

## 3.5 $Cu_2ZnSn(S_{1-x}Se_x)_4$ (CZTSSe)

CZTSSe is the most promising photovoltaic material in $Cu_2ZnSnS_4$ (CZTS)/ $Cu_2ZnSnSe_4$ (CZTSe) family. It is an alloy of S and Se, keeping the cationic ordering fixed as in their parent structures, CZTS and CZTSe; the mixing ratio of S and Se, x determines its PV performance, which is yet to be optimized. As we will be knowing in the next chapter that x = 0.5 $\pm$ 0.125 should be the optimized range of alloy mixing in achieving the maximum PV efficiency form it, knowing crystal structures of those alloy composition are prerequisite for any theoretical study. Since the crystal structures of x = 0.5 $\pm$ 0.125 compositions are unknown, our investigations begins with determining those at first. To model crystal structures of CZTSSe x=0.375 and 0.625 in conjunction with x=0.5 a kesterite-CZTS unit cell was chosen wherein S atoms were replaced by Se atoms according to different alloy composition values x. All possible combinations of S and Se per unit cell producing different CZTSSe structures were considered for geometry optimization. However, cations-ordering was kept fixed as those in CZTSSe adopt kesterite configurations as well.[115–121] Figure 3.5 represents DFT+U-determined lowest energy structures of CZTSSe for x=0.375, 0.5, and 0.625, which have been determined

for the first time while x = 0.5 structure is consistent with the previous result.[17] In the present work, we have used $U_{eff}$ = 6 eV to both Cu 3d and Zn 3d orbitals in order to correct the DFT description of 3d based compounds. A 13×13×7 K-point sampling was used for ionic relaxation of CZTSSe.

The x = 0.375 and 0.625 lowest energy structures involve two different arrangements of S and Se atoms along 'c' axis. Considering 'A' and 'B' are as reference points these arrangements are SS-SeSe-SS and Se-SSS-Se along '(+)c' axis for x = 0.375 while S and Se are just interchanged in x=0.625. In contrast, S and Se have one arrangement which is SS-

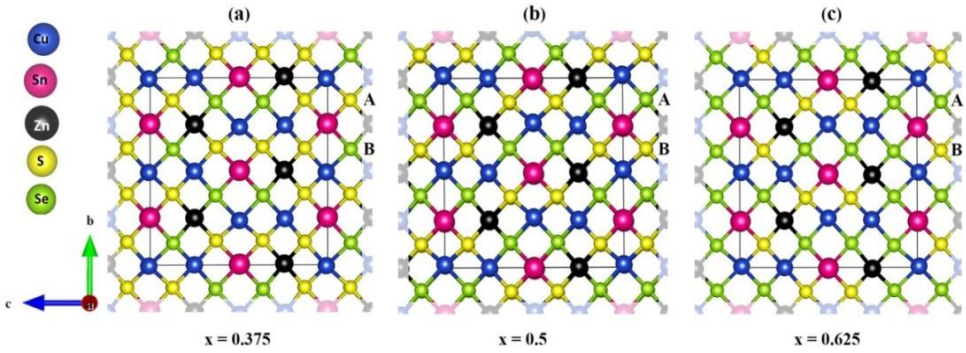


Figure 3.5 Crystal structures of CZTSSe for three different alloy compositions: (a) x = 0.375, (b) x = 0.5, and (c) x = 0.625. A and B are the two reference points for each composition from which two different S-Se arrangement along positive 'c' can be viewed.

SeSe in the '(+)c' direction for x = 0.5 lowest energy structure. All these different arrangements irrespective of alloy compositions keep alternating along 'b' axis.

Achieving the single phase crystallinity of these alloys as shown in Figure 3.5 is one of the primary criteria for enhanced solar-to-current conversion efficiency, however, it is often hard in practice, especially for a compound like CZTSSe comprising multi-

catinos-anions. The single-phase formation with least defects ensures maximum crystallinity in the samples, which will be discussed in the next chapter.

## 3.6 Conclusion

In this chapter, we have successfully predicted the crystal structures of different composition through mineral database search. The existing structures in the database were chosen for generating the unit cell of the desired stoichiometry through several manipulations. Those unit cells were later exposed to DFT/DFT+U/vdW-DFT optimization and the lowest energy structure was considered as the most probable crystal structure. Two of our predicted structures ($AgBiW_2O_8$ and $CuBiW_2O_8$) were experimentally verified. Although our method was primarily developed and successful in predicting crystal structures in the form of $ABW_2O_8$, can be extended to other stoichiometry as well; one real example of that is the crystal structure prediction of $Sn_2O_3$.

# Chapter 4

## Thermodynamic Phase Stability and Optimal Growth Conditions

### 4.1 Binary Compound: $SnO_x$

#### *4.1.1. Introduction*

SnO decomposes into $SnO_2$ and Sn above a certain temperature (> $300^0$C [111,122]) either directly or through intermediate phases. This phase transition, although has been known for a century, is not well understood yet. Moreover, various chemical formulae for these intermediate $SnO_x$ ($1< x < 2$) phases have been proposed without reaching a conclusion. Some studies[108,123] proposed $Sn_3O_4$ as the stoichiometry of the intermediate $SnO_x$ phase, while $Sn_2O_3$ chemical formula was proposed by others.[111,124] Though $Sn_5O_6$ chemical formula has also been mentioned as another probable intermediate $SnO_x$ phase,[125] not much information is available of it. Several studies verified $Sn_3O_4$[122,126–129] and $Sn_2O_3$[130] as the correct intermediate $SnO_x$ phase. At this point, a valid question arises: why is a general consensus absent on measured stoichiometry of intermediate $SnO_x$ phases? The answer of this question calls for a methodical investigation of SnO → $SnO_2$ phase transition. However, although many studies have reported the SnO decomposition followed by the formation of various $SnO_x$ phases while annealing at oxygen environment, the SnO to $SnO_x$ phase transformation process is still not well explained. Further, to the best of our knowledge, no theoretical study has been done thus far in this regard. These motivated us to pursue the present work which primarily intends to investigate the chemical mechanisms of SnO to $SnO_x$ phase transformation with respect to different oxygen growth conditions by means of *ab initio* calculation.

*4.1.2. Computational Details*

In addition to DFT, we have employed van der Waals (vdW) correction as implemented in VASP code The reason to incorporate empirical vdW correction in our calculations to compensate well-known failure[93–95] of DFT or hybrid-DFT or Hartree-Fock methods in taking account of non-bonded dispersion interaction between the layers in layered structures.[96–99] SnO is well known layered structure; $Sn_3O_4$ and $Sn_2O_3$, which are integral parts of the present investigation, have been reported as Sn (II, IV)-oxides and hence possess layered structural framework as well. Therefore, these three tin-oxides warrant vdW correction for all DFT and post-DFT calculations as well. However, to the best of our knowledge, $Sn_3O_4$ and $Sn_2O_3$ were not treated with any sort of empirical vdW correction thus far. Therefore, SnO is our reference material for optimal parameterization of vdW corrections. Among many existing flavors of vdW correction, a method introduced by Grimme[100] and implemented in VASP as DFT-D2 has been a popular choice for a wide class of systems due to its satisfactory results in conjunction with computational efficiency.[101–105] DFT-D2 indeed shows an improvement, but limited, over DFT results of SnO. A slight modification[131] of damping function in Grimme method reproduces experimental lattice constants quite well; however, the underestimation of the band gap without vdW correction was prevailed. This issue was resolved[132] by incorporation of a hybrid flavor namely, PBE0 with modified-DFT-D2. Since modification[131] of damping function is not available in VASP, we employ original DFT-D2 with a different hybrid flavor (HSE06[133]), intending to reproduce experimental results for SnO as precise as possible in the present calculation. For this purpose, we have used three different amount of exact exchanges (α =25%, 35%, and 40%) with the incorporation of plane-waves basis sets of a kinetic energy cut-off of 800 eV. The ion positions and volumes were always relaxed without any symmetry constraint to allow the internal geometry and the shape of the

lattice to be changed freely until the force on each of the ion was 0.001 eV/Å or less This criteria is consistent with the previous vdW *ab initio* calculations[131,132] for SnO. A comparison of three different α-induced DFT-D2-HSE06 calculations of SnO is shown in Table 4.1. This shows that, not only does α = 40% reproduce experimental lattice constants quite well, improves the fundamental indirect band gap of SnO as well. Although it overestimates the direct band gap, we keep α = 40% for the rest of DFT-D2-HSE06 calculations because of its better correction in c/a ratio and fundamental gap.

Table 4.1 A comparison of structural and band gap attributes of SnO between calculated (with vdW correction) and experimental results.

| Exact exchange | Lattice Constants (Å) | | | | | | Band Gaps (eV) | | | |
|---|---|---|---|---|---|---|---|---|---|---|
| | D2-HSE06 | | | Exp.[134–137] | | | D2-HSE06 | | Exp.[138–140] | |
| | a | c | c/a | a | C | c/a | Indirect | Direct | Indirect | Direct |
| 25% | 3.839 | 4.872 | 1.269 | 3.799-3.803 | 4.827-4.838 | 1.271-1.272 | 0.34 | 2.76 | 0.7 | 2.5-3 |
| 35% | 3.819 | 4.852 | 1.271 | | | | 0.29 | 2.83 | | |
| 40% | 3.809 | 4.842 | 1.271 | | | | 0.36 | 3.06 | | |

For DFT-D2-HSE06 calculations, the used k-point samplings were 3x4x2, 3x3x5, 3x3x5, and 5x5x4 for $Sn_2O_3$, $Sn_3O_4$, $SnO_2$, and SnO, respectively. The crystal structure of

$Sn_2O_3$ has been determined in the previous chapter while that of $Sn_3O_4$ was taken from Reference.[109]

*4.1.3. Phase Stability and Optimal Growth Conditions*

It has been reported that Sn (II)- to Sn (IV) transition can occur either as (i) SnO→$SnO_2$ through single oxidation state or as (ii) SnO →intermediate phase →$SnO_2$ through two oxidation states depending on the film deposition temperature,[141] initial content of the oxygen,[142] and annealing temperature.[141,142] In the case of multi-steps phase transition, an intermediate phase exists between 400-550$^0$C,[122,130,142] co-exists with $SnO_2$ between 500-600$^0$C,[122,130,141–143] and transforms into $SnO_2$ eventually either at a temperature above 600$^0$C with post-annealing at oxygen rich condition[142] or at further heating (T = 700$^0$C ) in air.[122] In the present work, we intend to realize the formation of different $SnO_x$ ($1 < x \leq 2$) phases and their transition from one phase to another with respect to the free energies of Sn and O. In Figure 4.1, lines representing Sn-O phases have been drawn with respect to their chemical potentials (Gibbs free energies) given in equations (4.1-4.4); these equations represent the necessary conditions of corresponding Sn-O phases to be formed at thermodynamic equilibrium.

SnO: $\Delta\mu_{Sn} + \Delta\mu_O = \Delta H_{f,SnO}$ = -2.358 eV, 4.1

$Sn_3O_4$ : $3\Delta\mu_{Sn} + 4\Delta\mu_O = \Delta H_{f,Sn_3O_4}$ = -9.736 eV, 4.2

$Sn_2O_3$: $2\Delta\mu_{Sn} + 3\Delta\mu_O = \Delta H_{f,Sn_2O_3}$ = -7.317 eV, 4.3

$SnO_2$: $\Delta\mu_{Sn} + 2\Delta\mu_O = \Delta H_{f,SnO_2}$ = -4.865 eV 4.4

$\Delta H_{f,SnO_x}$ in the above equations are the formation enthalpies of corresponding $SnO_x$ phases calculated with respect to bulk Sn and molecular $O_2$ phases.[12] In Figure 4.1, points in the area under (towards the axes) each line can correspond to non-equilibrium growth conditions for that $SnO_x$ phase. Under such conditions, the formation of that

phase is possible if kinetics allow it to be formed. In contrast, the area above (outwards from the axes) of each line corresponds to growth conditions not suitable enough for that $SnO_x$ phases to be formed. Since equations (4.1-4.4) are valid only at thermodynamic equilibrium, SnO to $SnO_2$ phase transition thermodynamically would possible only and if only a smooth transition between those respective lines is possible. Since this is not the case in Figure 4.1a and 4.1b, imposing non-equilibrium conditions such as heating would require to proceed SnO to $SnO_2$ phase transition; $T > 300^0C$ is required for the decomposition of SnO, in fact. Since all DFT calculations are done at T = 0 K, any sort of non-equilibrium description of this phase transition will be beyond the scope of the present discussion. Therefore, our discussion starts at a point from which onward the SnO to $SnO_2$ phase transition can be realized at thermodynamic equilibrium condition. In doing so, we assume that the decomposition of SnO was accomplished by means of a non-equilibrium process, and the decomposed phases thereafter were brought down into thermal equilibrium. With this assumption it is possible to realize the formation and transformation of different post SnO-decomposed phases and hence, would be enough to elucidate the SnO to $SnO_2$ phase transition. Moreover, since SnO to $SnO_2$ transformation depends on initial content of oxygen and annealing at oxygen atmosphere as stated above, the difference in growth conditions at different points in Figure 4.1 can primarily be thought of controlling oxygen growth (tuning oxygen pressure) condition in practice.

Our following phase transition discussion can be divided into two parts (see Figure 4.1a): growth zone 1 or GZ1 ($-2.44\ eV \leq \Delta\mu_O \leq -2.4\ eV$), and growth zone 2 or GZ2 ($-2.4\ eV < \Delta\mu_O \leq -0\ eV$). In GZ1, at thermal equilibrium, $SnO_2$ – line intersects with $Sn_2O_3$- and $Sn_3O_4$- lines. In contrast, no such intersection between the lines is observed in GZ2. This tells that equilibrium consideration of $SnO \rightarrow SnO_2$ phase transitions are

realized only in GZ1 i.e., at relatively oxygen poorer and Sn-rich ($\Delta\mu_{Sn} \approx 0$) conditions. Hence, our phase transition discussion is primarily restricted to this region only. For the sake of better visibility, GZ1 is presented separately in Figure 4.1b where points A, C, and F correspond to the required oxygen growth conditions to form $SnO_2$, $Sn_3O_4$ and $Sn_2O_3$, respectively at Sn-rich condition; points B ($\Delta\mu_{Sn}$ = -0.006 eV and $\Delta\mu_O$ = -2.43 eV) and E ($\Delta\mu_{Sn}$ = -0.039 eV and $\Delta\mu_O$ = -2.413 eV) represent growth conditions at which two intermediate $SnO_x$ phases co-exist with $SnO_2$; points D, G, and R are merely arbitrarily chosen, just as a matter of convenience.

Let's consider any point along AB line as a starting point of the phase transition at which a thermally equilibrium phase of $SnO_2$ singly exists. Since AB can be reached directly from SnO-line (although involves non-equilibrium process), points along that can be thought of necessary growth conditions for happening direct SnO→$SnO_2$ transition. No other point in Figure 4.1 allows to that happen. This implies that oxygen-poor growth condition must require for direct transition to proceed. A slight change of oxygen-growth condition (towards richer) would transform point A into point B at which $SnO_2$ would co-exist with $Sn_3O_4$. If oxygen annealing continues along BE growth conditions, $SnO_2$ + $Sn_3O_4$ will transforms into $SnO_2$ before coming to point E. This completes the indirect phase transition at oxygen poor growth condition. Since point A and point B are energetically so close, the latter rather than the former could be the starting point of indirect transition. In such case, indirect transition proceeds as SnO $\xrightarrow{heat}$ $SnO_2$ + $Sn_3O_4$ $\xrightarrow{annealing\ at\ O_2\ atmoshphre}$ $SnO_2$; however, that would require precise tuning of the growth conditions. Otherwise, $SnO_2$ being ended up at E would co-exist with $Sn_2O_3$. This indeed could be often outcomes in experiments as points B and E are energetically not significantly different, and experimental precision therefore might fail to capture the variation between those points. Further, since $Sn_2O_3$ is comprised of SnO and $SnO_2$

structures locally, the co-existed phase at E would be nothing but $SnO_2 + Sn_2O_3 \rightarrow SnO_2 + SnO + SnO_2 \rightarrow 2SnO_2 + SnO$. Therefore, during the indirect phase transition at oxygen poor growth condition, $SnO_2$ has higher probability to contain a certain portion of SnO. In contrast, further annealing in O-rich conditions along ER at the same annealing temperature would leave $SnO_2$ to be existed alone. These explain the experimental facts,[143] why $SnO_2$ contains a certain amount of SnO, or forms as a purely polycrystalline phase during indirect transition proceeded at two different oxygen annealing growth conditions, although annealing temperature is same. Further, point E could be growth conditions which lead to the formation of amorphous Sn-O ($SnO+SnO_2$) phase as found experimentally after post-annealing in $O_2$ atmosphere at $500^0$C.[142]

Besides transforming into $SnO_2$, transition to intermediate phases ($SnO \rightarrow Sn_3O_4$ / $Sn_2O_3$) is also possible. While $SnO \rightarrow Sn_3O_4$ can be achieved through both direct and indirect pathways, $SnO \rightarrow Sn_2O_3$ invokes multiple-steps, thereby transforming only indirectly. The reason is, a direct hoping from SnO- to $Sn_3O_4$ - line, although involves non-equilibrium process, is possible; however, $SnO \rightarrow Sn_2O_3$ requires to overcome both SnO and $Sn_3O_4$ lines as shown in Figure 4.1a and 4.1b. In the case of direct transition, points along BD onwards correspond to growth conditions those make $SnO \rightarrow Sn_3O_4$ to happen. In indirect $SnO \rightarrow Sn_3O_4$ transition, if B is the starting point of thermal equilibrium process, viable pathways are either BD or BC. However, annealing at further and further oxygen-rich along BD would be preferable for more crystalline and stable single-phase $Sn_3O_4$. This indirect phase transition can be seen as $SnO \xrightarrow{heat} SnO_2 + Sn_3O_4 \xrightarrow{annealing\ at\ O_2\ atmoshphre} Sn_3O_4$. During $SnO \rightarrow Sn_2O_3$ phase transition, the first intermediate phase would be either $SnO_2$ (AB) or $SnO_2 + Sn_3O_4$ (B) or $Sn_3O_4$ (BC). Among those, point B would be most desirable as it requires only one more step to reach at point E where $SnO_2$ starts to transform into $Sn_2O_3$; the complete transformation

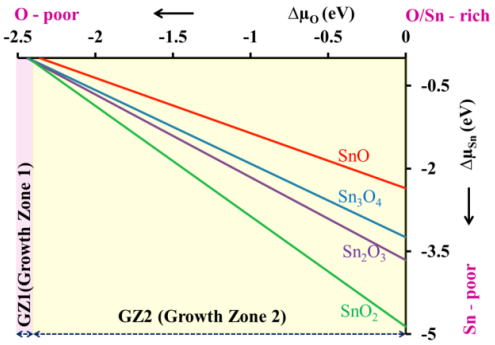


(a)

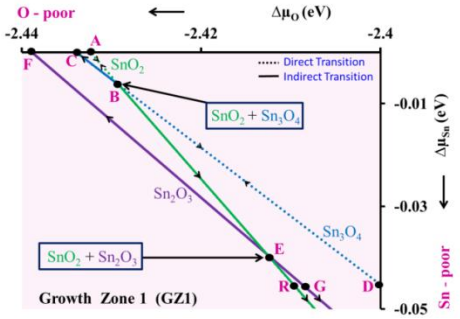


(b)

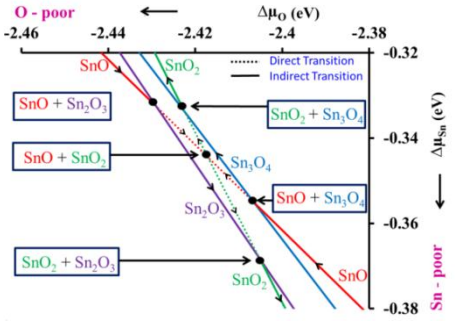


(c)

Figure 4.1 The formation of different $SnO_x$ phases with respect to Sn and O growth conditions. Figure b is the magnified version of GZ1in Figure a. It is clear that all the phase transformations are occurring in the relatively O-poor and Sn-rich growth conditions. Figure c is also the magnified version of GZ1 while no vdW correction was incorporated. The broken line represents direct transition from SnO-to-$SnO_x$ or vice versa.

requires further tuning of growth conditions either along EF or EG. Like $Sn_3O_4$, annealing at oxygen richer condition i.e., EG would provide more controlling on $Sn_2O_3$ structural and hence opto-electronic attributes. This indirect phase transition can be seen as $SnO \xrightarrow{heat} SnO_2 + Sn_3O_4 \xrightarrow{annealing\ at\ O_2\ atmoshphre} SnO_2 + Sn_2O_3 \xrightarrow{annealing\ at\ O_2\ atmoshphre} Sn_2O_3$. Compared to the thermodynamic formation of both intermediate phases, it is obvious that formation of $Sn_2O_3$ is more sophisticated than that of $Sn_3O_4$ since the latter (i) can be formed directly, (ii) invokes lesser intermediate steps during indirect transition, and (ii) forms at first followed by the former. For these reasons, the synthesis of $Sn_3O_4$ is probably more frequent than that of $Sn_2O_3$.

A similar plot of GZ1 is presented in Figure 4.1c which does not incorporate vdW correction empirically. The calculated (DFT) $\Delta H_{f,SnO_x}$ in Equation 4.1-4.4 would be -2.762 eV, -10.691 eV, -7.952 eV, and -5.179 eV for SnO, $Sn_3O_4$, $Sn_2O_3$, and $SnO_2$, respectively. In this figure, both SnO and $SnO_2$ lines intersect with each other including lines of intermediate phases. This implies that the transformation of SnO-to-$SnO_x$, even $SnO_2 \rightarrow SnO$, can be happened without involving any non-equilibrium process. However, this is not the case in reality. For example, $SnO_2 \rightarrow SnO$ decomposition requires T $>1500^0$C.[144] Therefore, empirical vdW correction of SnO is required to reproduce the correct mechanism of SnO-to-$SnO_x$ phase transition.

It is worth to note that $Sn_2O_3$ and $Sn_3O_4$ lines in Figure 4.1 never intersect with each other i.e. in principle these two phases never co-exist at thermodynamic growth conditions. However, the distance between the two lines (difference in growth conditions) is very small, minimum at O-poor conditions. Hence, due to the narrow window of growth conditions, $Sn_2O_3$ and $Sn_3O_4$ phases can be transformed into each other within the experimental limitation; in addition, any of those intermediate phases can co-exist with $SnO_2$ depending on initial oxygen conditions, points B ($SnO_2$ + $Sn_3O_4$ ) or E ($SnO_2$ +

$Sn_2O_3$). As a result, it would be extremely hard to distinguish between $Sn_2O_3$ and $Sn_3O_4$ as intermediate $SnO_x$ phases experimentally; different stoichiometry of intermediates $SnO_x$ phases in different experiments indeed corroborate this conclusion. Further, although Figure 4.1 depicts possibility of direct SnO → $SnO_2$ phase transition in GZ1, could be extremely difficult to achieve that in practice at thermodynamic equilibrium. The ranges of required growth conditions (AB) to allow SnO → $SnO_2$ directly might not be significantly large enough to overcome the experimental limit for precision control. Hence, there will be potential probability of SnO to $SnO_2$ phase transition to be accompanied by other intermediate $SnO_x$ phases. *Any chemical formula ($Sn_2O_3$ or $Sn_3O_4$) of the intermediate phases could be possible outcome during the measurement depending on the initial thermal equilibrium growth conditions and annealing condition (oxygen rich/poor), considering it as a fact rather than a matter of measurement inconsistency.*

### *4.1.4. Conclusion*

In conclusion, oxygen growth condition determines the pathway of SnO-to-$SnO_x$ phase transition, whether in one step (through Sn(II) → Sn(IV)/Sn (II, IV) oxidation state) or multi-steps (through Sn(II) → Sn(II,IV) → Sn(IV) oxidation states). It is important to note, all the phase transitions occur only at sufficient O-poor growth conditions, -2.44 eV < $\Delta\mu_o$ < -2.40 eV. Since this range of oxygen chemical potential is very small, a slight change of growth conditions would transforms intermediate $SnO_x$ phases one form to another. This explains why different stoichiometry of intermediate tin-oxides ($Sn_3O_4$ or $Sn_2O_3$) in different measurement was achieved. Further, it was shown that vdW correction of SnO needs to be incorporated to demonstrate the experimental feats.

## 4.2. Ternary Compounds

### *4.2.1 $CuBi_2O_4$*

#### 4.2.1.1 Introduction

As a visible light active p-type semiconductor, $CuBi_2O_4$ is of potential interest as a component in water splitting tandem photocatalysts for the generation of hydrogen fuel. It has an optical band gap of 1.8 eV.[145] In 2007, Arai et al, identified $CuBi_2O_4$ during a combinatorial screening as a potential proton reduction photocathode.[146,147] Unlike the Delafossites, $CuBi_2O_4$ contains stacks of square planar $Cu(II)O_4$ groups linked to distorted trigonal $Bi(III)O_6$ polyhedra.[148] Although $CuBi_2O_4$ has been reported[147,149] as a p-type semiconductor based on photocurrent measurements, the true origin of that is not known yet. Further, despite the fact that p-$CuBi_2O_4$ shows the potential for photoelectrochemical applications, has the limitations as a proton reducing photocathode.[150] Besides the origin of p-type activity, the photophysical properties of p-$CuBi_2O_4$ and its limitations as a proton reduction photocatalys can be understood with help of chemical potential analysis and defect calculations.

#### 4.2.1.2 Computational Details

All calculations of $CuBi_2O_4$ were done using DFT+U; the effective value of U was chosen as 6 eV($U_{eff}$ =U–J=7–1=6 eV, J=Stoner exchange parameter) to be consistent with the previous work of a Cu-Bi-O derived compuound.[12] A 9 x 9 x 13 Monkhorst–Pack[77] $k$-point sampling was used for ion relaxation. For the defect calculations,[17] we constructed a supercell containing 152 atoms, the used k-mesh for that was 5×3×5.

#### 4.2.1.3 Single-Phase stability, Defects, and Effective Growth Conditions

Figure 4.2(right) represents the chemical potential landscape of $CuBi_2O_4$, which demonstrates a very narrow growth region (ABC-yellow region) of its single-

phase formation. The probability of forming various charged neutral different defects with respect to ABC growth region is shown on the left of Figure 4.2. Defects calculations show that all cationic and intrinsic defects have higher formation energies ($\Delta H(\delta) \geq 1.36$ eV, $\delta$ = a single intrinsic defect) at single-phase growth conditions. Cu vacancies ($V_{Cu}$) and Cu substitution on Bi ($Cu_{Bi}$) sites are the most probable defects at oxygen-rich single phase growth conditions

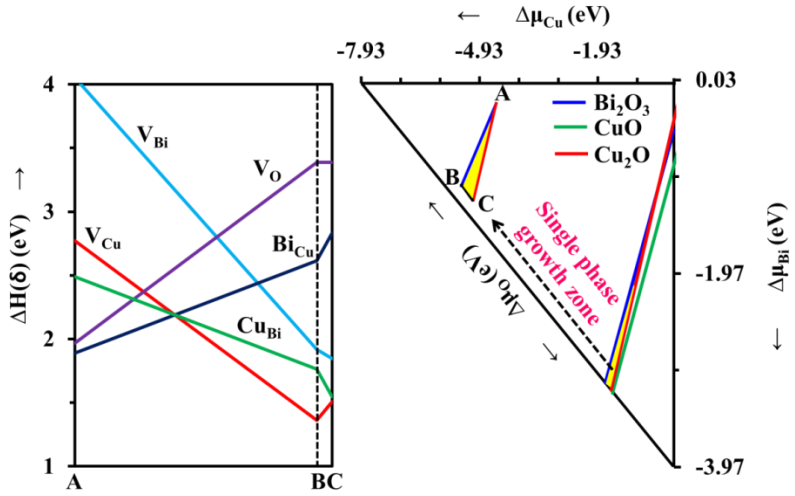


Figure 4.2 The left figure represents the probability of forming different intrinsic defects in $CuBi_2O_4$ with respect to its single-phase growth region (see yellow bounded region at right figure); the yellow region in the left figure was achieved using the chemical potenial landscapre analysis (see ref.[17]). In the right figure, $\Delta\mu_\alpha$ ($\alpha$ = Cu, Bi, and O) axes correspond to growth conditions, from rich ($\Delta\mu_\alpha$ = 0 eV) to poor ($\Delta\mu_\alpha$ = formation enthalpy), of respective species. The values of A, B, and C in the figure are ($\Delta\mu_{cu}$ = -0.33 eV, $\Delta\mu_{Bi}$ = -0.96 eV, $\Delta\mu_O$ = -1.42 eV), ($\Delta\mu_{cu}$ = -1.74 eV, $\Delta\mu_{Bi}$ = -3.10 eV, $\Delta\mu_O$ = 0 eV), and ($\Delta\mu_{cu}$ = -1.60 eV, $\Delta\mu_{Bi}$ = -3.17 eV, $\Delta\mu_O$ = 0 eV), respectively.

(formation energies ~ 1.5 eV), but only the $V_{Cu}$ reproduce the experimentally observed optical band gap of 1.75 eV (the band structure of $CuBi_2O_4$ with Cu

substitution defects is shown in Figure 1 in Appendix A). These Cu vacancies also lead to empty states in the $CuBi_2O_4$ valence band, explaining the observed p-type activity of the material. According to the p-DOS diagram (see Figure 2 Appendix A), the valence and conduction band edges of $CuBi_2O_4$ arise primarily from the combination of O 2p and Cu 3d orbitals, respectively, with additional contributions from the Cu 3d and Bi 6s orbitals just below the Fermi level. Trapping of photoelectrons in the Cu 3d band is the cause for the observed reductive photocorrosion of the material. The photocorrosion rate may further get higher if the presence $Cu_{Bi}$ can not be minimized. Because, this defect introduces defect states near conduction band which may act as electron trapping centers as well in addition to Cu 3d states near the conduction band edge. Therefore, for optimal performance of $CuBi_2O_4$, it is needed to employ a set of growth conditions which would maximize p-type activity with lesser intermediated defect levels introduced by $Cu_{Bi}$. Such an effective growth conditions could be towards B from A in Figure 4.2.

4.2.1.4 Conclusion

In conclusion, since $V_{Cu}$ is not spontaneous (see Figure 4.2(left)) with respect to single-phase growth zone, the p-type activity in $CuBi_2O_4$ should not very significant. To achieve the maximum the p-type activity, the chosen growth conditions should intensify the formation of $V_{Cu}$. In addition, it has to ensure that such a growth conditions further limit the formation of detrimental defects. According to our chemical potential landscape analysis in conjunction with defect calculation, the preferable growth conditions would be $\Delta\mu_{cu} \leq -1.74$ eV, $\Delta\mu_{Bi} \geq -3.10$ eV and $\Delta\mu_O \approx 0$ eV. These findings should facilitate the synthesis of p-$CuBi_2O_4$ with an improved photophysical and better proton reduction properties.

*4.2.2 α-$SnWO_4$*

4.2.2.1 Introduction

α-$SnWO_4$ (1.64 eV)[151] is also an promising n-type photocatalyst in which valence band is formed by the hybridization of the Sn 5s and O 2p orbitals and the conduction band is mainly composed of W 5d orbitals. A materials of such orbital hybridization often induces the formation of large-polaron carriers which in turn result relatively high charge carrier mobilities in those orbital comprising materials.[152] However, the photocatalytic performance of this material is not very optimistic by far; one of the reasons is the presence of $Sn^{4+}$ defect in the synthesized sample. Therefore, a due attention should be paid in synthesizing α-$SnWO_4$ so that the concentration of $Sn^{4+}$ can be minimized in the given growth conditions. A prediction of suitable growth conditions can guide the experimentalist in this regard, and it was attempted in the following discussion in terms of chemical potential landscape analysis with the defect calculations

4.2.1.2 Computational Details

For α-$SnWO_4$, only DFT was employed. A 11 x 5 x 11 Monkhorst–Pack[77] $k$-point sampling was used for ion relaxation. For the defect calculations, we constructed a supercell that contains 96 atoms and the used k-mesh for all defects-induced calculations was 3×3×5.

4.2.1.3 Single-Phase stability, Defects, and Effective Growth Conditions

Figure 4.3(right) represents the chemical potential landscape of α – $SnWO_4$, in which the yellow region (ABC) represents its single-phase formation growth conditions. From the figure, it is seen that it has higher single-phase stability than that of. $CuBi_2O_4$. Despite the fact, $\Delta H_{f,\alpha-SnWO_4} \leq \Delta\mu_O$ (eV) ≤ 0 ($\Delta H_{f,\alpha-SnWO_4}$= formation enthalpy of α – $SnWO_4$), a reduced oxygen growth conditions ($\Delta H_{f,\alpha-SnWO_4} \leq \Delta\mu_O$ (eV) ≤ 0) were

set in order to get better perspective of the single-phase zone. Moreover, ABC is the only growth region in which α – $SnWO_4$ forms as a single-phase. Therefore, -2 ≤ $\Delta\mu_O$ (eV) ≤ 0 growth conditions are redundant to the present discussion. Because of reduced oxygen growth conditions, the cationic axes are also limited to -3.51 ≤ $\Delta\mu_{Sn,W}$ (eV) ≤ 0. The probability of forming various intrinsic defects in α – $SnWO_4$ with respect to its single-phase growth zone is depicted in Figure 4.3. In left figure , the defects have positive

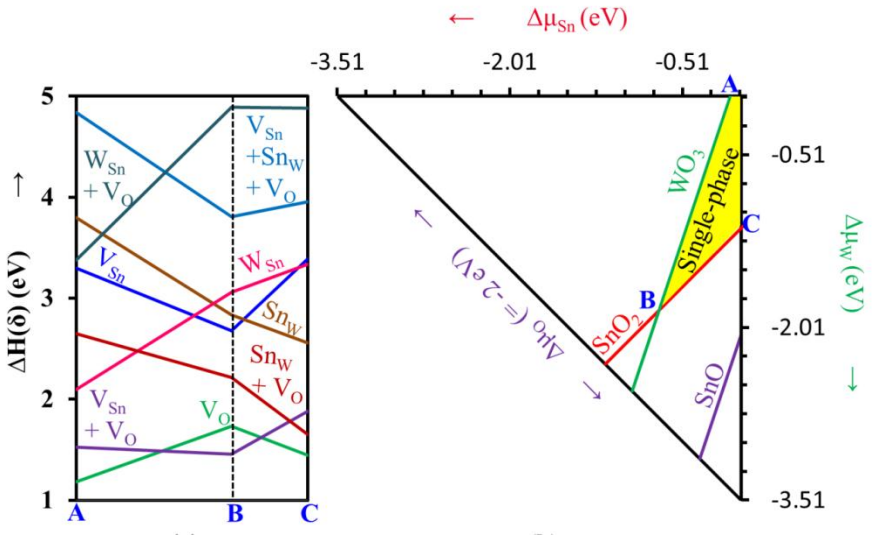


Figure 4.3 The defects formation energies and chemical potential landscape analysis of α-$SnWO_4$. The left figure represents the probability of forming different intrinsic defects in α-$SnWO_4$ with respect to its single-phase growth region (see yellow bounded region on the right figure). In the right figure, $\Delta\mu_\alpha$ (α = Sn, W, and O) axes correspond to growth conditions of respective species.

formation energies and the most probable defect is O vacancy ($V_O$); all other defects including cationic vacancies ($V_{cation}$) and antisites ($A_B$ = A replaces B) have formation energies > 2 eV. The presence of $V_O$ in the sample removes the degeneracy of lowermost conduction bands of the pristine α-$SnWO_4$ (see Figure 3 in Appendix A),

splitting those into two separated bands- unoccupied and occupied. The occupied band behaves as donor level, giving rise to the observed n-type activity in α-$SnWO_4$. Despite the fact that cationic vacancies are least probable in single-phase growth conditions, the presence of $Sn_W$ in α – $SnWO_4$ has been reported,[151] and that defect was attributed to the origin of $Sn^{4+}$ in the sample. In Figure 4.3, $Sn_W$ becomes favorable while pairing with $V_O$. To avoid/minimize the formation of that defect as a single/composite formation, one has to select relatively poor and rich growth conditions of Sn and W, respectively in the single-phase growth zone. Such a growth conditions would be along AB and most preferably, on the periphery of point A in Figure 4.3.

#### 4.2.2.4 Conclusion

In conclusion, the promises of α-$SnWO_4$ can be extended if it can be grown with less detrimental defects such as $Sn_W$. A suitable growth condition in this regard would be $\Delta\mu_W > \Delta\mu_{Sn}$ and $\Delta\mu_O << 0$ (for example, point A in Figure 4.3). This would ensure the presence of least $Sn_W$ in the synthesized α-$SnWO_4$ samples and hence the better exhibition of photocatalytic activity.

## 4.3. Quaternary Compound: $Cu_2ZnSnS_4$ (CZTS)

### *4.3.1. Introduction*

Kesterite-$Cu_2ZnSnS_4$ (CZTS) satisfies most of the major criteria for an ideal photovoltaic (PV) material,[153,154] however, its solar to electricity conversion efficiency is not very high; to date, the maximum conversion efficiency of CZTS based solar cell has been reported to be 10.1%,[155,156] ( and 12.6% for CZTSSe[157]) which is far from the theoretical limit (~31%) for a single-junction PV cell.[158] The lower conversion efficiency in CZTS is primarily due to frequent detrimental non-stoichiometric_crystal structure during

synthesis process.[159–161] As in any other multi-cations oxides or sulfides, the frequent non-stoichiometry of CZTS can be attributed to the presence of various defects (such as vacancies, interstitial, antisites etc.) and the co-existences of different secondary phases.[153,162,163] These defects and secondary phases influence the generation, separation, and recombination of electron-hole pairs and overall, the solar-to-current conversion efficiency.[153,164]

In the last ten years, incremental improvements in conversion efficiency of CZTS through different growth techniques have been reported.[155,156,161,165] Nevertheless, satisfactory solar-to-current conversion efficiency as well as synthesis of stoichiometric CZTS has not been reported yet. Further improvement of CZTS as light absorber materials requires: (i) to determine proper growth condition under which the synthesis of CZTS, stoichiometric or non-stoichiometric, with higher light conversion efficiency is possible and (ii) to address the stability issues of CZTS under such growth condition. Theoretical investigations such as electronic structure calculation of defects or defect clusters, and chemical potential landscape analysis can help to address these challenges. For example, it has been reported that Zn-rich and Cu-poor conditions are the most effective growth conditions to synthesize CZTS with higher solar conversion efficiency.[165–172] Recent theoretical calculation[162] validates these experimental findings by performing an extensive intrinsic defect and defect clusters analysis of CZTS. However, to determine an effective growth condition to avoid unwanted secondary phases in CZTS, a comprehensive chemical potential landscape analysis is needed. A detailed thermodynamic investigation of chemical potential landscape in conjunction with defect calculations can provide information regarding the coexistence of secondary phases and intrinsic defects formations, as well as the underlying correlation between them. These pieces of information are necessary to guide the synthesis of CZTS as a better light

absorbing material. A theoretical investigation not only can predict the materials' formation and stability, but also provide information on suitable pathways and growth conditions.

In the present work, mainly, two issues of CZTS have been addressed. First, the non-stoichiometry ($Cu_{2\pm x}$ $Zn_{1\pm y}$ $Sn_{1\pm z}$ $S_{4\pm\varepsilon}$) due to intrinsic lattice defects such as cationic and anionic vacancies ($V_{cation}$, $V_{anion}$, and $V_{cation}+V_{anion}$), cationic antisites ($A_B$, $B_A$, and $A_B$ + $B_A$ ; where, $A_B \rightarrow$ cation A replaces cation B ), cationic antisite - vacancy pairs ($A_B + V_{anion}$, $B_A + V_{anion}$, $A_B + V_A$, $B_A + V_B$ and $A_B + B_A + V_{anion}$). Second, the influence of intrinsic defects on the formation of single-phase CZTS at various growth conditions. We have found through chemical potential (Gibbs free energy) landscape analysis that CZTS, at thermodynamic equilibrium, with an intrinsic defect always coexists with at least one sulfide phase; implying that the single-phase formation is unlikely under such conditions.

*4.3.2. Computational Details*

Acknowledging the fact that the correction to DFT calculations for systems with localized $d$ and $f$ electrons.[58–60] is needed, we have employed $U_{eff}$ = 6 eV, ($U_{eff}$ = U-J=7-1= 6 eV, J = Stoner exchange parameter) both Cu 3d and Zn 3d orbitals. This value of $U_{eff}$ we have chosen here to be consistent with our previous work.[12] Despite the fact that Cu in CZTS has filled 3d shell, we have used U to this element in this study, and the reasons are given below.

It is expected that, like any other Cu $3d^{10}$ compounds, CZTS should have negligible Cu 3d contributions in the conduction band, revealing its filled shell character in the composition. DFT-GGA, as in figure 4.4, reproduces such Cu 3d contributions near the conduction band minimum quite well; those contributions, however, get even smaller with the treatment of U and HSE06-hybrid[133] ( with 25% exact exchange) functional,

depicting $3d^{10}$ natures more accurately in CZTS. Similar Cu 3d contributions around the conduction band edge (see inset in Figure 4.4) in three different methods demonstrate

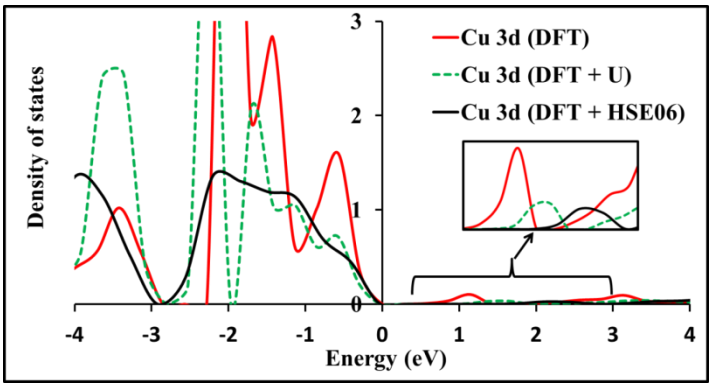


Figure 4.4 Partial density of states of Cu 3d in CZTS with (green broken line; K-mesh: 15x15x9) and without U (red solid line; K-mesh:15x15x9), and HSE06-hybrid (black line; K-mesh: 5x5x3). Due high computational demand, hybrid-DFT calculation was performed with less number of K-points, hence some features of DOS at the valence band are under-estimated; however, the small contribution of Cu 3d empty band at the conduction band minimum is still visible. The extra correlation (exchange) added through U (HSE06-hybrid) lowers the contribution of Cu 3d in the bottom part of the conduction band that manifests the filled shell nature of Cu 3d band better than DFT-only calculations. Inset shows the magnified version of Cu 3d contributions at the bottom of the conduction band in three different methods.

that those contributions are not merely computational artifacts, rather attribute to the limitations of parameterization of XC energy in three different methods. The different positions of the 3d peak at the conduction band are due to the different values of band gaps predicted by these three methods. Being post-DFT methods, both DFT-HSE06 and DFT+U improved band gaps by an amount 0.989 eV and 0.498 eV over DFT counterpart, respectively, whereas DFT-GGA gap was found to be 0.089eV. Although HSE06- hybrid

exhibits better improvement in CZTS band gap, fails to produce accurate description of the valence and conduction contributions to the band-edge corrections, demonstrating defect levels at wrong position in the corrected band gap.[173] In contrast, DFT+U, despite the underestimation of band gap, produces more accurate description of band-edge shifts, as does *scGW*, however, would require a significant less computational cost. Apart from our calculation as shown in Figure 4.4, with the addition of U comprised compound named γ-CuI has been reported in reference.[174]Moreover, it is canonical parameter, the improvement of both band gap and defect formation energy in another Cu $3d^{10}$ to treat all the Cu 3d orbitals, both in CZTS and all Cu based secondary phases, on equal footing. For some of the secondary phases discussed in this paper DFT+U is necessary. For instance, Cu 3d has unfilled nature in $Cu_2S$, and DFT not only underestimates the band gap but also determines wrong solid state description of that material.[175] DFT+U, however, improves band gap by 0.689 eV and produces correct semiconductor solution of that secondary phase as well. For these reasons, we have used U to Cu 3d in $Cu_2S$ and kept all Cu 3d orbitals in different compounds under the same treatment. Like in $Cu_2S$, DFT+U was also used to correct the band gap error in ZnS[176] and ZnO,[177,178] which motived us to employ the similar U contribution to Zn 3d. In the present work, the DFT+U formation energies of secondary phases (and CZTS) are consistent to HSE06-hybrid calculation,[179]and show even better agreement with the experimental counterparts.[180] A 2×2×1 supercell (64 atoms) was employed for the defect calculations with a k-point sampling of 5×5×5.

*4.3.3 Single-phase stability of CZTS*

To determine the single-phase stability of CZTS, we have considered all probable secondary sulfide phases formed by Cu, Zn, and Sn cations, which can co-exist

with it at any growth environment. The probable secondary phases are: three possible binary compounds of Sn-S (SnS, $SnS_2$, and $Sn_2S_3$), two possible binary compounds of Cu-S (CuS and $Cu_2S$), one possible binary compound of Zn-S (ZnS), and one ternary compound of Cu-Sn-S ($Cu_2SnS_3$).

In equilibrium growth condition of CZTS, to avoid the occurrences of these secondary phases according to Eq. (2.87) following conditions have to be satisfied:

$Cu_2S$: $2\Delta\mu_{Cu} + \Delta\mu_S < \Delta H_{f,Cu_2S} = -0.81$ eV, 4.5

CuS : $\Delta\mu_{Cu} + \Delta\mu_S < \Delta H_{f,CuS} = -0.51$ eV, 4.6

ZnS: $\Delta\mu_{Zn} + \Delta\mu_S < \Delta H_{f,ZnS} = -1.90$ eV, 4.7

SnS: $\Delta\mu_{Sn} + \Delta\mu_S < \Delta H_{f,SnS} = -1.05$ eV, 4.8

$SnS_2$: $\Delta\mu_{Sn} + 2\Delta\mu_S < \Delta H_{f,SnS_2} = -1.33$ eV, 4.9

$Sn_2S_3$: $2\Delta\mu_{Sn} + 3\Delta\mu_S < \Delta H_{f,Sn_2S_3} = -2.42$ eV, 4.10

$Cu_2SnS_3$: $2\Delta\mu_{Cu} + \Delta\mu_{Sn} + 3\Delta\mu_S < \Delta H_{f,Cu_2SnS_3} = -2.58$ eV. 4.11

In equilibrium, the necessary thermodynamics condition (see Eq. (2.86)) to form a stable stoichiometric $Cu_2ZnSnS_4$ (CZTS) is

CZTS: $2\Delta\mu_{Cu} + \Delta\mu_{Sn} + \Delta\mu_{Zn} + 4\Delta\mu_S = \Delta H_{f,CZTS} = -4.59$ eV 4.12

The upper and lower bounds of chemical potentials satisfying equation (2.89) for each atomic species according to Eq. (2.84) are

$-2.294$ eV $\leq \Delta\mu_{Cu} \leq 0$ eV, (4.13a)

$-4.59$ eV $\leq \Delta\mu_{Zn} \leq 0$ eV, (4.13b)

$-4.59$ eV$\leq \Delta\mu_{Sn} \leq 0$ eV, (4.13c)

$-1.15$ eV $\leq \Delta\mu_S \leq 0$. (4.13d)

Figure 4.5 shows the chemical potential landscapes of stoichiometric CZTS which are bounded by Eq. (2.89). These stability triangles for CZTS were drawn following

the approach explained in reference.[160] Each triangle represents a plane cut at different values for $\Delta\mu_{Cu}$; the abscissa, height, and diagonal of each triangle are bounded by $\Delta H_{f,CZTS}/n_{\alpha}$ (α = Zn, Sn, and S), respectively. Each point in these triangles satisfies equation (4.12) implying the formation of CZTS is possible anywhere inside and on these triangles.

Each line, $L_i$ (i = 1, 2, .., 7), on the chemical potential triangles shown in figures 4.5, 4.7, and 4.8 represents a boundary of a secondary phase that may coexist during the synthesis process of CZTS depending on the growth condition. Therefore, any point on each line, which divides the triangles into two regions, equals to corresponding $\Delta H_{f,s}$ (see equations (2.87) and (4.5-4.11)). The co-existence of a secondary phase is evident in any region which does not satisfy any of equations (4.5-4.11). For example, if we cross the triangle parallel to the diagonal (constant $\Delta\mu_S$) to the left from any point on the red ($Cu_2SnS_3$) line or $L_7$ (which holds equation (4.11) everywhere on it), $\Delta\mu_{Sn}$ will have higher value with respect to that point; similar statement is true for $\Delta\mu_S$ if we move horizontally (fixed $\Delta\mu_{Sn}$) towards left with respect to any point belonging to that line ($L_7$). As a result, any point that belongs to the region on the left of the red line does not satisfy equation (4.11) and hence, co-existence of $Cu_2SnS_3$ with CZTS is possible over that region. On the contrary, the co-existence of ZnS is possible on the region that corresponds to the right of green (ZnS) line or $L_3$ since equation (4.7) is not satisfied in that region (see Figure 4.5). All the Sn-S secondary phases are evident on the regions above lines (L4 - L6) representing those phases since equations 4.8-4.10 are not held over those regions. Conversely, the regions below the lines (L1- L2) representing Cu-S secondary phases do not satisfy equations 4.5-4.6 and therefore, these phases are always likely to occur there. As a result, although the formation of CZTS is possible everywhere inside the triangle, not a single bounded region at Cu-rich ($\Delta\mu_{Cu}$= 0) condition was found (see Figure 4.5a),

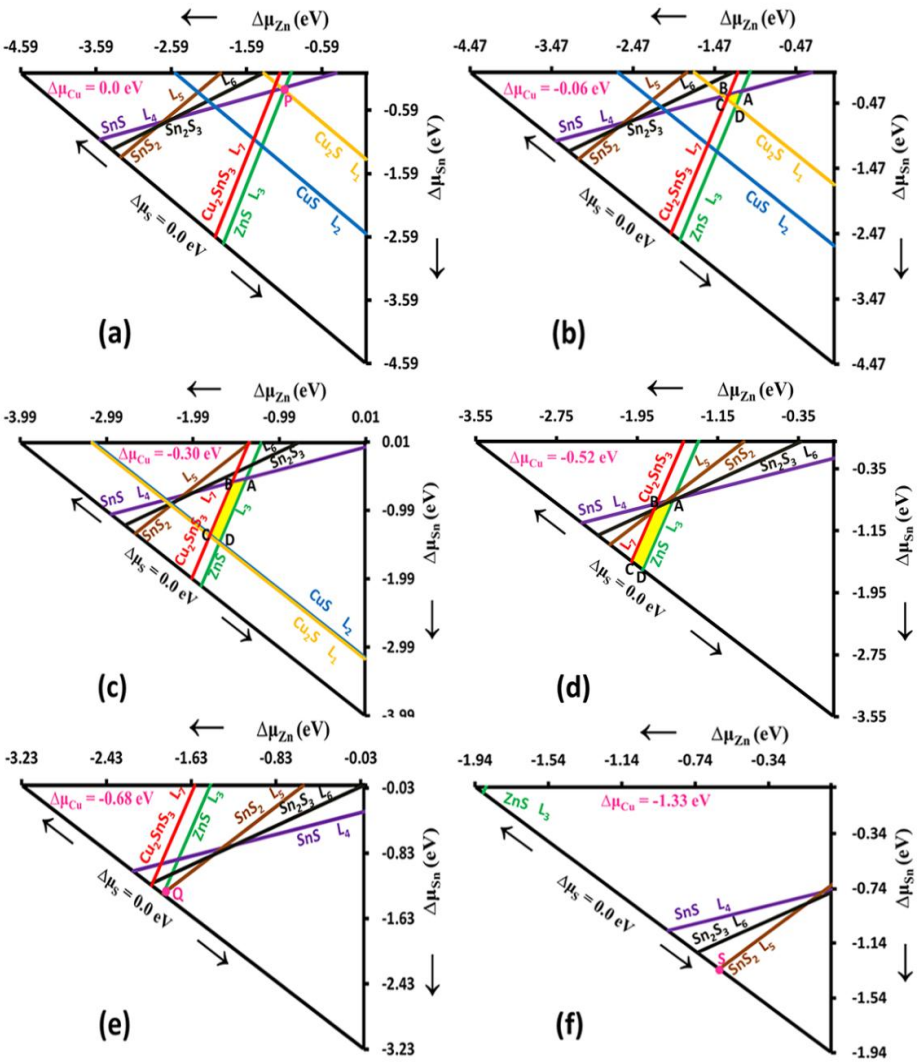


Figure 4.5 The triangles represent chemical potential landscapes for $Cu_2ZnSnS_4$ drawn at different Cu chemical potentials, $\Delta\mu_{Cu}$. Point P (figure (a)) and point Q (figure (d)), correspond to starting and end point growth conditions, respectively for stoichiometric $Cu_2ZnSnS_4$. Point S (figure (f)) corresponds to minimum $\Delta\mu_{Cu}$ at which $V_{Cu}$ becomes spontaneous.

except point P corresponds to a single-phase CZTS formation. Any little change of $\Delta\mu_\alpha$ ($\alpha$ = Zn, Sn, and S) at $\Delta\mu_{Cu}$= 0 with respect to point P will cause CZTS to co-exist with secondary phases; no other suitable growth conditions ($\Delta\mu_\alpha$, $\alpha$ = Zn, Sn, and S) at Cu-rich environment facilitate the single-phase formation of CZTS.

As $\Delta\mu_{Cu}$ becomes poorer ($\Delta\mu_{Cu} < 0$), point P emerges as a region (see yellow regions *ABCD* in Figure 4.5b-d). Any point belonging to area *ABCD* represents the necessary growth condition at which the formation of a single-phase CZTS, stoichiometric or non-stoichiometric ($Cu_{2\pm x}\ Zn_{1\pm y}\ Sn_{1\pm z}\ S_{4\pm\varepsilon}$), is possible. In the following subsection probability of defects formation will be examined in this single-phase region. The areas of *ABCD* regions in Figures 4.5b-d are not fixed, rather change with poorer $\Delta\mu_{Cu}$, and eventually vanish, converging into point Q in Figure 4.5e with $\Delta\mu_{Cu}$ = -0.68 eV. Any lower value beyond $\Delta\mu_{Cu}$ = -0.68 eV corresponds to the growth condition at which the formation of single-phase CZTS is no longer possible irrespective of $\Delta\mu_\alpha$ ($\alpha$ = Zn, Sn, and S) values. Therefore, only 0 eV < $\Delta\mu_{Cu}$ < -0.68 eV corresponds to suitable Cu-poor range for the synthesis of single-phase CZTS. In addition to that $\Delta\mu_{Cu}$ limit, further Cu poor ($\Delta\mu_{Cu}$ = -1.33 eV) growth condition was considered to draw Figure 4.5f, intending for defect formation discussion in the following section. This Cu poorer condition corresponds to threshold of spontaneous formation of Cu vacancy ($V_{Cu}$) which is considered to be a major beneficial defect[160,162] to CZTS solar performance,

It is noted that the lines representing $Cu_2S$ or CuS phases are no longer seen in Figure 4.5d at $\Delta\mu_{Cu}$ = -0.52 eV. The disappearance of these lines infers the fact that the formation of those phases is no longer possible at $\Delta\mu_{Cu} \leq$ -0.52 eV, the proof of which can be made using equations 4.5-4.11 and 4.12. For instance, the available chemical potential of S (-0.89 eV $\leq \Delta\mu_S \leq$ 0 eV) according to equation 4.12 at $\Delta\mu_{Cu}$ = -0.52 eV can not provide CuS with necessary growth conditions to attain the value, $\Delta H_{f,CuS}$ = -0.51 eV.

As a result, the formation of CuS ($L_2$) is impossible even at $\Delta\mu_S$ =0 (S-rich) since there will not be enough Cu to form this secondary phase. The similar explanation is also applicable for $Cu_2S$-line ($L_1$) line disappearance at $\Delta\mu_{Cu}$ = -0.41 eV (not shown in the figure).

*4.3.4. Defects formation*

Defects formation energies in CZTS and their ionization energies pursuing DFT and post-DFT (HSE06-hybrid) methods have been discussed at length in references.[160,162,179] However, for the completeness and consistency of the present discussions, here, we briefly present our defects formation calculations, which are consistent to results reported in those aforementioned references in the single-phase limit. Figure 4.6 represents the formation energies of various intrinsic defects. Our

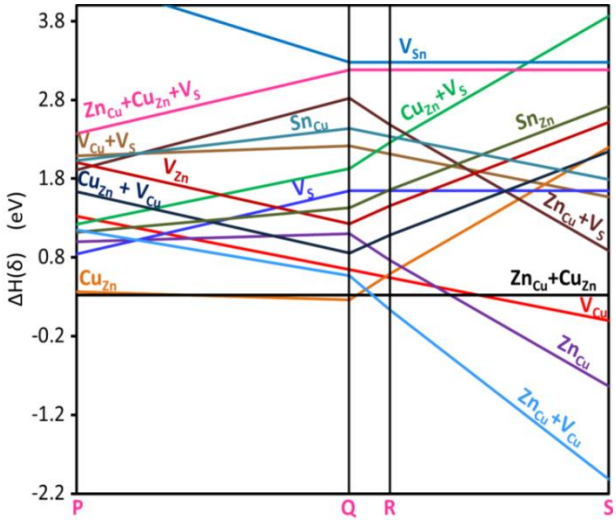


Figure 4.6 Various defect formation energies are shown. Point P, point Q, and point S correspond to three sets of $\Delta\mu_\alpha$ values in Figures 4.5a, 4.5d, and 4.5f, respectively. Point R is not shown in figure 4.5, chosen at $\Delta\mu_{Cu}$ = -0.78 eV. See table 4.2 for the values of $\Delta\mu_\alpha$ at P, Q, R, and S.

calculation is mainly focused on three types of defects: (i) dominant cationic defects those are mentioned in the recent literature at different growth conditions, (ii) the anionic defect ($V_S$), which were found to be most detrimental to CZTS solar performance,[160,162] and (iii) those defects in (i) with the presence of $V_S$ defect. In general, all the cationic defects with the presence of anionic defects were found to have higher formation energies as compared to the formation energies while forming independently. The defects in (iii) which have very high formation energies (> 4 eV) were not presented in Figure 4.6.

Table 4.2 The values of chemical potentials for cations, $\Delta\mu_\alpha$ ($\alpha$ = Cu, Zn, Sn, and S), at points P, Q, R, and S with respect to figure 4.5.

| Figure | Chemical Potential | | Points | | | |
|---|---|---|---|---|---|---|
| | $\Delta\mu_{Cu}$ eV | $\Delta\mu_\alpha$ | P eV | Q eV | R eV | S |
| 4.5a | 0.0 | $\Delta\mu_{Zn}$ | -1.12 | - | | |
| | | $\Delta\mu_{Sn}$ | -0.24 | - | | |
| | | $\Delta\mu_S$ | -0.81 | - | | |
| 4.5e | -0.68 | $\Delta\mu_{Zn}$ | - | -1.89 | | |
| | | $\Delta\mu_{Sn}$ | - | -1.33 | | |
| | | $\Delta\mu_S$ | - | 0.0 | | |
| Not Shown | -0.78 | $\Delta\mu_{Zn}$ | - | - | -1.67 | |
| | | $\Delta\mu_{Sn}$ | - | - | -1.33 | |
| | | $\Delta\mu_S$ | - | - | 0.0 | |
| 4.5f | -1.325 | $\Delta\mu_{Zn}$ | - | - | | -0.61 |
| | | $\Delta\mu_{Sn}$ | - | - | | -1.33 |
| | | $\Delta\mu_S$ | - | - | | 0.0 |

Four different points *P*, *Q*, *R*, and *S* in Figure 4.6 are chosen at different $\Delta\mu_{Cu}$ values: point *P* corresponds to Cu-rich and S-poor conditions while other points correspond to Cu-poor and S-rich condition; points *R* and *S* are chosen at $\Delta\mu_S = 0$ to see whether S-rich can avoid the detrimental $V_S$ defect while non-stoichiometry of CZTS is

evident beyond point *Q*. Moreover, point *R* corresponds to the least value of $\Delta\mu_{Zn}$ for which $V_{Cu}$ dominates over $Cu_{Zn}$ antisite defects, both were found to be beneficial for p-type activity,[160,162] at Cu-poor ($\Delta\mu_{Cu}$ = -0.78 eV) condition. On the other hand, point *S*, which corresponds to spontaneous formation of $V_{Cu}$, mimics the attributes of point K in Figure 4.8b at $\Delta\mu_{Cu}$ = -1.33 eV. The values of $\Delta\mu_{\alpha}$ (α = Cu, Zn, Sn, and S) at points P, Q, R, and S shown in Figures 4.5a, 4.5e, and 4.5f, respectively, are presented in Table 4.2.

In Figure 4.6, $Zn_{Cu}$ + $Cu_{Zn}$ antisite (both Cu and Zn replace each other) defect has the lowest formation energy between points *P* and *Q*, which is constant irrespective of Cu-value. Since $Zn_{Cu}$ + $Cu_{Zn}$ antisite pair preserves the number of atoms of both Zn and Cu species, stoichiometry of CZTS due to a defect remains unaffected by this antisite pair. However, the antisite $Cu_{Zn}$, which can cause non-stoichiometry in CZTS, has very low formation energy ($\Delta H(Cu_{Zn})$ = 0.37 eV ) and is almost equally probable as composite antisite of $Zn_{Cu}$ + $Cu_{Zn}$ at $\Delta\mu_{Cu}$ = 0.0 eV (at point *P*). Moreover, compared to other defects, $\Delta H(Cu_{Zn})$ becomes slightly lower between points *P* and *Q* (see Figure 4.6) which implies that the presence of $Cu_{Zn}$ intrinsic defect is likely to occur for the growth conditions available in *ABCD* regions. This entails that *ABCD* regions correspond to only non-stoichiometric single-phase CZTS ($Cu_{2\pm x}\ Zn_{1\pm y}\ Sn_{1\pm z}\ S_{4\pm\varepsilon}$). However, $\Delta H(Cu_{Zn})$ starts increasing significantly after point *Q* and becomes higher than $\Delta H(V_{Cu})$ at *R*. On the contrary, $\Delta H(V_{Cu})$, having a higher value at *P*, becomes lower as $\Delta\mu_{Cu}$ decreases and reaches a negative value (-0.001 eV) at *S*. Another defect $Zn_{Cu}$ , which has higher formation energy between *P* and *Q*, becomes more and more probable after *Q*. Similar trend was observed for $Zn_{Cu}$+$V_{Cu}$ which attained the lowest formation energy at *S* in Figure 4.6. Among all detrimental defects, only $V_S$ has lowest formation energy ($\Delta H(V_S)$ = 0.84 eV) at Cu-rich condition and S-poorer condition; $\Delta H$ ($V_S$) increases as Cu-becomes poorer at S-rich condition. Hence, it is necessary to provide S-rich condition to avoid $V_S$

defects in CZTS. From Figure 4.6 it can be concluded that intrinsic defects are almost inherent in CZTS at any value of $\Delta\mu_{Cu}$. Hence, it is needed to investigate the chemical potential landscape of CZTS allowing intrinsic defects to be formed at different $\Delta\mu_{Cu}$, which will be presented in the following subsection.

*4.3.5. Role of intrinsic defects on single-phase stability of CZTS*

It is clear from Figure 4.6 that even if the synthesis of single-phase CZTS is possible, stoichiometry is unlikely. Moreover, the reported[166–172] synthesis of CZTS are indeed non-stoichiometric. Hence, it has been imperative to analyze the stability and growth condition of non-stoichiometric CZTS as well for high efficiency solar light absorption and conversion. Two attributes can lead to non-stoichiometry of CZTS: (i) defect or defect clusters and (ii) co-existence of secondary phases. So, the important question here, what is the probability of achieving single-phase CZTS where non-stoichiometry is only due to defects? This question will be answered in the following discussions. To facilitate the discussions, when only defect causing non-stoichiometry takes place we term it here as *single-phase non-stoichiometric* CZTS. On the other hand, the term *multi-phases non-stoichiometric* CZTS will be used when both defects and secondary phases co-exists.

It is shown in Figure 4.6 that two dominant beneficial defects, Cu-Zn antisite ($Cu_{Zn}$) and Cu vacancy ($V_{Cu}$) at Cu-rich (point P in Figure 4.6) and Cu-poor (point S in Figure 4.6) conditions, respectively, have very low formation energies. On the contrary, all detrimental defects have relatively higher formation energies at any values of $\Delta\mu_{Cu}$. Hence, for brevity only $V_{Cu}$ and $Cu_{Zn}$ causing non-stoichiometric CZTS will be considered for the present discussion.

In the following discussion, $\Delta H_{CZTS}$ in equations 4.15 and 4.17 were calculated following the equation (4) and have the form:

CZTS(δ): $\Delta H_{CZTS} = E_{CZTS,supercell}(\delta) - k_\alpha \sum_\alpha E_\alpha^{bulk}$. (4.14)

where $E_{supercell}$ (δ) corresponds to the energy of a CZTS-supercell that contains a single defect δ (= $Cu_{Zn}$ or $V_{Cu}$). $k_\alpha$ is the number of atoms of species α present in the supercell and $E_\alpha^{bulk}$ bears the same definition as in equation (2.85). Following this, the necessary thermodynamic conditions to form these two types of non-stoichiometric CZTS are:

(i) $Cu_{Zn}$: $\Delta\mu_{Cu} + \Delta\mu_{Sn} + \Delta\mu_{Zn} + 4\Delta\mu_S = \Delta H_{CZTS}$ = -4.40 eV. (4.15)

where,

-2.20 eV ≤ $\Delta\mu_{Cu}$ ≤ 0 eV, (4.16a)

-4.40 eV ≤ $\Delta\mu_{Zn}$ ≤ 0 eV, (4.16b)

-4.40 eV≤ $\Delta\mu_{Sn}$ ≤ 0 eV, (4.16c)

-1.10 eV ≤ $\Delta\mu_S$ ≤ 0. (4.16d)

and

(ii) $V_{Cu}$: $2\Delta\mu_{Cu} + \Delta\mu_{Sn} + \Delta\mu_{Zn} + 4\Delta\mu_S = \Delta H_{CZTS}$ = -4.42 eV. (4.17)

where,

-2.21 eV ≤ $\Delta\mu_{Cu}$ ≤ 0 eV, (4.18a)

-4.42 eV ≤ $\Delta\mu_{Zn}$ ≤ 0 eV, (4.18b)

-4.42 eV≤ $\Delta\mu_{Sn}$ ≤ 0 eV, (4.18c)

-1.11 eV ≤ $\Delta\mu_S$ ≤ 0. (4.18d)

The chemical landscapes of non-stoichiometric CZTS caused by $Cu_{Zn}$ and $V_{Cu}$ at different $\Delta\mu_{Cu}$ are presented in Figures 4.7 and 4.8, respectively. In these figures, $Cu_2S$-line ($L_1$) and ZnS-line ($L_3$) changed their positions with respect to Figure 4.5 leaving no

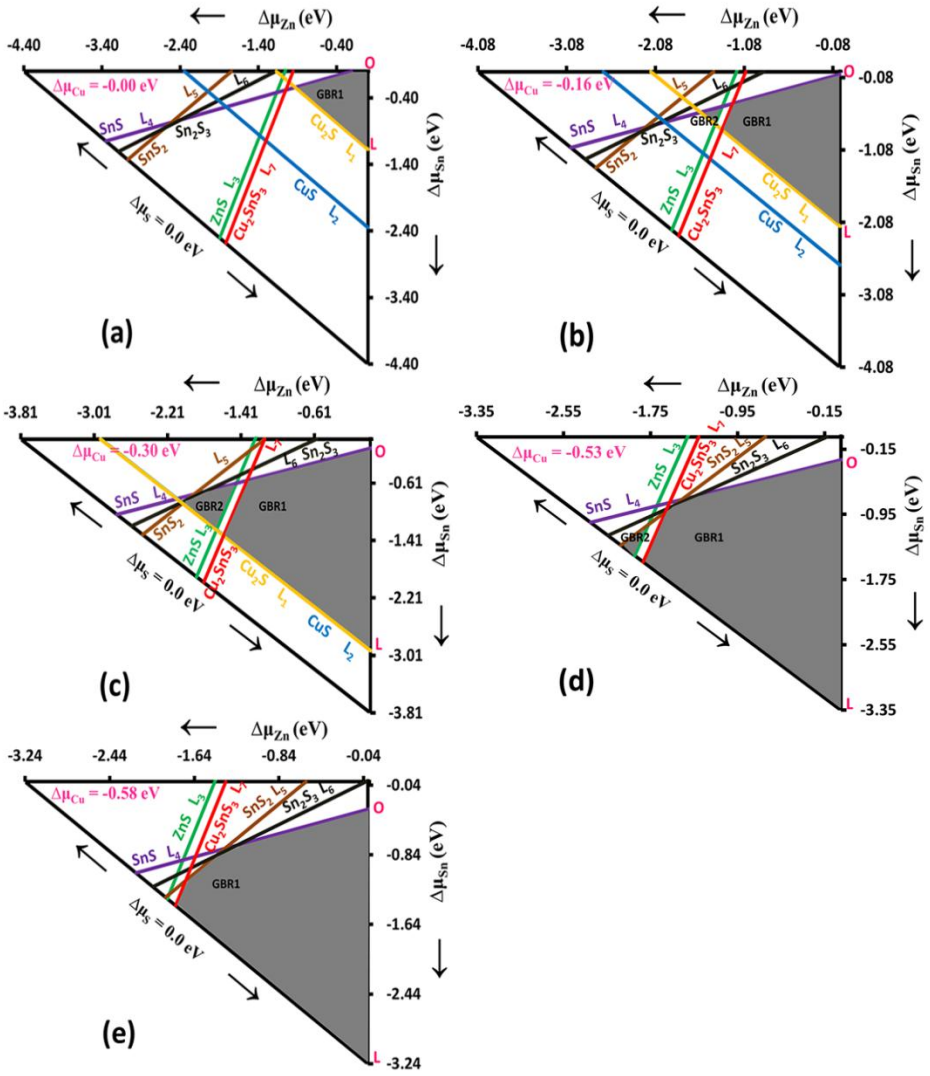


Figure 4.7Chemical potential landscapes of non-stoichiometric $Cu_2ZnSnS_4$ that contain one $Cu_{Zn}$ defect per supercell (64 atoms). Grey bounded regions (GBR1 and GBR2) in the figures represent the occurrence of one secondary phase (ZnS or $Cu_2SnS_3$) along with $Cu_2ZnSnS_4$.

bounded region where equations 4.5-4.11 are simultaneously satisfied. This implies that a single defect prohibits the formation of single-phase CZTS under these conditions and triggers the formation of multi-phases non-stoichiometric CZTS; at least one secondary phase co-exists with it. This finding was observed at irrespective of DFT or DFT+U level, which implies that the formation of multi-phases non-stoichiometric CZTS is independent of empirical treatment of Coulomb correlations through U. Since intrinsic defects are very likely to form at any value of $\Delta\mu_{Cu}$ irrespective of U value (see reference[80] for $\Delta H$ ($\delta$) at DFT level ), this justifies why secondary phases are frequently found experimentally to be co-existed with CZTS. Therefore, it can be concluded that the synthesis of single-phase stoichiometric CZTS would be unlikely *at thermodynamic equilibrium condition*.

To the best of our knowledge, we find only one experimental evidence of single-phase CZTS grown in traveling heater method (THM).[181] This work, although, confirms the non-existence of $SnS_x$ and Sn phases with CZTS, information regarding the co/non-existence of two other phases ZnS and $Cu_2SnS_3$ were absent. ZnS and $Cu_2SnS_3$, because of same zincblende framework as CZTS,[182] are hard to be detected through only XRD analysis;[162] alternative techniques such as energy dispersive X-ray spectroscopy (EDS),[183] Raman scattering analysis,[184,185] and X-ray absorption near edge structure analysis[187] are needed to be employed. ZnS sometimes coexists even in the CZTS samples with the stoichiometric Zn/Sn ratio.[187] This implies that our aforementioned conclusion is more pertinent than the claim in reference.[181]

### *4.3.6. High efficient CZTS*

#### 4.3.6.1 Determination of an effective growth condition

While the non-stoichiometry of a desired material is evident, it is then necessary to explore effective growth condition at which (i) the co-existence of secondary phases is

minimal, (ii) the benign/beneficial defects are dominant, and (iii) the contributions from detrimental defects will be absent or negligible. An optimal growth condition should satisfy these conditions.

The grey bounded regions in Figures 4.7 and 4.8 represent the formation of multi-phases non-stoichiometric CZTS where only one secondary phase, either ZnS or $Cu_2SnS_3$, co-exists; ZnS-CZTS and $Cu_2SnS_3$-CZTS belong to GBR1 (Grey Bounded Region 1) and GBR2 (Grey Bounded Region 2), respectively. All other regions represent the co-existence of more than one secondary phase and most importantly, Sn-S and Cu-S phases. These phases have different crystal structures (either orthorhombic or monoclinic or trigonal) than that of CZTS causing a lattice mismatch at the interface. It was reported that that incoherent heterointerfaces, failing to passivate grain boundaries, empower the electron-hole recombination process and consequently reduce the solar-to-current conversion efficiency.[164] Therefore, no region except GBR (1 or 2) does correspond to high efficiency growth conditions for CZTS. Hence, our non-stoichiometric analysis will be limited to these grey bounded regions only.

Although each grey region corresponds to coexistence of one secondary phase with CZTS, may not contribute to solar – to – current conversion equally. The grey region with lower probability of forming detrimental (e.g. $V_S$, $Sn_{Cu}$, $Sn_{Zn}$ etc.) defects and higher probability of beneficial ($V_{Cu}$ and $Cu_{Zn}$) or benign defects (e.g. $Cu_{Zn}$+$Zn_{Cu}$, $Zn_{Cu}$+ $V_{Cu}$ etc.) corresponds to high efficiency growth condition for CZTS. To minimize the formation of $V_S$, $Sn_{Cu}$ and $Sn_{Zn}$ defects it is necessary to have sufficiently S-rich, Zn-rich, and Sn-poor conditions. It was shown in Figure 4.6 that beneficial $Cu_{Zn}$ defects are probable when sufficient Cu-rich and Zn-poor growth conditions are available. Conversely, Cu-poor condition is necessary to promote more $V_{Cu}$ defects which are primarily responsible for high efficiency of CZTS.[162] In the following, all the grey regions will be examined one by

one to see which one satisfies most these high efficiency growth conditions simultaneously.

In Figure 4.7a at Cu-rich condition, only one grey region (GBR1) is formed where ZnS coexists with CZTS (ZnS-CZTS). Although GBR1 has larger area i.e., better flexibility of tuning $\Delta\mu_\alpha$ ($\alpha$ = Zn, Sn, and S) values, does not correspond to high efficiency growth conditions due to two reasons. First, point *O*, which represents the lower bound value of $\Delta\mu_S$ for GBR1, corresponds to extreme S-poor condition. On other hand, point *L*, representing the upper bound value of $\Delta\mu_S$ (= -0.81 eV) for GBR1, still corresponds to same S-poor condition as at point *P* in Figure 4.5 a. $\Delta H$ ($V_S$) was found to have lower value (0.84 eV) in Figure 4.6 under such S-poor ($\Delta\mu_S$ = -0.81 eV) condition, suggesting higher probability of forming detrimental $V_S$ defects. These defects may create a significant number of deep donor levels,[162] and these donor levels may act as electron-hole recombination centers which are detrimental to any semiconductor's performance. Second, the most beneficial defect $V_{Cu}$ towards enhanced p-type activity of CZTS is very unlikely for GBR1 in Figure 4.7a since it has higher formation energy ($\Delta H$ ($V_{Cu}$) = 1.32 eV) at Cu-rich condition; further decrement of $\Delta\mu_{Cu}$ is necessary to have higher contributions from $V_{Cu}$ defects. At $\Delta\mu_{Cu}$ = -0.16 eV both GBR1 and GBR2 appear on the plane but area of GBR2 is much smaller than that of GBR1 (see Figure 4.7b). The smaller area of GBR2 implies that the synthesis of $Cu_2SnS_3$-CZTS would be very challenging; any small deviation of $\Delta\mu_\alpha$ ($\alpha$ = Zn, Sn, and S) would bring in more secondary phases. On the contrary, the synthesis of ZnS-CZTS would be easier if the growth condition in GBR1 is pursued.

Nonetheless, $Cu_2SnS_3$-CZTS mixed phase corresponds to a better efficiency growth condition over ZnS-CZTS at $\Delta\mu_{Cu} \geq$ -0.16 eV. This can be attributed to the fact that any point belonging to GBR2 has lower $\Delta\mu_{Zn}$ value than that of to GBR1, and beneficial

$Cu_{Zn}$ defect is more probable at $\Delta\mu_{Zn}$ poor values if $\Delta\mu_{Cu}$ remains same. Moreover, the contributions from $V_{Cu}$ defects at $\Delta\mu_{Cu}$ = -0.16 eV, if formed, would be equal for each region since both lies on the same $\Delta\mu_{Cu}$ plane. In addition, contributions from detrimental $V_S$ defects in GBR2 would be equal or less than that of in GBR1 since the upper bound value of $\Delta\mu_S$ (see point *L* in Figure 4.7) is same for both regions while lower bound value of $\Delta\mu_S$ is significantly higher in GBR2 than that of in GBR1. In contrast, relatively much lower $\Delta\mu_{Sn}$ values are possible in GBR1 compared to GBR2, and it is beneficial since Sn-poorer condition is desirable to avoid the formation of detrimental $Sn_{Zn}$ and $Sn_{Cu}$ defects. Hence, GBR1 will have less probability of forming those detrimental defects in comparison with GBR2 if Sn-poorer conditions are chosen; however, presence of those detrimental defects in GBR2 are very unlikely as well since they have very high formation energy even at Sn-rich condition (point *P* in Figure 4.6 which has higher $\Delta\mu_{Sn}$ values than that of in GBR2). Similar comparison between GBR1 and GBR2, can also be made for further Cu-poor condition such as in Figures 4.7c and 4.7d. It is to be noted that the area of GBR2 increases as $\Delta\mu_{Cu}$ decreases, becomes maximum while $Cu_2S$-line ($L_1$) merges with CuS-line ($L_2$) at $\Delta\mu_{Cu}$ = -0.30 eV, starts decreasing at $\Delta\mu_{Cu}$ < -0.30 eV, and eventually, vanishes at $\Delta\mu_{Cu}$ = -0.58 eV. However, GBR2 would not correspond to growth condition of high efficiency solar absorber as points belonging to this area do not facilitate the conditions for $V_{Cu}$ being dominant over $Cu_{Zn}$, which is necessary to extract maximum hole concentration. Hence, $Cu_2SnS_3$-CZTS will not exhibit maximum efficiency due to the lack of enough hole concentration. On other hand, GBR1 (ZnS-CZTS) still exists and occupies maximum area of triangle even at $\Delta\mu_{Cu}$ = -0.58 eV. Therefore, only GBR1 will be investigated at further Cu-poor condition at which CZTS contains $V_{Cu}$ defect.

Figure 4.8 represents chemical potential landscape of $V_{Cu}$ – CZTS where $\Delta\mu_{Cu}$ = −0.78 eV and $\Delta\mu_{Cu}$ = −1.33 eV were chosen in such a way that any point in GBR1

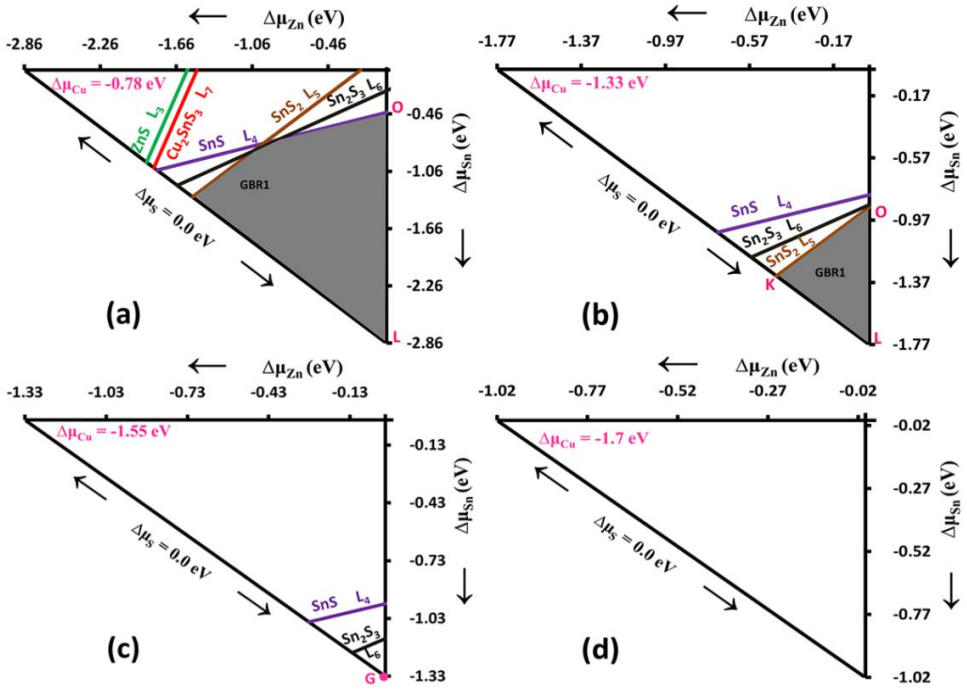


Figure 4.8 Chemical potential landscapes of non-stoichiometric $Cu_2ZnSnS_4$ that contain a $V_{cu}$ defect per supercell (64 atoms). Grey bounded regions (GBR1) in the figures represent the occurrence of one secondary phase (ZnS) along with $Cu_2ZnSnS_4$.

promotes formation of $V_{Cu}$. Since GBR1 at $\Delta\mu_{Cu} = -0.78$ eV shows $V_{Cu}$ dominance, the hole concentration as well as p-type activity of CZTS will be enhanced significantly. Moreover, the larger area of GBR1 at $\Delta\mu_{Cu} = -0.78$ eV provides wider flexibility of tuning up the growth condition. For examples, if Zn-poor values of GBR1 are chosen, the contributions from $Cu_{Zn}$ defects alongside $V_{Cu}$ defects are very likely since they will still have low formation energies (point *R* in Figure 4.6). On the other hand, if $\Delta\mu_{Zn} \rightarrow 0$ values are chosen, $\Delta\mu_{Sn} << 0$ are obtainable which are beneficial to avoid the formation of detrimental $Sn_{Zn}$ and $Sn_{Cu}$ defects. Moreover, S-rich condition for GBR1 is always achievable at $\Delta\mu_{Cu} \leq -0.58$ eV. Hence, far better efficiency is achievable from GBR1 at

$\Delta\mu_{Cu}$ = −0.78 eV if Zn- and Sn-poorer conditions are chosen; the maximum contributions from $V_{Cu}$ defect, however, is yet to come until $\Delta\mu_{Cu}$ = −1.33 eV at which $\Delta H$ ($V_{Cu}$) becomes negative (see point S in Figure 4.6).

In addition to spontaneous formation of $V_{Cu}$, significant Sn-poor values will still be present in GBR1 at $\Delta\mu_{Cu}$ = -1.33 eV. Moreover, like as before, maximum S-rich condition is also achievable in this case. As a result, the presence of detrimental $V_S$ defects would not be more than those as in previous GBR1s (Figures 4.7 and 4.8a). It is to be noted that in GBR1 at $\Delta\mu_{Cu}$ = -1.33 eV, $\Delta\mu_{Zn} \rightarrow$ 0.0 eV as $\Delta\mu_S \rightarrow$ 0.0 eV and $\Delta\mu_{Sn} <<$ 0.0 eV. These growth conditions are required to maintain Cu/(Zn+Sn) <1 and Zn/Sn >1 ratios which reduce detrimental [$2Cu_{Zn} + Sn_{Zn}$] defects and are conducive to have higher hole concentration contributed by $V_{Cu}$ defects.[162] In addition, both $\Delta H(Zn_{Cu})$ and $\Delta H(Zn_{Cu}+V_{Cu})$ were found to have negative values at $\Delta\mu_{Cu}$ = -1.33 eV (see Figure 4.6), even much lower than $\Delta H$ ($V_{Cu}$). $Zn_{Cu}$ defect creates shallow donor levels which do not act as recombination centers and hence, at least, are not detrimental for solar energy conversion efficiency.[162] In contrast, the high population of $Zn_{Cu}+V_{Cu}$ defects result in band bending that favors the separation of electron-hole pairs, which in turn boosts solar-to-current conversion.[160,162,163] However, the contribution from the beneficial $Cu_{Zn}$ defects in GBR1 at $\Delta\mu_{Cu}$ = −1.33 eV would be very minimal since $\Delta H$ ($Cu_{Zn}$) is very high at point *S* (see Figure 4.6). It can be attributed to the fact that Zn becomes richer ($\Delta\mu_{Zn} \geq$ - 0.44 eV, see Figure 4.8b) in GBR1 at $\Delta\mu_{Cu}$ = −1.33 eV compared to point *R* ($\Delta\mu_{Zn}$ = - 1.67 eV) in Figure 4.6, and $\Delta H$ ($Cu_{Zn}$) increases as $\Delta\mu_{Zn}$ increases while $\Delta\mu_{Cu}$ remains same or becomes poorer. Despite the fact that the presence of $Cu_{Zn}$ defect would be less, it can be concluded that GBR1 at $\Delta\mu_{Cu}$ = −1.33 eV is likely to be the preferable growth condition because it does guarantee not only the maximum p-type activity of CZTS through $V_{Cu}$ defect but also promotes the formation of all benign defects and satisfies all

other criteria such Zn-rich, Sn-poor etc. growth conditions simultaneously to avoid detrimental defects. In other words, only ZnS-CZTS can exhibit maximum PV efficiency if suitable growth conditions are chosen during the synthesis. The lower recombination velocity at ZnS-CZTS interface as reported in a recent experimental study[164] strengthens our conclusion as well.

The area of GBR1 becomes smaller at $\Delta\mu_{Cu} < -1.33$ eV which implies that the synthesis of CZTS would be very challenging at further Cu-poor values since GBR1 tends to be a point at $\Delta\mu_{Cu} \rightarrow -1.55$ eV. At $\Delta\mu_{Cu} \leq -1.55$ eV the formation of any grey bounded region is no longer possible. Therefore, $-1.33 \text{ eV} \leq \Delta\mu_{Cu} < -1.55$ eV corresponds to the Cu-poor growth condition for CZTS as high efficiency solar absorber. The boundary values of other chemical potentials, $\Delta\mu_{\alpha}$'s, at this Cu-range are tabulated in Table 4.3. It is important to note that at point *S* (equivalent to point K in Figure 4.8b) shown in Figure 4.6, $\Delta H$ ($Cu_{Zn}$) and $\Delta H$ ($V_{Zn}$) were found to be very high while $\Delta H$ ($Zn_{Cu}$), $\Delta H$ ($V_{Cu}$), and $\Delta H$ ($Zn_{Cu}+V_{Cu}$) achieves a negative value. These imply that the population of Zn and Cu atoms would be higher and lower, respectively, than that of in stoichiometric CZTS for the growth conditions of GBR1 at $-1.33 \text{ eV} \leq \Delta\mu_{Cu} < -1.55$ eV. Conversely, $Sn_{Zn}$, $Sn_{Cu}$, and $V_{Sn}$ have very higher formation energies for the same point *S* as shown in Figure 4.6, which entails that the population of Sn atom would not be changed significantly with respect to its stoichiometric ratio for the points belonging to GBR1 on the same $\Delta\mu_{Cu}$ planes. Hence, these conclude that Cu/(Zn+Sn) <1 and Zn/Sn >1 ratios are evident for higher efficiency CZTS. This conclusion supports the experimental findings that the CZTS high solar conversion efficiency satisfy Cu/(Zn+Sn) ≈ 0.8 and Zn/Sn ≈ 1.2 ratios. At this end, it can be noted that DFT calculations were performed at T = 0 K. To include thermal effects on defect formation or concentration one might attempt

to incorporate vibrational energy contributions at finite temperatures with static (T = 0 K) results as outlined in reference.[188]

Table 4.3 The values of $\Delta\mu_\alpha$ ($\alpha$ = Cu, Zn, Sn, and S) at different points shown in Figures 4.7 and 4.8.

| Defects | Figure | Chemical Potential | | Points | | | |
|---|---|---|---|---|---|---|---|
| | | $\Delta\mu_{Cu}$ eV | $\Delta\mu_\alpha$ | O eV | L eV | K eV | G eV |
| $Cu_{Zn}$ | 4.7a | 0.0 | $\Delta\mu_{Zn}$ | 0.0 | 0.0 | | |
| | | | $\Delta\mu_{Sn}$ | 0.0 | -1.17 | | |
| | | | $\Delta\mu_S$ | -1.1 | -0.81 | | |
| | 4.7b | -0.16 | $\Delta\mu_{Zn}$ | 0.0 | 0.0 | | |
| | | | $\Delta\mu_{Sn}$ | -0.04 | -2.13 | | |
| | | | $\Delta\mu_S$ | -1.01 | -0.49 | | |
| | 4.7c | -0.30 | $\Delta\mu_{Zn}$ | 0.0 | 0.0 | | |
| | | | $\Delta\mu_{Sn}$ | -0.13 | -2.94 | | |
| | | | $\Delta\mu_S$ | -0.92 | -0.21 | | |
| | 4.7d | -0.53 | $\Delta\mu_{Zn}$ | 0.0 | 0.0 | | |
| | | | $\Delta\mu_{Sn}$ | -0.28 | -3.35 | | |
| | | | $\Delta\mu_S$ | -0.76 | 0.0 | | |
| | 4.7e | -0.58 | $\Delta\mu_{Zn}$ | 0.0 | 0.0 | | |
| | | | $\Delta\mu_{Sn}$ | -0.32 | -3.24 | | |
| | | | $\Delta\mu_S$ | -0.73 | 0.0 | | |
| $V_{Cu}$ | 4.8a | -0.78 | $\Delta\mu_{Zn}$ | 0.0 | 0.0 | | |
| | | | $\Delta\mu_{Sn}$ | -0.44 | -2.86 | | |
| | | | $\Delta\mu_S$ | -0.60 | 0.0 | | |
| | 4.8b | -1.33 | $\Delta\mu_{Zn}$ | 0.0 | 0.0 | -0.44 | |
| | | | $\Delta\mu_{Sn}$ | -0.89 | -1.77 | -1.33 | |
| | | | $\Delta\mu_S$ | -0.22 | 0.0 | 0.0 | |
| | 4.8c | -1.55 | $\Delta\mu_{Zn}$ | | | | 0.0 |
| | | | $\Delta\mu_{Sn}$ | | | | -1.33 |
| | | | $\Delta\mu_S$ | | | | 0.0 |

It is observed that ZnS-line ($L_3$) and $Cu_2SnS_3$-line ($L_7$) are absent on the $\Delta\mu_{Cu}$ = -1.33 eV plane, and at $\Delta\mu_{Cu}$ = -1.7 eV (see Figure 4.8d) all the Sn-S lines ($L_4$ – $L_6$ ) disappear from the chemical potential landscape of CZTS. The disappearance of $Cu_2SnS_3$-line ($L_7$) has similar physical aspect as explained for Cu-S-lines ($L_1$ and $L_2$) in

subsection 4.3.3 i.e., the formation of $Cu_2SnS_3$ is no longer possible for any values of $\Delta\mu_{Sn}$ and $\Delta\mu_S$ available on the $\Delta\mu_{Cu} \leq -1.33$ eV planes (see Figure 4.8b-d). However, disappearance of ZnS and Sn-S has extreme physical aspect which implies the co-existence of ZnS and Sn-S phases are still obvious irrespective of the values available for $\Delta\mu_\alpha$ ($\alpha$ = Zn, Sn, and S) on $\Delta\mu_{Cu} \leq$ -1.7 eV planes given by equation (4.17). The explanation for the co-existence of ZnS and Sn-S phases at $\Delta\mu_{Cu}$ = -1.7 eV can also be explained from equations 4.5-4.11 and equation (4.17). At $\Delta\mu_{Cu} = -1.7$ eV the corresponding $\Delta\mu_\alpha$ ($\alpha$ = Zn, Sn, and S) following equations (2.84) and (4.17) are

$$-1.02 \text{ eV} \leq \Delta\mu_{Zn} \leq 0 \text{ eV}, \quad (4.19a)$$

$$-1.02 \text{ eV} \leq \Delta\mu_{Sn} \leq 0 \text{ eV}, \quad (4.19b)$$

$$-0.26 \text{ eV} \leq \Delta\mu_S \leq 0. \quad (4.19c)$$

According to equation 4.7, the necessary values of $\Delta\mu_S$ at Zn-rich ($\Delta\mu_{Zn}$= 0) and Zn-poor ($\Delta\mu_{Zn} = -1.02$ eV) conditions to avoid the co-existence of ZnS are $-1.90$ eV and $-0.88$ eV, respectively. However, equation 4.19c cannot provide such a poor condition of $\Delta\mu_S$ if equation (13) holds. As a result, the formation of ZnS is evident at $\Delta H_{f,CZTS} \leq \Delta\mu_{Cu} \leq -1.7$ eV for any value of $\Delta\mu_{Zn}$. Similar argument is also valid for the occurrence of Sn-S phases at $\Delta\mu_{Cu} \leq -1.7$ eV.

4.3.6.2. Prediction of high efficiency pathway

Among possible fragmentation pathways we have considered only three pathways (equations 4.20-4.22) through which $\Delta H_{frag.,CZTS} < 0$ can be achieved, manifesting the stable formation of the material itself.[12] The pathways which possess negative fragmentation energies for CZTS are

$$Cu_2ZnSnS_4 = Cu_2SnS_3 + ZnS \quad ; \Delta H_{frag.,CZTS} = -0.11 \text{ eV}, \quad (4.20)$$

$$Cu_2ZnSnS_4 = Cu_2S + ZnS + SnS_2 \quad ; \Delta H_{frag.,CZTS} = -00.56 \text{ eV}, \quad (4.21)$$

$$Cu_2ZnSnS_4 = 2CuS+ZnS+SnS \quad ;\Delta H_{frag.,CZTS} = -0.62 \text{ eV}. \tag{4.22}$$

Since equations 4.20-4.22 possess negative fragmentation energies, synthesis of stable CZTS using either of these pathways is possible i.e., secondary phases present in those equations can be used as precursors to synthesize stable CZTS. However, the degree of stoichiometry, stability, and PV efficiency of CZTS might be varied depending on the pathway (or precursors) chosen to synthesize it. This aspect will be explored in this subsection.

CZTS synthesized by the pathway given by equation 4.20 will have lowest stability as $|\Delta H_{frag.,CZTS}|$ has lowest value of among others. This lower stability issue is also seen from Figures 4.5, 4.7, and 4.8. A little change of $\Delta\mu_{Zn}$ will destabilize the region bounded by $Cu_2SnS_3$-line ($L_7$) and ZnS-line ($L_3$) on the chemical potential landscape of CZTS. Moreover, these two lines never bound a grey region in Figures 4.7 and 4.8, i.e., at least two secondary phases ($Cu_2SnS_3$ and ZnS) would co-exist simultaneously in CZTS. Hence, equation 4.20 will not correspond to high efficiency growth condition for CZTS. The other two pathways given by equation 4.21 and equation 4.22 possess much lower $\Delta H_{frag.,CZTS}$, implying better stability. This fact is commensurate with the areas of the regions bounded by Cu-S-lines ($L_1$-$L_2$), ZnS-line ($L_3$), and Sn-S-lines ($L_4$-$L_5$) at different $\Delta\mu_{Cu}$ values (Figure 4.5). Since high efficiency region (see GBR1 in Figure 4.8b) can be achieved using both pathways given by equations 4.21 and 4.22, maximum efficiency of CZTS is extractable through these pathways if $\Delta\mu_\alpha$ ($\alpha$ = Cu, Zn, Sn, and S) are chosen appropriately (see Table 4.3 for high efficiency $\Delta\mu_\alpha$). As GBR1 corresponds to co-existence of ZnS with CZTS, the pathways those bound GBR1 can be written in the following way

$$Cu_2S+2ZnS+SnS_2 = Cu_2ZnSnS_4 + ZnS, \tag{4.23}$$

$$2CuS+2ZnS+SnS = Cu_2ZnSnS_4 + ZnS, \quad (4.24)$$

Although ZnS-CZTS interface exhibits least recombination velocity[164] and their co-existence is favorable for preventing a shunt mechanism,[73] they form higher conduction band offset (1.3 eV).[74] Such higher band offset would form high energy barrier for the carriers, which will eventually reduce the photo-current potentially.[75] As a result, PV efficiency from CZTS at a satisfactory level is unlikely to come unless its stoichiometric single-phase is achieved. To achieve the single-phase of CZTS one prescription could be the fixing the growth conditions of Cu and Sn such that corresponds to effective growth conditions e.g. GBR1 in Figure 4.8b i.e., no formation of Cu-S, Sn-S, and Cu-Sn-S phases are allowed. Then, one should let the Zn/S-growth conditions to be so rich so that $\Delta\mu_{Zn}$, $\Delta\mu_S >> 0$ (where Zn and S atoms are more readily available than their standard solid phases e.g. gaseous phases of Zn and S), however, corresponds to non-equilibrium thermodynamic conditions. Under such conditions, Zn and S atoms will have higher kinetic energies, obstructing the stable formation of ZnS phase. On the contrary, higher energetics of Zn and S atoms are likely to be compensated by the atoms of other species pertaining to poor sources, allowing the stable formation of CZTS. However, at $\Delta\mu_S >> 0$, the formation of Cu-S, Sn-S, and Cu-Sn-S phases could be probable again. To avoid those phases, $\Delta\mu_{Cu}$ and $\Delta\mu_{Sn}$ should be tuned to poor values accordingly. The detail of non-thermodynamic approach is beyond the present scope and will be presented elsewhere. In contrast, at thermodynamic equilibrium, the co-existence of ZnS phase can be avoided employing suitable Zn-poor growth condition, however, that will prompt other phases to be co-existed with CZTS, namely CuS. This CZTS-CuS phase, although is unexpected for higher PV efficiency, with intrinsic defects poses to be an alternative promising potential candidate in near IR photodetectors.[76]

*4.3.7. Conclusion*

It has been found by our theoretical analysis that synthesis of *single-phase* CZTS is not likely to occur under thermodynamic equilibrium condition. We have shown that, even though in principle single-phase "stoichiometric" CZTS is possible, the presence of a single non-stoichiometric causing defect (which may form spontaneously) can lead to mixed-phase CZTS. While non-stoichiometry is evident for CZTS, a suitable combination of chemical potentials, $\Delta\mu_\alpha$ ($\alpha$ = Cu, Zn, Sn, and S), is necessary to limit the occurrences of unwanted secondary phases to a minimum, prevent the formation of detrimental defects, and promote the benign defects to have higher efficiency CZTS for solar energy conversion. The values of chemical potentials of cations, $\Delta\mu_{Cu,}$ $\Delta\mu_{Zn}$, and $\Delta\mu_{Sn}$, can be chosen in such way so that both the maximum sulfurization and the maximum hole concentration through $V_{Cu}$ defects can be reached. The suitable combination of $\Delta\mu_\alpha$ ($\alpha$ = Cu, Zn, Sn, and S) to synthesize the efficient CZTS are found to be $-1.33$ eV $\leq \Delta\mu_{Cu} <$ $-1.55$ eV, $-0.44$ eV $\leq \Delta\mu_{Zn} \leq 0$ eV, $-1.77$ eV $< \Delta\mu_{Sn} \leq -0.89$ eV, and $-0.22$ eV $< \Delta\mu_S \leq 0$ eV. These theoretical findings explain why Cu-poor and Zn-rich conditions in experiments are frequently found to be the effective growth conditions of high efficient CZTS. In addition to justifying these two experimentally found conditions, our newly determined ranges of chemical potentials also predict that, Sn-poor and S-rich growth conditions are required as well to synthesize higher efficient CZTS. Apart from that, it has been shown that synthesis of CZTS would be accompanied with at least one secondary phase, and in the above chemical potential ranges it is most likely to be ZnS. The two pathways: (*i*) $2CuS+2ZnS+SnS = Cu_2ZnSnS_4 + ZnS$ and (*ii*) $Cu_2S+2ZnS+SnS_2 = Cu_2ZnSnS_4 + ZnS$, are found to be the most viable route for achieving CZTS with appropriate growth conditions. The above findings and methodology can be applied to further tune the growth conditions of CZTS or any other complex quaternary materials in general.

## 4.4. Pentarnary Compound: $Cu_2ZnSn(S_{1-x}Se_x)$ (CZTSSe)

### *4.4.1 Introduction*

The $Cu_2ZnSn(S_{1-x}Se_x)_4$ (CZTSSe) alloy has also been emerged as a next generation commercialized photovoltaic cell because its power conversion (solar-to-current) efficiency (PCE) has reached a benchmark 12.6%,[192] higher than that of their parent compounds: CZTS (10.1%,[155,156]) and CZTSe (11.6%[193]). Further improvement of its PCE is necessary to be a perfect replacement of current costly commercialized solar cells, namely CIGS; this primarily requires the reduction of the large open-circuit voltage ($V_{oc}$) deficit (~37%[155,192]) with respect to SQ limit[5] by a considerable amount,[194] which would improve[195] device FF (fill factor) as well. In addition, further enhancement of short-circuit current density ($J_{sc}$), although it reaches > 80%[192,196] of SQ limit, would maximize PCE. However, the progression of $V_{oc}$ and $J_{sc}$ in CZTSSe is opposite to each other in most of the samples as shown in Figure 4.9; for example, the maximum of $V_{oc}$ results minimum in $J_{sc}$. As a result, a CZTSSe sample exhibiting maximum $V_{oc}$ or $J_{sc}$ does not have highest efficiency since the product $V_{oc}*J_{sc}$ in that case is even lower than that of sample wherein neither $V_{oc}$ nor $J_{sc}$ is highest. This tells that further tuning of $V_{oc}$ and $J_{sc}$ has to be done in such way that maximizes $V_{oc}*J_{sc}$ as well, as was done in 12.6% sample, to intensify the PCE of CZTSSe further. This warrants an effective optimization of those factors/parameters which govern $V_{oc}$ and $J_{sc}$ in CZTSSe.

$V_{oc}$ and $J_{sc}$ primarily depend on several factors[162,190,197–202] such as alloy composition, single-phase crystallinity, defects population, nature of back contact (Ohmic or non-Ohmic), interface with buffer layer. Among these factors, like any other materials, the first three are most fundamentals to CZTSSe's intrinsic attributes and hence need to be optimized first before fixing the rest of the technical glitches. In CZTSSe, S-richer composition tends to increase band gap which in turn improves $V_{oc}$; in fact, $V_{oc}$ is higher

in CZTSSe than that of in CZTSe.[192,193] In contrast, higher content of S in CZTSSe

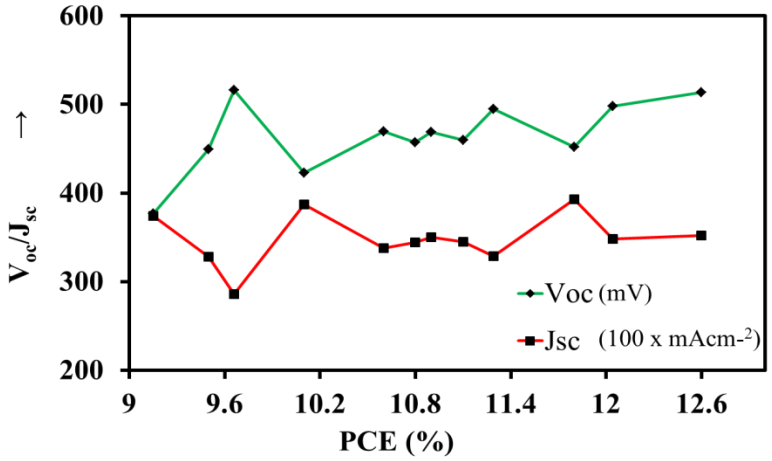


Figure 4.9 The measured $V_{oc}$ and $J_{sc}$ for different CZTSSe samples ( 9.1% -12.6%). This figure was produced using data of $V_{oc}$ and $J_{sc}$ available in Ref. [116,192,196,203] $J_{sc}$ values have been multiplied by 100 for better visibility. It is obvious from the figure that the progression of $V_{oc}$ and $J_{sc}$ in most of CZTSSe samples is inverse to each other.

reduces[199,204] hole mobility and bulk conductivity, and introduces[205–207] higher series resistance, which in principal lower $J_{sc}$. Therefore, it is obvious that neither higher (high Se-rich) nor lower (high S-rich) value of x would maximize $V_{oc}*J_{sc}$ or PCE in $Cu_2ZnSn(S_{1-x}Se_x)_4$. At this point, the burning question is what value of x would maximize $V_{oc}*J_{sc}$ in CZTSSe, thereby allowing it to exhibit PCE more than 12.6%. The answer of this question is not known precisely. In the present work, we determine an effective value of x with respect to single-phase stability and probability of forming defects. In this regard, we, at first, infer an effective range of x from recent theoretical and experimental evidences as discussed below.

The variations of $V_{oc}$, μ (hole mobility), and σ (conductivity) with composition x (= Se/(S+Se)) in CZTSSe have been documented in different studies.[198,199] Timmo[198] et al. reported that $V_{oc}$ increases linearly as x decreases (increasing S concentration) until it falls off sharply at $x < 0.15$. The $V_{oc}$ (513.4 mV) for 12.6% efficient CZTSSe corresponds to $x \approx 0.48$ value on $V_{oc}$ Vs. x plot in Ref.[198] Like $V_{oc}$, μ increases with decreasing x as well, however, drops off rapidly at $x < 0.5$. These imply that $x \leq 0.5 - \varepsilon$ (ε is any small number) be the range that may correspond to maximum $V_{oc}*J_{sc}$ in CZTSSe. On the contrary, it has been predicted based on n- and p-type doping flexibility[121] that CZTSSe alloy with $x > 0.5$ (higher Se concentration) exhibits higher efficiency; 10.1 % efficient CZTSSe validates this prediction quite well[203]. In addition, CZTSSe with efficiencies > 10.1 %, although x not known,[116,192,196,203] possess band gaps in the ranges 1.13-1.17 eV which correspond to $x = 0.5 + \varepsilon$ in the band gap (DFT-HSE) Vs. x plot in Ref..[121]Although the calculated gaps are typically underestimated, the aforementioned extrapolation of x with respect to those band gap values for CZTSSe should be fair enough. This is because theoretical band gaps of CZTSSe are in well agreement with their experimental counterparts for values at x= 0, 1 as well as $x \approx 0.6$ ($E_g$ = 1.15 eV (exp.[203]) and ≈1.17 (cal.[121])); furthermore, the change of $E_g$ in CZTSSe is almost linear with x.[121,208,209] At this point, taking two opposite scenarios of alloy composition into considerations, $0.5 - \varepsilon \leq x \leq 0.5 + \varepsilon$ appears to be most suitable range to extract maximum efficiency from CZTSSe alloy. Unfortunately, no theoretical investigation effort has been made considering the closest values to x = 0.5 per unit cell of CZTSSe. For the purpose, we choose ε such a way that corresponds two closest possible compositions to x = 0.5 (4 S and 4 Se) per unit cell including, which are $x = 0.5 - \varepsilon = 0.375$ ( 5 S and 3 Se, S-rich) and $x = 0.5 + \varepsilon = 0.625$ (3 S and 5 Se, Se-rich).

Apart from alloy composition, $V_{oc}$ and $J_{sc}$ highly depend on band offset[190] which is formed while a secondary phase co-exists with the primary phase. In the case of 12.6% CZTSSe, Zn(S, Se) co-exist with it, and the conduction band offset (CBO) can be of 1.3 eV.[189] Such a higher CBO and heterojuction reduce both $V_{oc}$ and $J_{sc}$, and eventually the PCE.[190] In addition to band offset/heterojunction, the presence of interface/bulk defects controls carrier mobility, carrier lifetime, diffusion length, and so on, which in turn impact $V_{oc}$ and $J_{sc}$; beneficial defects improve those factors while detrimental ones do the other way. The large $V_{oc}$ deficit in CZTSSe in fact has been attributed to severe band tailing caused by intrinsic point defects.[201] Therefore, further improvement of PCE requires to synthesis CZTSSe as a single-phase in conjunction with maximum beneficial and least detrimental defects, which in turn are contingent on growth conditions. The growth conditions[192](Cu-poor and Zn-rich) which have been using for synthesizing high efficient CZTSSe promote co-existence of Zn(S, Se) phases and are based on the parent compounds. Despite having the same kesterite crystal structures as of parent compounds, the high efficient growth condition for CZTSSe could be different since mixing[121] of S and Se in forming stable CZTSSe costs additional energy. This warrants a comprehensive investigation on growth conditions of CZTSSe. However, to the best of our knowledge, no effort has been made in this regard yet. This leads us to determine the high efficient growth conditions for CZTSSe in the present work.

Determination of a high efficient growth condition at which a CZTSSe alloy would exhibit desired efficiency invokes chemical potential analysis in conjunction with defect calculations. The proceeding of the former requires solving the free energy equation of CZTSSe with that of each secondary phase. This leads to a mathematical impasse for CZTSSe because its free energy equation contains five variables including two anionic while a binary secondary phase has only two variables (a cationic and an anionic, S or

Se) in their free energy equations. A possible simple solution of that is to keep fixing at least two variables (growth conditions). However, determining a suitable choice of two constraints out of numerous degrees of freedom is a challenging task, which was not attempted for CZTSSe before. In the present work, we intend to provide pathways for proceeding chemical potential analysis of CZTSSe, determining its higher PCE growth conditions for three suitable alloy (x) compositions.

*4.4.2 Computational Details*

The results presented here are based on DFT+U calculations of three different alloy compositions, x = 0.375, 0.5, and 0.625. The choice of this over other post-DFT methods and in the case of Cu 3d[10] compounds has been justified in Ref.[17]The used Monkhorst–Pack[77] k-point sampling for ionic relaxation of CZTSSe was 13×13×7. A 2×2×1 supercell (64 atoms) was used for the defect calculations with a k-point sampling of 5×5×5.

*4.4.3 Single-phase stability*

To determine the single-phase stability of CZTSSe it is necessary to invoke chemical potential or equilibrium growth conditions analysis. The common approach in this regard is to draw chemical potential landscapes upon solving free energy equations of secondary phases with that of the primary phase.[17,160]The growth conditions to form stable CZTSSe at thermodynamic equilibrium

x=0.375: $2\Delta\mu_{Cu} + \Delta\mu_{Zn} + \Delta\mu_{Sn} + 1.5\Delta\mu_{Se} + 2.5\Delta\mu_{S} = -9.538$ eV, (4.25a)

x=0.5: $2\Delta\mu_{Cu} + \Delta\mu_{Zn} + \Delta\mu_{Sn} + 2.0\Delta\mu_{Se} + 2.0\Delta\mu_{S} = -11.210$ eV, (4.25b)

x=0.625: $2\Delta\mu_{Cu} + \Delta\mu_{Zn} + \Delta\mu_{Sn} + 2.5\Delta\mu_{Se} + 1.5\Delta\mu_{S} = -12.871$ eV. (4.25c)

To avoid the formation of secondary phases

$Cu_2ZnSnS_4$: $2\Delta\mu_{Cu} + \Delta\mu_{Sn} + \Delta\mu_{Zn} + 4\Delta\mu_{S} = \Delta H_{f,CZTS} \leq -4.587$ eV, (4.26a)

| | | |
|---|---|---|
| $Cu_2ZnSnSe_4$: | $2\Delta\mu_{Cu} + \Delta\mu_{Sn} + \Delta\mu_{Zn} + 4\Delta\mu_{Se} = \Delta H_{f,CZTSe} \leq -3.935$ eV, | (4.26b) |
| $Cu_2SnS_3$: | $2\Delta\mu_{Cu} + \Delta\mu_{Sn} + 3\Delta\mu_{S} < \Delta H_{f,Cu_2SnS_3} = -2.58$ eV, | (4.26c) |
| $Cu_2SnSe_3$: | $2\Delta\mu_{Cu} + \Delta\mu_{Sn} + 3\Delta\mu_{Se} < \Delta H_{f,Cu_2SnSe_3} = -2.245$ eV, | (4.26d) |
| $Cu_2S$: | $2\Delta\mu_{Cu} + \Delta\mu_{S} < \Delta H_{f,Cu_2S} = -0.807$ eV, | (4.26e) |
| $Cu_2Se$: | $2\Delta\mu_{Cu} + \Delta\mu_{Se} < \Delta H_{f,Cu_2Se} = -0.558$ eV, | (4.26f) |
| CuS: | $\Delta\mu_{Cu} + \Delta\mu_{S} < \Delta H_{f,CuS} = -0.513$ eV, | (4.26g) |
| CuSe: | $\Delta\mu_{Cu} + \Delta\mu_{Se} < \Delta H_{f,CuSe} = -0.395$ eV, | (4.26h) |
| ZnS: | $\Delta\mu_{Zn} + \Delta\mu_{S} < \Delta H_{f,ZnS} = -1.895$ eV, | (4.26i) |
| ZnSe: | $\Delta\mu_{Zn} + \Delta\mu_{S} < \Delta H_{f,ZnSe} = -1.621$ eV, | (4.26j) |
| SnS: | $\Delta\mu_{Sn} + \Delta\mu_{S} < \Delta H_{f,SnS} = -1.048$ eV, | (4.26k) |
| SnSe: | $\Delta\mu_{Sn} + \Delta\mu_{Se} < \Delta H_{f,SnSe} = -1.007$ eV, | (4.26l) |
| $SnS_2$: | $\Delta\mu_{Sn} + 2\Delta\mu_{S} < \Delta H_{f,SnS_2} = -1.328$ eV, | (4.26m) |
| $SnSe_2$: | $\Delta\mu_{Sn} + 2\Delta\mu_{Se} < \Delta H_{f,SnSe_2} = -0.827$ eV, | (4.26n) |
| $Sn_2S_3$: | $2\Delta\mu_{Sn} + 3\Delta\mu_{S} < \Delta H_{f,Sn_2S_3} = -2.416$ eV. | (4.26o) |

Drawing a chemical potential landscape of a compound can be done in two approaches: solving simultaneously the n-dimensional free energy equation of that primary phase either (i) with those of suitable n-1 secondary phases or (ii) with that of a secondary phase at a time. The approach (i) can be proceeded if and only if n-1 different secondary phases co-exist with the primary phase at a given growth condition. However, for a compound like CZTSSe, it is highly impossible that four different (must be different in atomic species as approach (i) requires) secondary phases would co-exist with it at a growth conditions e.g. Cu-/Sn-poor and Zn-rich (high efficient growth conditions) which favor the formation of Zn-S/Se phases only. As a result, although approach (i) provides mathematical convenience, is not well-suited to chemical potential analysis of a multi-cations compound like CZTSSe. In contrast, approach (ii) considers the secondary phases are no longer coupled, thereby demonstrating the probability of co-existing each secondary phase independently with the primary phase at a given growth conditions. This approach, although ignores coupling between the secondary phases during the synthesis process, is good enough[17,160] to reproduce experimental results. However, the latter approach experiences a mathematical impasse for CZTSSe while solving solving

Equations 4.25 and 4.26. Because the lowest order secondary phase in the present discussion is a binary phase; a free energy equation (see Equations (4.26e-o)) would span a two dimensional linear space (two variables: one cationic and one anionic, S or Se) whereas a CZTSSe has five variables, three cations and two anions (S and Se) (see Equations 4.25). Therefore, Equations 4.25 and Equations (4.26e-o) cannot be solved simultaneously unless two variables are allowed to be fixed. Since fixing two variables out of five can be done in many ways, an effective choice of that is needed to make the chemical potential analysis accessible without losing any meaningful details. For this, we choose two suitable constraints which are Cu-poor ($\Delta\mu_{Cu} < 0$) and S-rich ($\Delta\mu_S = 0$) in drawing the chemical potential landscapes of CZTSSe for three different alloy compositions shown in Figure 4.10. Constraining two variables further resolves the issue in projecting five dimensional single-phase stability of CZTSSe onto three dimensional chemical potential diagrams. The aforementioned two constraints were chosen based on following experimental facts. First of all, Cu-poor growth condition populates $V_{Cu}$ (Cu-vacancy) which in turn maximizes p-type activity in CZTS(e) based compounds.[162] In fact, all high efficient CZTSSe (Cu/(Zn+Sn) ≈ 0.8-0.85)[168,194]were synthesized at this growth condition. Further, it is the preferable growth condition[197,210] for avoiding detrimental defects such as $Cu_{Zn}$ + $Sn_{Zn}$ and $Cu_{Sn}$, and eliminating unwanted Cu-S/Se secondary phases. The values at which $V_{Cu}$ becomes spontaneous ($\Delta H (V_{Cu}) < 0$, $\Delta H (\delta)$ = formation energy of a single defect δ) was chosen as poor value for the present work. On the other hand, the reason to choose $\Delta\mu_S = 0$ as another constraint is to avoid most detrimental anionic defect, $V_S$ (S-vacancy)[31] as it introduces deeper donor level than that of $V_{Se}$ (Se-vacancy); further, the formation of $V_S$ is more probable over $V_{Se}$ in their parent compounds. These Cu-poor and S-rich constraints define the plane of each right triangle in Figure 4.10 while two cationic growth conditions are allowed to vary along abscissa

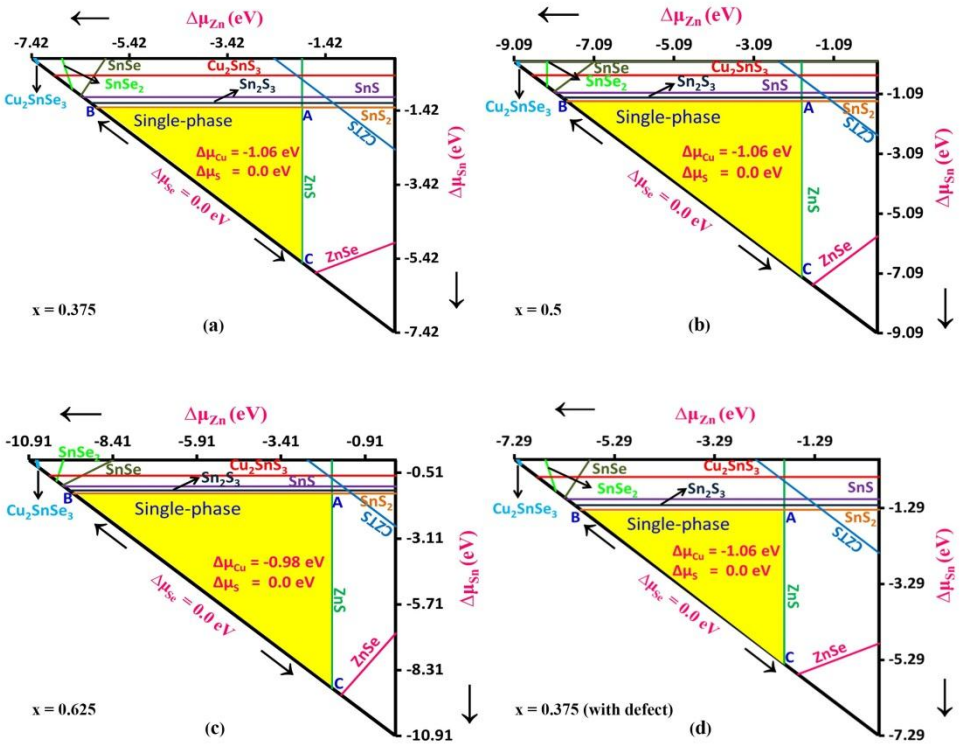


Figure 4.10 Chemical potential landscapes of CZTSSe for three different alloys: x = 0.375, 0.5 (a), and 0.625(c). Cu (poor) and S (rich) growth conditions are fixed on each plane in the triangles. Each yellow bounded region on those Cu-poor/Se-rich planes corresponds to single-phase growth zone of respective CZTSSe; area of which is commensurate with the respective CZTSSe's single-phase stability; the more Se in the composition, higher the stability. Figure (d) was drawn considering a single defect ($V_{Cu}$) in CZTSSe (x = 0.375) supercell (64 atoms). Unlike CZTS, the single-phase stability of CZTSSe remains intact even with the presence of a single-defect; other alloys exhibit similar feats which, however, were omitted here to avoid redundancy of figures.

and height of those triangles. Se growth condition is fixed along any line parallel to diagonal which represents its rich value, and becomes poorer and poorer towards the origin. composition or x increases in the samples. Since cationic stoichiometry and

ordering remain same in the crystal structures of CZTSSe and its parent compounds, the larger yellow regions in Figure 4.10 can be solely attributed to non-zero values of x in CZTSSe i.e., due to alloy of S

The yellow regions in Figure 4.10 represent single-phase growth zones of CZTSSe. The areas of those regions are commensurate with their single-phase stabilities as well; larger the areas, higher the stabilities. Compared to those for stoichiometric CZTS(e), the areas of these regions are significantly larger, manifesting higher single-phase the stabilities of CZTSSe than their parent structures.[17,162] The areas of these regions get bigger and bigger as Se

and Se; such larger single-phase growth zones are usually rare for multi-cations-anions compound. As a result, unlike CZTS,[17] the single-phase stability is too robust to be lost even with a presence of a spontaneous single defect (see Figure 4.10d). This higher single-phase stability would ensure two desirable aspects of solar-to-current conversion process in CZTSSe: (i) no unwanted mid-gap states due to hetero-junction interface, thereby preventing recombination of carriers and (ii) no inherent band-offset like in CZTS i.e., no energy barrier for photo-generated electrons across the conduction band. The probability of forming various intrinsic defects in those single-phase regions is shown in Figure 4.10.

Note that no CZTSe phase was shown in Figure 4.10 because the solutions of Equation (4.25) and Equation (4.26b) yields $\Delta\mu_{Se} > 0$ with respect to the aforementioned constraints taken for each x. CZTSe line satisfying these values lies outside the triangle i.e., belongs to non-equilibrium region and hence beyond the scope of present discussion.

*4.4.4 Defect calculation*

Figure 4.11 represent the probability of forming the intrinsic defects with respect to single-phase growth condition (yellow regions) in Figure 4.10. Point A has the same growth conditions (($\Delta\mu_{Zn}$, $\Delta\mu_{Sn}$) = (-1.895, -1.328)) for all three compositions. At point A, most of the defects have $\Delta H$ ($\delta$) > 0 except $V_{Cu}$ and $V_{Se}$. Although $V_{Cu}$ is a desirable defect for enhanced p-type activity, the presence of $V_{Se}$ could introduce numerous deep donor levels which in turn could act as recombination centers. Further, $V_{Se}$ population would be the most dominant as it possesses lowest negative formation energy at this point. Therefore, formation of $V_{Se}$ needs to be avoided or minimized, which requires Se-rich growth conditions. Points B and C correspond to Se-rich growth conditions as well as the same Sn-growth ($\Delta\mu_{Sn}$ = -1.328 eV) and Zn-growth ($\Delta\mu_{Zn}$ = -1.895 eV) conditions, respectively for all compositions. Despite having $\Delta H$ ($V_{Se/S}$) > 1 eV due to

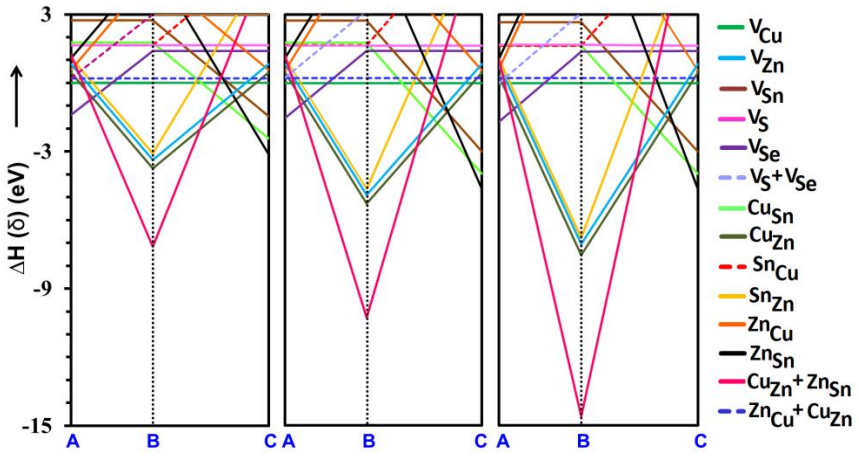


Figure 4.11 Defects formation energies of various defects in CZTSSe for its different alloys. The probability of forming defects in the figure was determined with respect to single-phase growth zones in Figure 4.4.2(a-c). The defects which have formation energies higher than 3 eV were not shown. From the figure, it is obvious that defects are evident in the single-phase CZTSSe, no matter the growth condition is.

both anions-rich conditions at point B, cations-poor conditions let few cationic defects ($Sn_{Zn}$, $Cu_{Zn}$, and $V_{Zn}$) becoming spontaneous including detrimental defect $Cu_{Zn}$ + $Sn_{Zn}$ which has the lowest formation energy ($\Delta H$ ($Cu_{Zn}$ + $Sn_{Zn}$) < -7.17 eV) in all x. This detrimental defect becomes more and more probable with increasing Se since $\Delta\mu_{Zn}$ extends to poor conditions farther in Figure 4.10a and 4.10b with increasing x. In contrast, growth conditions at point C raises $\Delta H$ ($Cu_{Zn}$ + $Sn_{Zn}$) to more than 6 eV, however, makes the formation of another harmful defect ($Cu_{Sn}$) spontaneous. Therefore it is obvious that, at least one unwanted highly populated defect will be present inside the yellow regions (single-phase growth zone) in Figure 4.10 irrespective of compositions and growth conditions. Hence, growth conditions in Figure 4.10 or 4.11, although allow the single-phase to be formed, are not optimized enough for CZTSSe for exhibiting high efficiency. Nevertheless, Figures 4.11 provide a qualitative idea in conjecturing a high efficient growth conditions for CZTSSe which are as follows. At points B and C, all anionic growth conditions are rich; however, cationic growth conditions are $\Delta\mu_{Zn} << \Delta\mu_{Sn} < 0$ and $\Delta\mu_{Sn} << \Delta\mu_{Zn} < 0$, respectively. As a result, although $\Delta H$ ($V_{Se/S}$) are highest at those points, at least one detrimental cationic defect ($Cu_{Zn}$ + $Sn_{Zn}$ or $Cu_{Sn}$) is spontaneous. In contrast, neither $Cu_{Zn}$ + $Sn_{Zn}$ nor $Cu_{Sn}$ is spontaneous at point A because cationic growth conditions $\Delta\mu_{\alpha}$ ($\alpha$ = Cu, Zn, and Sn) are poor but comparable (at least one is not significantly lower than the other) to each other. This tells that, richer anion growth conditions and equally poor (or comparable each other) cations growth conditions would be required to minimize the probability of forming unwanted defects. However, a natural question arises at this point: is the single-phase of CZTSSe achievable under those growth conditions? The answer of this question requires redrawing Figure 4.10 keeping $\Delta\mu_{\alpha}$ ($\alpha$ = Cu, Zn, and Sn) fixed which is, however, is not physically possible. Hence, a

different approach is required to answer the above question which will be pursued in the following.

*4.4.5 High efficient growth conditions and alloy composition*

Figure 4.12 represents a different approach of chemical potential diagram of CZTSSe keeping all the cationic growth conditions fixed. This reduces Equations (4.25) to two dimensional linear space and removes solving issues with binary phases. In this case, formation enthalpy equations of primary and secondary phases (Equations 4.25 and 4.26) take the following forms.

| | | |
|---|---|---|
| CZTSSe (x=0.375): | $\Delta\mu_{Se} \geq$ -6.359 eV -1.667 $\Delta\mu_S$ -ε/1.5, | (4.27a) |
| CZTSSe (x=0.5): | $\Delta\mu_{Se} \geq$ -5.605 eV -$\Delta\mu_S$ - ε/2, | (4.27b) |
| CZTSSe (x=0.625): | $\Delta\mu_{Se} \geq$ -5.148 eV -0.6$\Delta\mu_S$ - ε/2.5, | (4.27c) |
| $Cu_2ZnSnSe_4$: | $\Delta\mu_{Se} \geq$ -0.984 eV - ε/4, | (4.27d) |
| $Cu_2SnSe_3$: | $\Delta\mu_{Se} \geq$ -0.748 eV - 0.667 $\Delta\mu_{Cu}$ - 0.333 $\Delta\mu_{Sn}$, | (4.27e) |
| ZnSe: | $\Delta\mu_{Se} \geq$ -1.621 - $\Delta\mu_{Zn}$, | (4.27f) |
| $SnSe_2$: | $\Delta\mu_{Se} \geq$ -0.414 eV - 0.5 $\Delta\mu_{Sn}$, | (4.27g) |
| SnSe: | $\Delta\mu_{Se} \geq$ -1.007 eV - $\Delta\mu_{Sn}$, | (4.27h) |
| $Cu_2ZnSnS_4$: | $\Delta\mu_S \geq$ -1.147 eV -$\Delta$/4, | (4.27i) |
| $Cu_2SnS_3$: | $\Delta\mu_S \geq$ -0.861 eV - 0.667 $\Delta\mu_{Cu}$ - 0.333 $\Delta\mu_{Sn}$, | (4.27j) |
| ZnS: | $\Delta\mu_S \geq$ -1.895 - $\Delta\mu_{Zn}$, | (4.27k) |
| $SnS_2$: | $\Delta\mu_S \geq$ -0.664 eV - 0.5 $\Delta\mu_{Sn}$, | (4.27l) |
| SnS: | $\Delta\mu_S \geq$ -1.048 eV - $\Delta\mu_{Sn}$, | (4.27m) |
| $Sn_2S_3$: | $\Delta\mu_S \geq$ -0.805 eV - 0.667 $\Delta\mu_{Sn}$. | (4.27n) |

Where $\varepsilon = 2\Delta\mu_{Cu} + \Delta\mu_{Zn} + \Delta\mu_{Sn}$. The equality sign in the above equations corresponds to stable formation while non-equality sign involves abundance in growth conditions which may lead to spontaneous formation and dissociation of the corresponding phases. As a result, unlike in Figure 4.10, the stable formation of the phases is represented only by the respective lines in Figure 4.12, and the region that satisfies inequality conditions of Equation 4.27 corresponds to

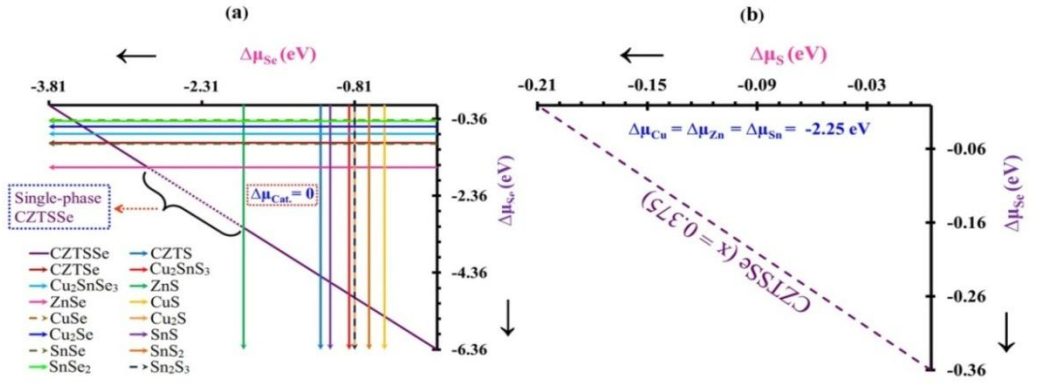


Figure 4.12 The formation of CZTSSe and its different secondary phases with respect to S ($\Delta\mu_S$) and Se ($\Delta\mu_{Se}$) growth conditions while keeping cationic growth conditions fixed: (a) all cations-rich and (b) all cations-poor. The diagonal line represents stable formation of CZTSSe while all other arrow ended lines in (a) indicate the formation of secondary phases. Each arrow corresponding to inequality sign in Equation (4.27) indicates unbound $\Delta\mu_{S/Se}$ poor value of respective phase. The unbounded values were chosen to extrapolate the co-existence of secondary phases (intersecting points with diagonal) with CZTSSe at given growth conditions for the primary phase. The single-phase of CZTSSe was indicated by the broken line. Figure (b) represents a high efficient growth conditions at which no secondary phases form.

unstable formation of that respective phase. In Figure 4.12, thermodynamically stable multi-phases CZTSSe (CZTSSe + Secondary phase(s)) will be formed only at the intersecting points with CZTSSe line (e.g., points).

To avoid the redundancy of figures, only x =0.375 was chosen as for Figure 4.12 since other compositions (x = 0.5 and 0.625) will have similar figures except extended poor cations/anions-growth conditions due to lower $\Delta H_{f,CZTSSe}$ than that of x=0.375. In Figure 4.12, two different growth conditions: all-cations-rich (see (a)) and all-cations-

equally-poor (see (b)) were used. The later growth conditions were parameterized in such a way so that Equation (4.27a-c) yield enough anions richer growth conditions ($\Delta\mu_{S/Se}$) for which $\Delta H$ ($V_{S/Se}$) ≥ 1 eV in Figure 4.13. This gives $\Delta\mu_{Zn} = \Delta\mu_{Sn} = \Delta\mu_{Cu}$ = - 2.25 eV, -2.60 eV and -2.99 eV for x = 0.375, 0.5, and 0.625, respectively; Equations (4.26) are satisfied at these conditions i.e., no secondary phases survive at these cationic-poor growth conditions. Further, these $\Delta\mu_{\alpha}$ (α = Cu, Zn, Sn, S, and Se) values satisfy equality conditions of Equations (4.27a-c) and hence correspond to stable formation of single-phase CZTSSe as well. For example, $\Delta\mu_{Zn} = \Delta\mu_{Sn} = \Delta\mu_{Cu}$ = - 2.25 eV conditions in Equation (4.27a) generate Figure 4.12b wherein no secondary phases representing lines exist; the only available line (broken) represents the stable single-phase CZTSSe at thermodynamic equilibrium. $\Delta H$ ($V_{S/Se}$) and $\Delta H$ ($V_S + V_{Se}$) in Figure 4.13 were calculated using S/Se-growth conditions along this single-phase line. The defect formation energies with respect to these anionic and cationic growth conditions are presented in Table 4.4.

In Table 4.4, all the defects except $V_{Cu}$, $Zn_{Cu}$, and $V_{Zn}$ (x = 0.625) have positive formation energies. $V_{Cu}$ is desirable defect for enhanced p-type activity, and $Zn_{Cu}$ is not detrimental, all it causes n-type activity in the parent compounds. Since $V_{Cu}$ dominates over $Zn_{Cu}$, p-type activity would prevail in CZTSSe. Other probable defects $Cu_{Zn} + Zn_{Cu}$, $Zn_{Sn}$ and $V_{Zn}$ in Table 4.4 were not termed as detrimental ones in the case of parent structures. In addition, all anionic defects, while forming independently or as a pair, have higher formation energies >1 (see Figure 4.13).Therefore, growth conditions in Table 4.4 can be termed as effective growth conditions for synthesizing high efficient CZTSSe (x = 0.375, 0.5, and 0.625). Since the minimum values of $\Delta H$ ($V_{S/Se}$) are not high enough, anionic defects could be formed introducing

Table 4.4 Defect formation energies at all cations-equally-poor and anions rich/richer growth conditions.

| Defects | ΔH (δ) eV | | | Growth Conditions eV | | |
|---|---|---|---|---|---|---|
| | Alloy Composition | | | Alloy Composition | | |
| | 0.375 | 0.5 | 0.625 | 0.375 | 0.5 | 0.625 |
| $V_{Cu}$ | -1.2 | -1.21 | -2.02 | $\Delta\mu_{Cations}$ = | | |
| $Cu_{Sn}$ | 2.04 | 2.03 | 1.98 | | | |
| $Cu_{Zn}$ | 1.29 | 1.29 | 1.23 | | | |
| $V_{Sn}$ | 1.82 | 1.80 | 1.79 | | | |
| $Sn_{Cu}$ | 1.38 | 1.38 | 1.28 | | | |
| $Sn_{Zn}$ | 1.68 | 1.66 | 1.63 | -2.25 | -2.60 | -2.99 |
| $V_{Zn}$ | 0.47 | 0.46 | -0.30 | | | |
| $Zn_{Cu}$ | -0.27 | -0.29 | -0.32 | | | |
| $Zn_{Sn}$ | 0.51 | 0.53 | 0.48 | | | |
| $Zn_{Cu}$ + $Cu_{Zn}$ | 0.2 | 0.21 | 0.21 | | | |
| $Cu_{Zn}$ + $Sn_{Zn}$ | 2.63 | 2.59 | 2.55 | | | |
| $V_S$ | 1.65 | 1.63 | 1.67 | $\Delta\mu_S$ = 0.0 | 0.0 | 0.0 |
| | 1.37 | 1.22 | 1.06 | $\Delta\mu_S$ = - 0.22 | - 0.41 | - 0.61 |
| $V_{Se}$ | 1.40 | 1.40 | 1.37 | $\Delta\mu_{Se}$ = 0.0 | 0.0 | 0.0 |
| | 1.04 | 1.00 | 1.01 | $\Delta\mu_{Se}$ = - 0.36 | - 0.41 | - 0.36 |
| $V_S$ + $V_{Se}$ | 2.64 | 2.76 | 2.71 | $\Delta\mu_S$ = 0.0<br>$\Delta\mu_S$ = - 0.22 | 0.0<br>- 0.41 | 0.0<br>- 0.61 |
| | 2.78 | 2.76 | 2.46 | $\Delta\mu_S$ = -0.36<br>$\Delta\mu_{Se}$ = 0.0 | -0.41<br>0.0 | -0.36<br>0.0 |

deep donor levels. Further optimization of anion growth conditions could reduce the probability of forming detrimental anionic defects even further; this can be realized from Figure 4.13 and will be discussed here. In CZTSSe, the most probable anionic defect is $V_{Se}$ which has formation energy minimum ($\Delta H$ ($V_{Se}$) ≈1) at $\Delta\mu_{Se}$ = -0.41 eV for x=0.5. $\Delta\mu_{Se}$ $\rightarrow$0 raises $\Delta H$ ($V_{Se}$ ), however, makes $\Delta H$ $(V_S)_{x=0.625}$ lower as $\Delta\mu_S$ decreases with increasing $\Delta\mu_{Se}$ (See Equations 4.4.3a-c)). Therefore, $\Delta\mu_{S/Se}$ should be chosen such a way that raises both $\Delta H$ ($V_{S/Se}$) from their minimum values for all compositions. This corresponds to $\Delta\mu_{Se}$ richer conditions over $\Delta\mu_S$. For example, both have higher values from their minimum and equal to each other at point P, Q, and R for x = 0.375, 0.5, and

0.625, respectively. In these conditions, $\Delta H\ (V_{S/Se})$ are highest and lowest for x = 0.375 and x = 0.625, respectively. In contrast to Figure 4.13a, $\Delta\mu_S \rightarrow 0$ conditions would be preferable for pair formation ($V_S + V_{Se}$) since $\Delta H\ (V_S + V_{Se}) > 2.62$ eV for all compositions at that growth condition as shown in Figure 4.13b. Under this circumstance, one has to choose either S-rich or S-rich conditions. Since $\Delta H\ (V_S + V_{Se})_{min} > 2^*\Delta H\ (V_{S/Se})_{min}$ and is more than 2.44 eV, the probability of forming anionic defects as a pair is very low. As a result, a due consideration should be given in case of independent formation of $V_{S/Se}$ in which $\Delta\mu_{Se} \rightarrow 0$ and corresponding $\Delta\mu_S$ would be effective anionic growth conditions.

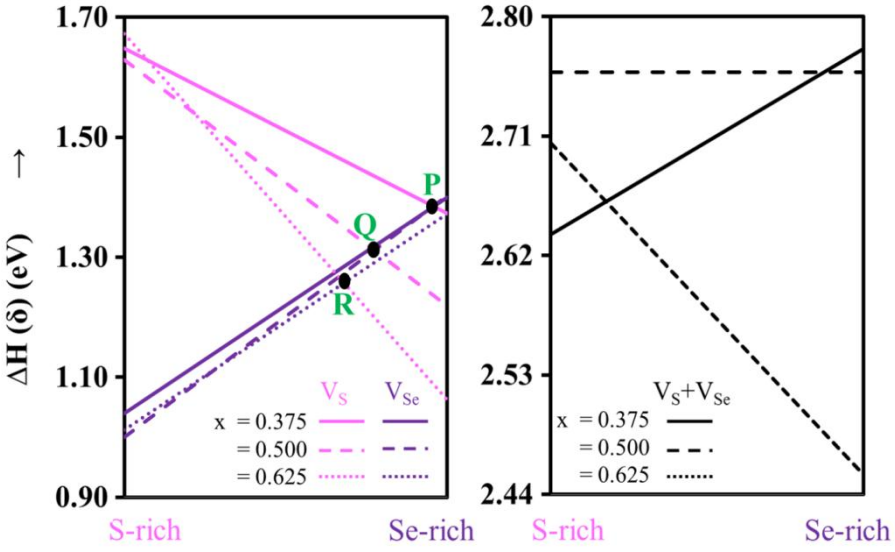


Figure 4.13 Anionic defect formation energies of CZTSSe for three different composition alloys (x = 0.375, 0.5, and 0.625) at fixed cationic growth conditions. All three cationic growth conditions $\Delta\mu_\alpha$ (α = Cu, Zn, and Sn) were fixed as equally poor as to produce $\Delta H\ (V_{S/Se}) \geq 1$ eV in Equation 4.27a-c. The poor values of $\Delta\mu_{Se}$ and $\Delta\mu_S$ at S-rich and Se-rich growth conditions respectively are presented in Table 4.4. P, Q, and R the optimal values to avoid anionic defects for each x

In addition to growth conditions, the probability of independent formation of $V_{S/Se}$ varies with alloy composition as shown in Figure 4.13, and further optimization of x would minimize the number of $V_{S/Se}$, eventually enhancing the PCE of CZTSSe. x = 0.625 (Se-rich), which exhibits highest single-phase stability, is prone to experiencing $V_S$ defect; in fact, $\Delta H$ ($V_S$) is minimum for x =0.625 at Se-rich growth conditions. Further, higher vapor pressure of S than that of Se makes the formation of detrimental $V_S$ more facile over $V_{Se}$.[197] Therefore, although Se-rich composition exhibits few better electronic attributes such as shallower donor levels, lower effective mass, higher dielectric constant, and smaller series resistance over S-rich counterpart, the population of $V_S$ could be high which is not desirable at all. In contrast, defects are less probable in S-rich composition even in Se-rich growth conditions. Further, band gap increases with the increment of S content in CZTSSe which tends to $V_{oc}$ and FF as well. However, series resistance increases with increasing band gap in CZTSSe that reduces FF which is not desirable as well for higher PCE. Under these circumstances, x = 0.5 CZTSSe appears as an effective composition for CZTSSe because (i) $\Delta H$ (δ) including $\Delta H$ ($V_{S/Se}$) are higher in x = 0.5 (Se-rich) even at Se-rich growth conditions, (ii) the hole conductivity is maximum for x = 0.5,[199] and (iii) x = 0.5 corresponds to band gap ~1.20 eV in HSE band gap Vs x, which is close to the band gap (~1.15 eV) that leads to observed empirical optimal efficiency on band-gap-dependent FF profile. Further, areas of single-phase growth zones in those compositions, although smaller than that in x =0.625, is larger enough to retain the single-phase stability.

From Figure 4.13, it is obvious that the t formation of anionic defects as independently ($V_S$ and $V_{Se}$) rather than as a pair ($V_S$ + $V_{Se}$) is more probable. In the case of independent formation, unlike the case as in parent compounds, $V_{Se}$ has lower formation energy than that of $V_S$ in CZTSSe, and hence $V_{Se}$ will dominate over $V_S$ at all

anions-rich conditions. Since a donor level introduced by $V_{Se}$ is shallower than that by $V_S$, CZTSSe would experience lesser recombination centers over CZTS. Apart from higher single-phase stability, it is the alloy of S and Se which improves the anionic defects formation scenario with respect to the parent compounds, and this is probably the another reason why CZTSSe exhibits better performance than CZTS.

*4.4.6. Conclusion*

We, for the first time, present a pathway to determine high efficient growth conditions for a material comprising five atomic species (three cations and two anions e.g. CZTSSe). It is found that all cations equally poor ($\Delta\mu_{Cu} \approx \Delta\mu_{Zn} \approx \Delta\mu_{Sn}$) and anionic (S/Se)-richer) growth conditions, different from the conditions as in higher efficient parent compounds, are needed for achieving higher PCE of CZTSSe. These growth conditions allow CZTSSe to be formed as a single-phase in conjunction with promoting and prohibiting beneficial and detrimental defects, respectively. It is found that the alloy of S and Se makes CZTSSe better solar absorber over parent compounds. Because not only does this provide higher single-phase stability, but also make the most unwanted anionic defect ($V_S$ as in CZTS[17]) less probable, thereby ensuring better $J_{sc}$. Further, the presence of S, providing higher band gap, secures higher $V_{oc}$ in CZTSSe[192,193] over CZTSe. In addition, the probability of forming all anionic defects including other intrinsic defects can be minimized by tuning the alloy composition. Based on defect calculations in conjunction with recent theoretical and experimental evidences, it was predicted that x = 0.5 would be effective alloy composition for a high efficient CZTSSe.

# Chapter 5

# New PV Material ($CuSnW_2O_8$)

## 5.1 Introduction

In the present work, we propose, for the first time, a quaternary oxide, $CuSnW_2O_8$ (CTTO), that may be a new solar absorber material with great promise for affordable PV application. The reason for CTTO's promise is due to its electronic properties and stability, as determined by density functional theory (DFT) and post-DFT methods.

We chose two inexpensive and non-toxic cations, Cu and Sn, to add to $WO_3$, due to their contributions in reducing the band gap in $CuWO_4$ (2.30 eV[211]) and α-$SnWO_4$ (1.64 eV[151]). In addition, the optimal band gap in CZTS for PV application can be attributed to the simultaneous contributions of Cu 3d and Sn 5s at valence band maximum (VBM) and conduction band minimum (CBM), respectively. A similar contribution from Cu and Sn is therefore expected when added to $WO_3$, resulting in an anticipated reduction in band gap in CTTO. In addition to band gap engineering, as in CZTS, higher p-type activity (such as in any other Cu-based compounds through Cu vacancies) and higher electron mobility (due to the spherical nature of the Sn 5s orbital at CBM) could be likely outcomes in synthesized CTTO. Finally, as in other W-based oxides, e.g., $CuBiW_2O_8$,[12] enhanced light absorption is expected in CTTO, as well. Therefore, CTTO promises to be the sought-after ideal solar absorber material. As a new material, the success in predicting PV characteristics of CTTO lies in upon the successfully determination of its crystal structure.

## 5.2 Computational Details

In addition to DFT, DFT+U[39,43,58] and Hybrid functional (HSE06[133]) (μ=0.2, α=0.25 $EXC_{HF}$) were employed to overcome the shortcoming of DFT—i.e., the underestimation

of electron localization for systems with localized $d$ and $f$ electrons.[58–60] DFT-HSE06 was employed to calculate electronic band structure and density-of-states (DOS) calculations of the pristine unit cell. However, DFT+U was used for optical absorption calculation of pristine CTTO. The reason for that was having an absorption spectrum of pristine CTTO with detailed features, which requires a very high K-sampling as well as enough empty bands. Such requirements could not be achieved with HSE06 for a multi-cations material like CTTO within our computation resource. In contrast, DFT+U is computationally convenient and hence, generating a desirable absorption spectrum was possible. Further, a comparison between DFT+U and HSE06 band structures and p-dos were made, which exhibited negligible dissimilarity between those (see Figure 5.4) except the difference in band gaps. So, it was expected that DFT-HSE06 optical absorption will have the same features as does DFT+U except delayed onset. Considering this fact in conjunction with computational convenience, we were convinced to employ DFT+U for optical absorption calculations for pristine to all supercells (1x2x2) of CTTO. The unit cell of CTTO was converged with DFT (or DFT+U) at 7x11x13 k-mesh, and the converged unit cell was later used for all HSE06 calculations. Although it is better to use a higher K-mesh for DOS calculation, we had to restrict ourselves to a smaller 3×5×5 Monkhorst–Pack[77] K-sampling, in order to make DFT-HSE06 DOS calculation compatible with our available computational efficiency. For DFT+U calculations, we used $U_{eff}$ = 6 eV to the Cu 3d orbital. We chose this value of $U_{eff}$ to be consistent with our previous work.[12] For the defect calculations, we constructed a supercell containing 96 atoms. The k-point sampling for all defect-induced calculations was 5×5×5.

## 5.3 Crystal Structure Prediction

In the present work, the most stable structure was determined from different existing structures through a comprehensive mineral database search by means of an in-house algorithm.[12,212] In addition, StructurePredictor[1,213] software generated structures were considered for the DFT total-energy calculation as well to obtain lowest-energy structures. This method leverages our successful predictions of similar W-based oxides ($AgBiW_2O_8$ and $CuBiW_2O_8$) in our previous work.[12,212] Figure 5.1 shows the evolution of different motif (possible) structures of $CuSnW_2O_8$ (more than 250) from existing structures. Based on the lowest-energy structure, we then determined the electronic properties and stability of CTTO, as well as probable intrinsic defects, which will be discussed in the rest of this chapter.

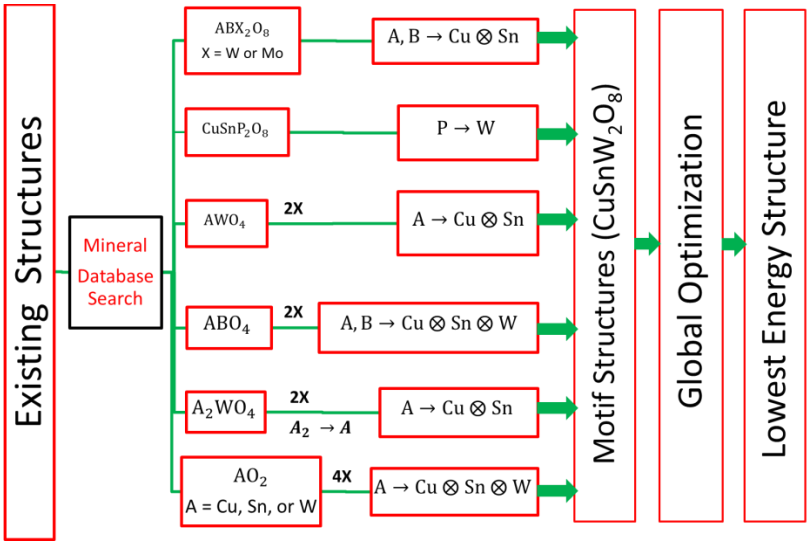


Figure 5.1 Evolution of motif structures from existing structures. “nx” (n=2 and 4) indicates that original structures were doubled and quadrupled to form motif structures. "⊗” corresponds to all possible different arrangements among the cations in a unit cell.

## 5.4 Results

### *5.4.1 Structural Properties*

After optimization of all motif structures, DFT+U determine $NaInW_2O_8$- or $CuBiW_2O_8$- derived structure as the ground state geometry of $CuSnW_2O_8$. The $LeFiW_2O_8$-derived structure could also be a probable one as it has formation energy higher by 0.002 eV per unit formula compared to lowest energy structure (See Table 5.1). Further, all these three motif structures boil down to similar structure for a particular arrangement of Cu and Sn differing merely in per unit formula (Z). The similarities between structures are also reflected in XRDs of them shown in Figure 5.2. Any structures of those can be considered as ground state structure attributing the difference in formation energies as a computational artifact. Since $NaInW_2O_8$ or $CuBiW_2O_8$–derived structure has the lowest Z and exhibits lowest energy in DFT+U case, we keep one them for all our following discussion.

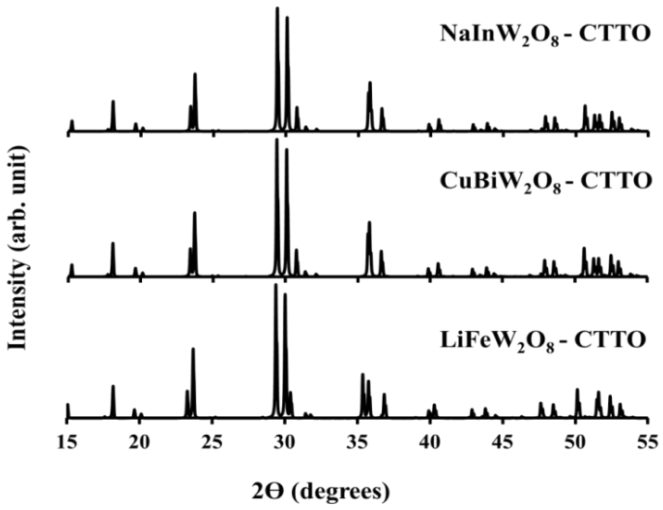


Figure 5.2 Theoretical XRDs of three DFT+U possible structures of $CuSnW_2O_8$.

Table 5.1 DFT+U formation enthalpies ($\Delta H_f$) and volumes of few most probable structures for $CuSnW_2O_8$. The value of $\Delta H_f$ presented here for StructurePredictor (SP) structure is the lowest among all SP generated structures. All $\Delta H_f$ were calculated following the reference.[12]

| | Origin | Unit Cell Formula (Z) | Monkhorst–Pack[77] K-mesh | Formation Enthalpy/Z (eV) | Volume/Z ($Å^3$) |
|---|---|---|---|---|---|
| Existing Structures | $CuBiW_2O_8$[12] | 2 | 7x11x13 | -21.445 | 142.82 |
| | $NaInW_2O_8$ | 2 | 7x11x13 | -21.445 | 142.83 |
| | $LiFeW_2O_8$ | 4 | 9x7x15 | -21.443 | 143.80 |
| | $CuSbM_2O_8$ | 4 | 13x3x11 | -21.349 | 151.96 |
| Structure Predictor | sp1483_crystal35257 | 2 | 7x11x13 | -21.164 | 140.485 |

The following discussion is based on $NaInW_2O_8$-derived structure[214] which was determined as the ground-state geometry of CTTO. It belongs to a monoclinic crystal structure with *a*=9.81 Å, *b*=5.81 Å, *c*=5.01 Å, and $\beta$=91.74° (Z=2), as shown in Figure 5.3. All cations in CTTO form $AO_6$ octahedra; $WO_6$ forms layers along the "*b*" direction leaving an empty space between them, and a similar feature was found for two other octahedra. Each $WO_6$ is connected with $CuO_6$ and $SnO_6$ through corner-sharing oxygen atoms. In addition, these Cu-Sn octahedra form zigzag layers along the "c" direction, and they alternate their positions periodically in a layer along the "a" direction; this alternating trend in a layer requires a unit cell of CTTO to have Z>1.

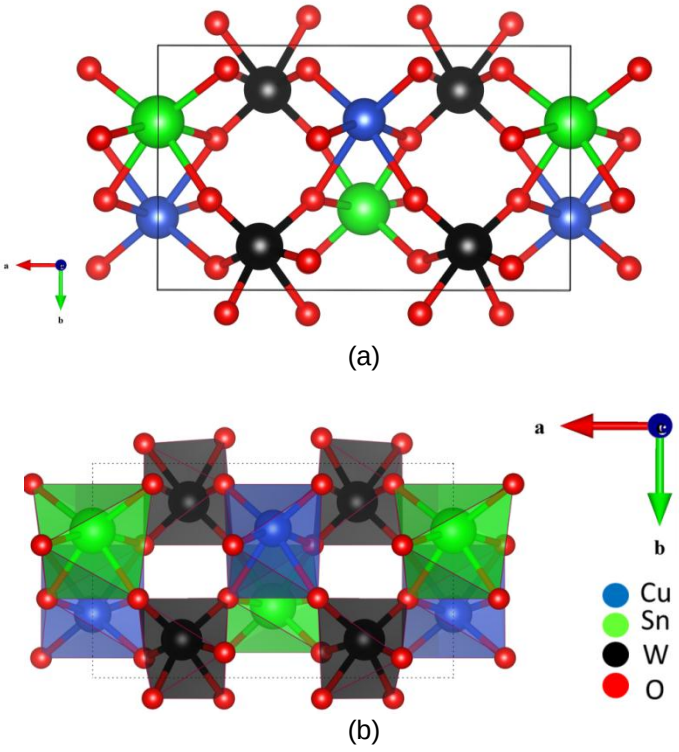


Figure 5.3 Crystal structure of $CuSnW_2O_8$: (top) ball-and-stick model and (bottom) polyhedral model.

*5.4.2. Electronic Properties*

Figure 5.4 shows the HSE06-hybrid electronic band structure and projected density of states (p-DOS) for CTTO. The indirect fundamental band gap (1.25 eV) was found along the $BE_0$ symmetry region, whereas the direct band gap (1.37 eV) occurs at symmetry point B in the Brillouin zone.[215–218] Both of these hybrid-DFT band gap values belong to the optical range for PV applications established by the classic SQ limit. However, it is not necessary that a material satisfy the SQ predicted band gap to be a better PV

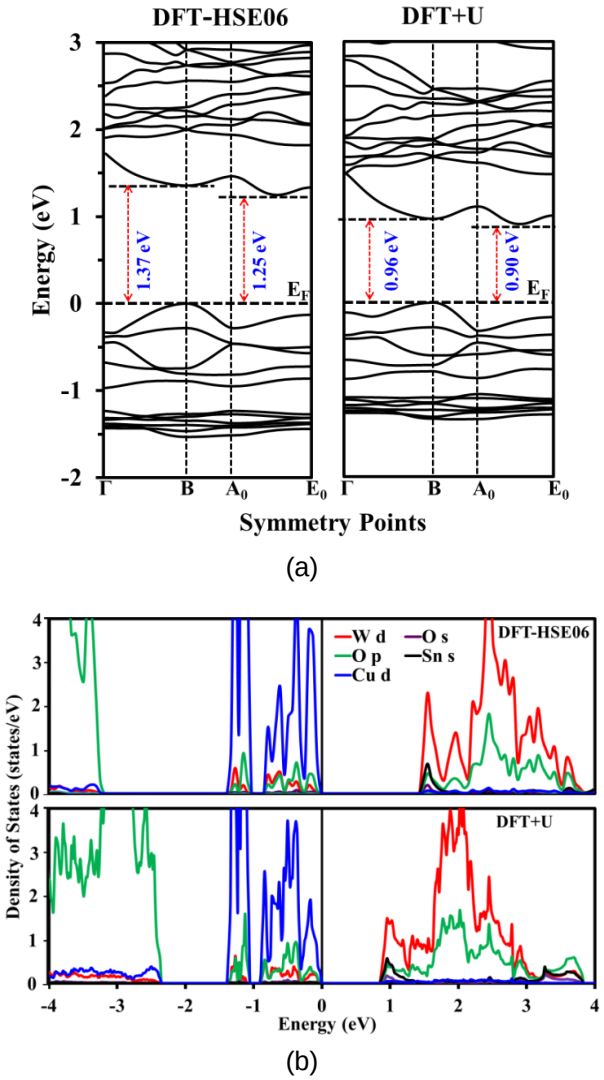


Figure 5.4 The DFT+U and DFT-HSE06: a) electronic band structures and b) projector density of states (p-DOS). The Fermi level was set to 0 eV. The overall features of band structures and p-DOS in both methods were found to be similar except band gaps which can be attributed to the difference in adopted empirical corrections in two different post-DFT methods.

absorber.[219] For instance, SQ limits the band gap to 1.45 eV to exhibit maximum efficiency for a solar-absorbing material whereas highest-efficiency $CuIn_xGa_{1-x}Se_2$ (CIGS) has a bandgap of 1.14 eV.[220] It is noted that, like hybrid-DFT, both DFT and DFT+U schemes produce similar features (not shown) of bandstructures except for smaller band gaps.

In addition to band gap, good PV material must have higher carrier mobility. The conductivity effective mass of holes ($m^*_{h,c}/m_0$), which determines hole mobility, was found to be 0.322, which is lower than that of Si (0.36/0.386),[221] indicating higher hole mobility in CTTO. This can be attributed to contributions from O 2p orbital at the VBM or nearby (see p-DOS in Figure 5.3), having the best correspondence with curve-like features around the valence band edge in the band structure. Like hole mobility, a higher value of electron mobility is also expected because the conduction band edge, as in CZTS, exhibits a parabolic curve-like feature along the BΓ region, indicating lower effective mass of electrons. The Sn 5s orbital, which contributes (see p-DOS in Figure 5.4b) to the parabolic band feature, justifies its selection as a cation in predicting next-generation PV material. Nonetheless, electron mobility comes into play once an electron moves to the conduction band, overcoming the band gap barrier through solar excitation. Contributions of both O 2p and W 5d orbitals at VBM and CBM, respectively, should ensure the favorable p → d electron transition in CTTO upon excitation, promising a higher solar absorption rate than that of CZTS and CIGS. This feature in CTTO is clear when the optical absorption coefficient of those materials are compared side by side in Figure 5.5.

*5.4.3. Optical Absorption*

In Figure 5.5, the DFT+U absorption spectra of CTTO, CZTS, and CIGS were compared; the reason to use rather DFT+U than hybrid-DFT here as a post-DFT

method is explained in sections 5.2. We observed that the light absorption in CTTO and CZTS starts at almost the same time; however, in $CuIn_xGa_{1-x}Se_2$ (CIGS, x=0.5), it occurs quite early. Nevertheless, the steepness of the CTTO absorption spectrum is the highest among all at the onset, attributed to the presence of a W 5d orbital around the conduction band edge. This distinction indicates that CTTO, although it possesses an indirect

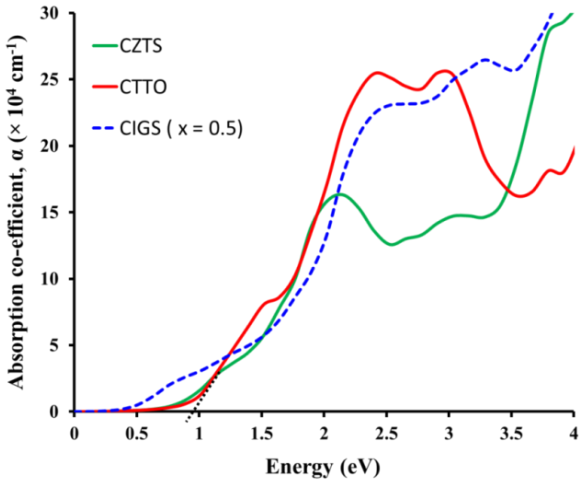


Figure 5.5 DFT+U optical absorption spectrum: red, green, and blue lines represent the absorption of CTTO, CZTS, and CIGS, respectively the used K-meshes for those were 7×13×15, 9×9×5, and 13×13×7, respectively.

fundamental gap, will be a better solar absorber than CIGS and CZTS. The DFT+U optical band gap of CTTO is ~0.97 eV, which corresponds to DFT+U direct band gap of 0.96 eV (see Figure 5.4a). Since DFT+U and DFT-HSE06 band features were found to be similar, DFT-HSE06 photo-onset should also correspond to its direct band gap which would be ~1.37 eV. The fast rise in CTTO absorption spectrum can primarily be attributed to an electronic transition from occupied O 2p states at the top of the valence band to unoccupied W 5d states near the conduction band edge. Like O 2p → W 5d, another favorable Cu 3d → Sn 5s/O 2p could occur because Sn 5s and O 2p states carry

non-negligible weight around the band edges. The results presented here so far based on their electronic and optical properties indicate that CTTO would be superior solar absorber materials to CZTS and CIGS. However, the thermodynamic stability of this newly predicted material needs to be examined.

*5.4.4. Thermodynamic Stability*

5.4.4.1. Bonding Rigidity and Stability against Phase Segregation

One of the first indicators of material stability is to determine its cohesive energy calculated with respect to the infinitely separated atomic limit: the lower its value, the stronger the bonding between the atoms of that material. The cohesive energy per atom of CTTO was found to be -5.94 eV with the DFT+U scheme, which is significantly smaller than that of CZTS (DFT+U: -4.11 eV) and comparable to highly stable $WO_3$ (DFT: -6.77 eV). Hence, binding between atoms in CTTO would be stronger than that in CZTS, and this rigidity in atomic binding is comparable to $WO_3$, which justifies the selection of W oxide as a PV material.

Another manifestation of the material's stability is the negative fragmentation energies with respect to competitive binary and/or ternary oxides.[12] This determines the material's averseness to being decomposed into different competitive secondary phases: the lower its value, the higher the withstanding capability and the more robust the stability of that material. The pathways with fragmentation energies for CTTO are presented below:

$CuSnW_2O_8 = SnO + CuO + 2WO_3$; $\Delta H_{frag.,CTTO} = -0.05$ eV (5.1)

$3CuSnW_2O_8 = Cu_2O + 3SnO + CuWO_4 + 5WO_3 + 1/2O_2$; $\Delta H_{frag.,CTTO} = -1.46$ eV (5.2)

$3CuSnW_2O_8 = Cu_2O + CuO + 3SnO + 6WO_3 + 1/2O_2$; $\Delta H_{frag.,CTTO} = -1.57$ (5.3)

eV

$2CuSnW_2O_8 = Cu_2WO_4 + 3WO_3 + 2SnO + 1/2O_2$; $\Delta H_{frag.,CTTO} = -2.68$ eV (5.4)

$3CuSnW_2O_8 = CuO + 3SnO + Cu_2WO_4 + 5WO_3 + 1/2O_2$ ; $\Delta H_{frag.,CTTO} = -2.69$ eV (5.5)

The negative fragmentation energies in different pathways indicate that CTTO will be stable enough to withstand different fragmentation processes. Compared to fragmentation energies of CZTS (see Ref.[160]), CTTO will have greater stability than CZTS but also be a robust material.

5.4.4.2. Single-Phase Stability

The single-phase stability, which determines the probability of forming the material in question as a single phase or multi-phases (e.g. CTTO + secondary phases), can be mapped through chemical potential landscape analysis. Figure 5.6 portrays chemical potential landscapes of CTTO at two different growth conditions. Each chemical potential landscape, satisfying equation (5.6), represents a set of growth conditions at which the stable formation of CTTO is possible at thermodynamic equilibrium.

$$\Delta\mu_{Cu} + \Delta\mu_{Sn} + 2\Delta\mu_W + 8\Delta\mu_O = \Delta H_{f,CTTO} = -21.445 \text{ eV} \quad (5.6)$$

The upper and lower bounds of chemical potentials satisfying equation (6.1) for each atomic species are

$$-21.445 \text{ eV} \le \Delta\mu_{Cu} \le 0 \text{ eV} \quad (5.7a)$$
$$-21.445 \text{ eV} \le \Delta\mu_{Sn} \le 0 \text{ eV} \quad (5.7b)$$
$$-10.723 \text{ eV} \le \Delta\mu_W \le 0 \text{ eV} \quad (5.7c)$$
$$-2.681 \text{ eV} \le \Delta\mu_O \le 0 \quad (5.7d)$$

The set of growth conditions in equations (5.7) could facilitate the formation of secondary phases as well. To avoid the occurrence of secondary phases at thermodynamic equilibrium,

| | | |
|---|---|---|
| α-$SnWO_4$: | $\Delta\mu_{Sn} + \Delta\mu_W + 4\Delta\mu_O < \Delta H_{f,SnWO_4}$ = -11.506 eV | (5.8a) |
| $CuWO_4$: | $\Delta\mu_{Cu} + \Delta\mu_W + 4\Delta\mu_O < \Delta H_{f,Cu_2WO_4}$ = -10.203 eV | (5.8b) |
| $Cu_2WO_4$: | $2\Delta\mu_{Cu} + \Delta\mu_W + 4\Delta\mu_O < \Delta H_{f,Cu_2WO_4}$ = -9.03 eV | (5.8c) |
| $WO_3$: | $\Delta\mu_W + 3\Delta\mu_O < \Delta H_{f,WO_3}$ = -8.560 eV | (5.8d) |
| SnO: | $\Delta\mu_{Sn} + \Delta\mu_S < \Delta H_{f,SnO}$ = -2.762 eV | (5.8e) |
| $SnO_2$: | $\Delta\mu_{Sn} + 2\Delta\mu_S < \Delta H_{f,SnO_2}$ = -5.179 eV | (5.8f) |
| CuO: | $\Delta\mu_{Cu} + \Delta\mu_S < \Delta H_{f,Cu_2O}$ = -1.527 eV | (5.8g) |
| $Cu_2O$: | $2\Delta\mu_{Cu} + \Delta\mu_S < \Delta H_{f,Cu_2O}$ = -1.595 eV | (5.8h) |

Each line, $L_i$ (i = 1, 2, .., 8), across the chemical potential triangles shown in Figure 5.6, satisfying equation (5.8), represents a boundary of a secondary phase that may coexist during the synthesis process. The co-existence of a secondary phase is evident in one of two regions, divided by a line $L_i$, which does not satisfy corresponding equation. The only exception of previous statement is to α-$SnWO_4$ presenting line ($L_1$). Neither side of the line except points on it corresponds to growth condition suitable for the formation of α-$SnWO_4$. This can be attributed to the fact that two equations will be solvable if and only if the RHS of the following equations equal to each other

| | | |
|---|---|---|
| α-$SnWO_4$: | $\Delta\mu_W + 4\Delta\mu_O = \Delta H_{f,SnWO_4} - \Delta\mu_{Sn}$ | (5.9a) |
| $CuSnW_2O_8$: | $\Delta\mu_W + 4\Delta\mu_O = (\Delta H_{f,CTTO} - \Delta\mu_{Sn} - \Delta\mu_{Cu})/2$ | (5.9b) |

Which yields,

$$\Delta\mu_{Sn} = (2*\Delta H_{f,SnWO_4} - \Delta H_{f,CTTO} + \Delta\mu_{Cu}) \quad (5.9c)$$

Equations (5.9c) generates a set of Cu and Sn growth conditions $\{\Delta\mu_{Cu}, \Delta\mu_{Sn}\}$ which have one to one correspondence. As a result, only a point of $\Delta\mu_{Sn}$ rather than distribution satisfies equations (5.9a) and (5.9b) simultaneously on each Cu-plane or plane of a

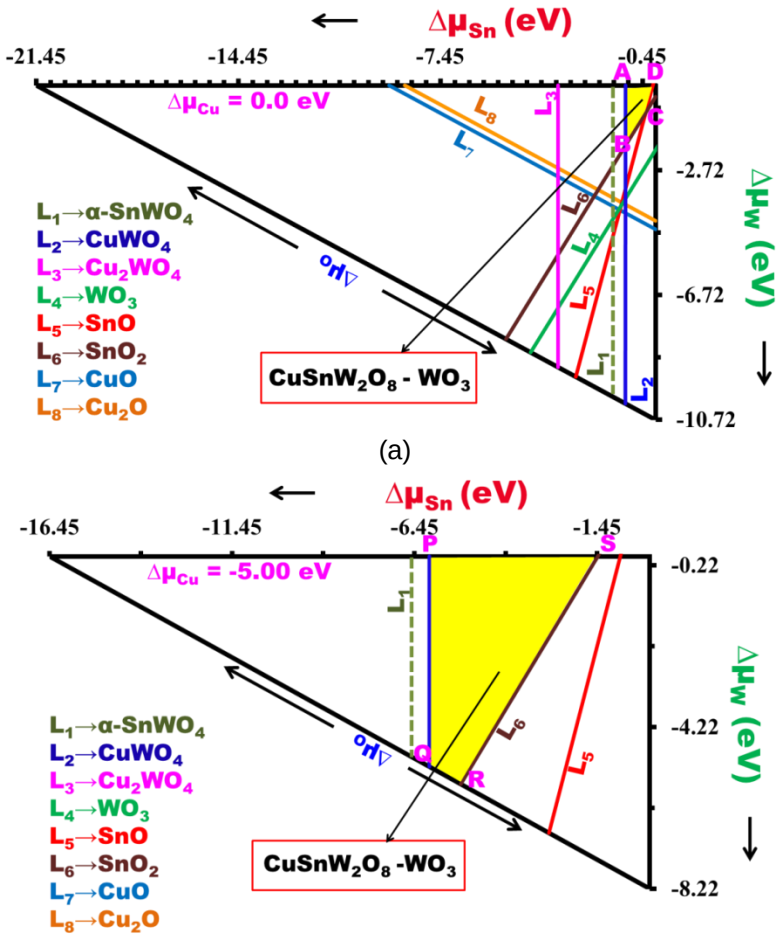


Figure 5.6 Chemical potential landscape of CTTO in two different Cu growth conditions: (a) Cu-rich and (b) Cu-poor. Yellow-bounded regions represent the range of growth conditions of all chemical species to form CTTO-$WO_3$, as well as the stability of this mixed phase: the larger the spread, the higher the stability.

triangle in Figure 5.6. This constraint limits α-$SnWO_4$ phase to be co-existed on either side of the line presenting it in CTTO chemical potential landscape.

Any region bounded by different lines $L_i$ in Figure 5.6 that satisfies the above equations simultaneously corresponds to single phase of CTTO. No such region in Figure

5.6 was found, implying the fact that formation of single phase CTTO would be highly unlikely during the growth process like any other multi-cations compounds; however, minimization of co-existence of unwanted secondary phases would not be a harder task. For example, the synthesis of $CuSnW_2O_8$-$WO_3$ multi-phases can be preferable since both have monoclinic structures and hence, are likely to introduce least lattice mismatch i.e., recombination velocity at heterojuction interface. The formation of those multi-phases are possible at flexible growth conditions (see yellow bounded regions ABCD and PQRS in Figures 5.6a and 5.6b, respectively) of all chemical species (Cu, Sn, W, and O). Moreover, the larger spreads of yellow bounded regions in Figure 5.6, especially in Cu-poor growth conditions implies higher stability of those multi-phases even with a wide variation of growth conditions.

*5.4.5. Defects*

The frequent formation of Cu-vacancy ($V_{Cu}$) in Cu based compounds is expected. The lower formation energy ($\Delta H$ ($V_{Cu}$) = 0.233 eV at $\Delta\mu_{Cu}$ = 0) (see Figure 5.7 for Cu-rich condition) tells that $V_{Cu}$ is indeed highly probable defect in CTTO, even at Cu-rich growth condition; $V_{Cu}$ becomes spontaneous at $\Delta\mu_{Cu}$ = -0.233 eV. In fact, different intrinsic defects in CTTO are probable at certain conditions like in any other multi-cations compounds. However, apart from Cu-vacancy, we present here only two other defects, $Sn_{Cu}$ and $Sn_{Cu}$ + $V_{Cu}$ , which are relevant for our following discussion. The details of defects calculation will be presented somewhere else.

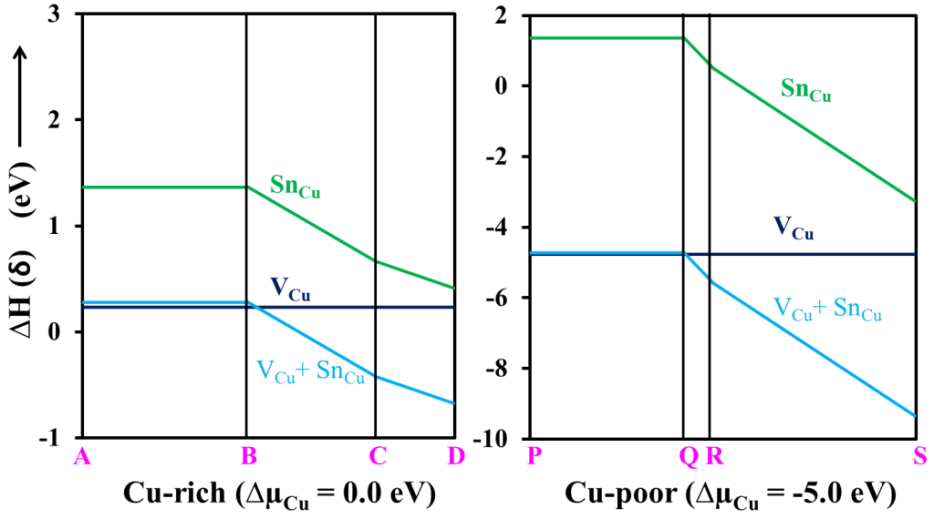


Figure 5.7 The DFT+U defects formation energy in CTTO at two different growth conditions: Cu-rich and Cu-poor.

5.4.5.1 p-type activity

One of the factors, which determines the higher PV efficiency is p-type conductivity. Typically, the frequent formation of Cu-vacancy ($V_{Cu}$) in Cu based compounds make them p-type semiconductor i.e., better PV materials e.g. $Cu_2S$, CZTS, CIGS etc. Hence, like other Cu-based PV materials, p-type activity through facile formation of $V_{Cu}$ is also expected in CTTO. Unoccupied hole states the top of VB (along Γ-Z and at Y in spin up channel; and along Γ-Z, C-

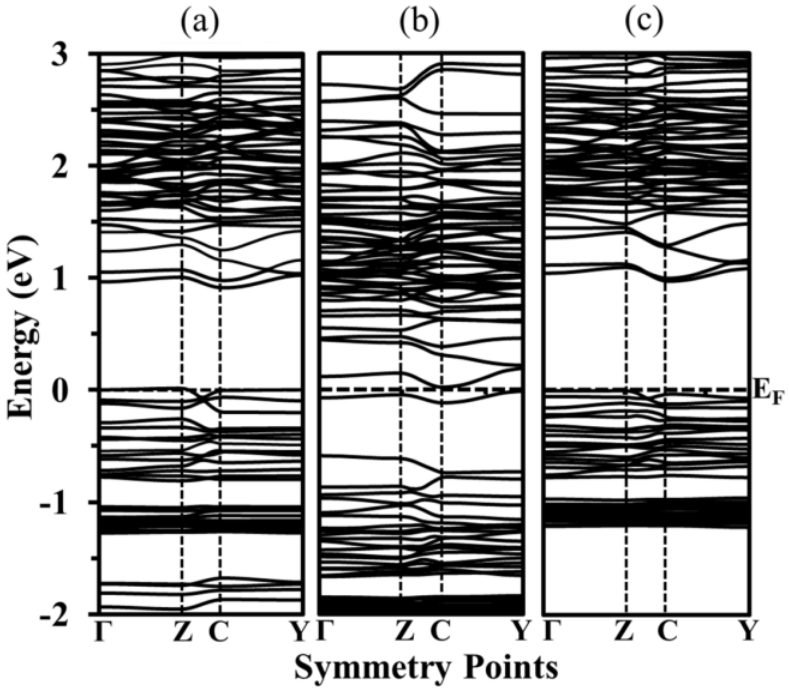


Figure 5.8 Band structures of three defects: (a) $V_{Cu}$, (b) $Sn_{Cu}$, and (c) $Sn_{Cu}$+$V_{Cu}$-induced CTTO.

Y in spin down channel), in Figure 5.8 confirms that a single $V_{Cu}$ defect induces p-type activity in CTTO. The degree of p-type activities can be determined from $V_{Cu}$ concentration at equilibrium. The equilibrium $V_{Cu}$ concentration in CZTS and CTTO are $3x10^{3}$ $cm^{-3}$ and $1x10^{16}$ $cm^{-3}$, respectively at 298 K temperature and at Cu-rich ($\Delta\mu_{Cu} = 0$) growth condition. The $10^{13}$ times higher concentration of $V_{Cu}$ in CTTO clearly indicates that it will have more enhanced p-type activity than that of CZTS. As $\Delta\mu_{Cu}$ decreases, $V_{Cu}$ concentration also increases. However, $Sn_{Cu}$ defect could be spontaneous at Cu-poor/Sn-rich growth conditions that introduces n-type activity (see unoccupied bands around the VB edge in Figure 5.8b). When these two different defects are formed simultaneously as $Sn_{Cu}$ + $V_{Cu}$ pair, both p-type and n-type conductivity counterbalances each other, leaving CTTO a neutral type PV material; no more hole or unoccupied states

around VB edge in figure 5.8c. Only way to have the p-type attribute in CTTO is to bar the formation of $Sn_{Cu}$ defects. This can be done by limiting growth conditions to any Cu-rich/Sn-poor values or between A and B (see figures 5.6a and 5.7) if one prefers only $WO_3$ to be co-existed with it.

5.4.5.2 Optical absorption with defects induced CTTO

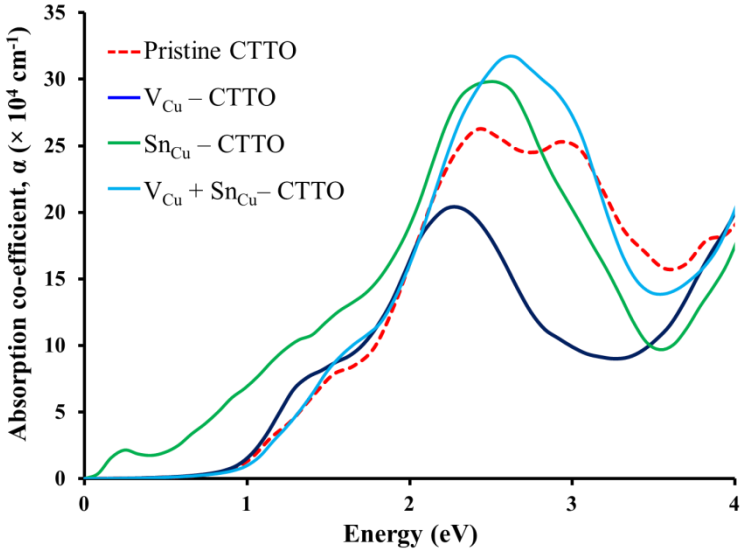


Figure 5.9 The DFT+U optical absorption spectra of pristine and defect-induced CTTO. It is seen that the absorption spectra of pristine and defects-induced CTTO have similar features except the very early absorption in $Sn_{Cu}$-CTTO. The first two early rises in the $Sn_{Cu}$ absorption spectrum correspond to the transition between occupied and unoccupied states around the conduction band edge, which do not contribute to PV efficiency. A 7×11×13 K- point sampling was used to produce the absorption spectrum of pristine CTTO, while it was 5×5×5 for those of defect-induced CTTO.

Figure 5.9 represents a comparison between optical absorption spectra of pristine and different defects induced CTTO. It is quite obvious from the figure that defects in CTTO do not deteriorate absorption rate compared to pristine counterpart. In fact, $V_{Cu}$ and $Sn_{Cu}$ enhance absorptions rate in CTTO. However, $Sn_{Cu}$ is itself not as probable defect as $V_{Cu}$. Moreover, the first two rises in $Sn_{Cu}$ absorption spectrum correspond to transition between occupied sates in

VB and unoccupied states around VB edge, which do not contribute PV efficiency. Furthermore, the third rise of that spectrum which contributes to PV efficiency requires more energy than other defects at onset. In contrast, absorption rate of highly probable $Sn_{Cu}$ + $V_{Cu}$ defect induced CTTO remains similar to pristine counterpart upto ~2.1 eV and increases afterwards. This tells that if CTTO even can't be synthesized as p-type material, the absorption rate will still be superior to that of CZTS and CIGS (see figures 5.5 and 5.9).

## 5.5. Conclusion

In summary, we present a new quaternary oxide, CTTO that is suitable for affordable PV application. This material was found to possess a $NaInW_2O_8$-derived monoclinic ground-state structure determined by a comprehensive mineral database search in conjunction with DFT total-energy calculations. This structure exhibits an indirect fundamental band gap of 1.25 eV with the HSE06-DFT scheme. The mobility of holes was greater than that of Si. The DOS calculations confirm that the combined effects of Cu 3d and Sn 5s at VBM and CBM, respectively, as in CZTS, significantly reduced the band gap compared to that of $WO_3$. Moreover, the optical absorption rate of CTTO was higher than that of CZTS and CIGS (x=0.5) at onset. This material displays higher stability and can be synthesized at flexible experimentally convenient growth conditions,

although the co-existence of at least one secondary phase is likely. Like any other Cu-based oxide, Cu vacancy is highly probable at any Cu growth condition, making this material a p-type semiconductor. In fact, the population of this vacancy is significantly higher than that of CZTS at room temperature. Based on the previously mentioned electronic properties and stability features, we conclude that CTTO, if synthesized, could be an excellent alternative to current commercialized PV materials.

# Chapter 6

## New PEC Material ($ZnSnW_2O_8$)

### 6.1 Introduction

In Chapter 1 the need to predict an affordable photocatalysts was demonstrated. Further, it was explained the reasons behind in designing a solar absorber new material in the form of $ABW_2O_8$. We have chosen Zn and Sn as our A and B cations, respectively for predicting a photocatalysts,. The reasons are i) both Zn and Sn are non-toxic and abundant on earth-crust, ii) Sn 5s has higher energy than O 2p, thereby expecting band gap reduction, as in α-$SnWO_4$, and iii) the presence of Zn 3d at lower energy, as in $ZnWO_4$,[6] would push VBM and CBM upward further, placing the conduction band edge above $H_2/H^+$ redox potentials. Note that, from $CuSnW_2O_8$ (see Figure 5.4b) and CZTS, the presence of Cu 3d and Sn 5s at VBM and CBM, respectively potentially reduces band gap in those compounds; such a lower band gap is needed for PV application, however, in practice, a relatively larger band gap ($2eV < E_g < 2.4$ eV) is essential for an efficient solar-to-hydrogen conversion process. For this reason, we didn't select two cations which would have had simultaneous role in band gap reduction, resulting a lower band gap material like CTTO and CZTS. Rather, we have selectively chosen two cations so that two would satisfy two different purposes, one (Sn) for band gap reduction while the other one (Zn) for pushing the band edges upward sufficiently. Note that the addition of only Sn to $WO_3$ results a satisfactory band gap reduction in α-$SnWO_4$, while the presence of Zn 3d lifts the conduction band edge in $ZnWO_4$ above $H_2/H^+$ redox potentials.

### 6.2 Computational Details

In addition to DFT, DFT+U[39,43,58] and Hybrid functional (HSE06[133]) (μ=0.2, α=0.25 $EXC_{HF}$) were also employed to overcome the shortcoming of DFT—i.e., the underestimation of electron localization for systems with localized $d$ and $f$ electrons.[58–60] DFT-HSE06 was

employed to calculate electronic band structure and density-of-states (DOS) calculations of the pristine unit cell. However, DFT+U was used for optical absorption calculation of pristine $ZnSnW_2O_8$. The reason for that has been explained in Section. The energy was converged up to four decimal places at 9x5x19 k-mesh, and the converged unit cell was later used for all HSE06 calculations. However, smaller 5×3×5 K-sampling was used in order to make DFT-HSE06 DOS calculation compatible with our available computational efficiency. For DFT+U calculations, we used $U_{eff}$ = 6 eV to the Cu 3d orbital. We chose this value of $U_{eff}$ to be consistent with our previous work.[12] For the defect calculations, we constructed a supercell containing 96 atoms. The k-point sampling for all defect-induced calculations was 3×3×3.

## 6.3 Crystal Structure Prediction

Once the new material is designed, the success in predicting the opto-electronic properties and stability feats depends on the precise crystal structure prediction. To accomplish this task quite successfully, we employed our crystal structure prediction method to $ZnSnW_2O_8$. Our method predicts the α-$SnWO_4$- derived crystal structure as the most probable structure of $ZnSnW_2O_8$. Therefore, our following discussions would be based on this structure.

## 6.4 Results

### *6.4.1 Structural Properties*

The crystal structure of belongs monoclinic symmetry (P 2/c; S.G. 13; Z=2) with a = 5.678 Å, b =11.785 Å, c = 5.180 Å, and γ = 84.11°. Like other tungstates, W forms $WO_6$ octahedra while Zn and Sn form $ZnO_4$ and $SnO_4$ (as in SnO) tetrahedra, respectively as shown in Figure 6.1a. $WO_6$, being connected with each other through corner sharing O,

forms a zigzag network along ‘c’ axis (see Figure 6.1b). Between each two layers of $WO_6$, $ZnO_4$ and $SnO_4$ are alternatively inserted, extending along ‘b’axis. Each $AO_4$ (A = Zn and Sn) is connected with a similar tetrahedra only along ‘a’ axis through edge sharing O and leaves a huge void between them in ‘c’ direction see (Figure 6.2a). However, these two tetrahedral do not make a direct network between them in any directions.

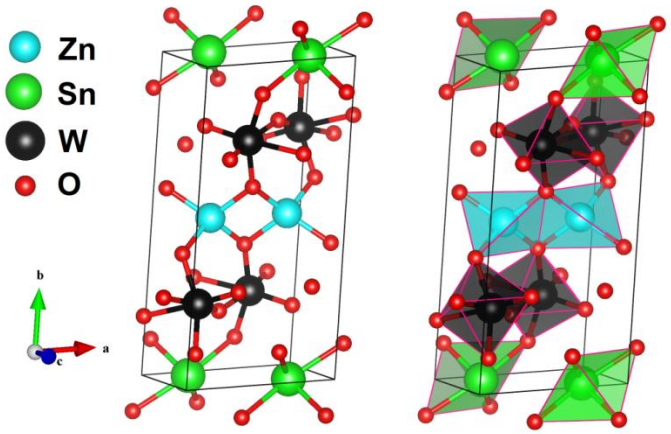


(a)

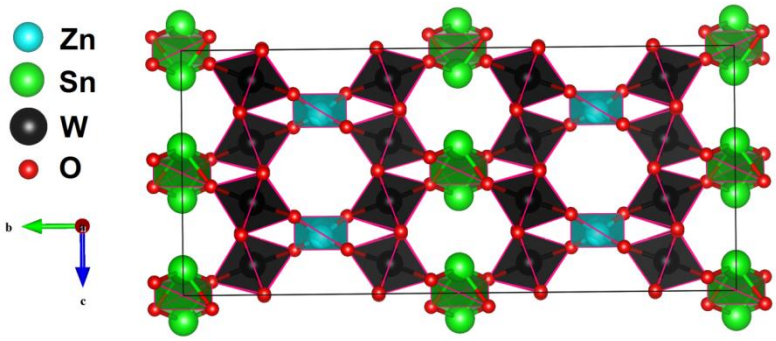


(b)

Figure 6.1 The DFT+U optimized crystal structure of $ZnSnW_2O_8$. Figure a represents two different models of the unit cell of 24 atoms: (left) ball-and-stick and (right) polyhedra. A 2x1x2 supercell of 96 atoms in the polyhedra model is shown in figure b, which contains hollows in the long-ranged periodicity.

*6.4.2 Electronic Properties*

The electronic band structure and projected density of states (p-DOS) of pristine-$ZnSnW_2O_8$ are presented in Figure 6.2. It possesses almost a direct band gap of 2.34 eV (DFT-HSE06) and 1.66 eV (DFT+U), which occurs along C-Z-D region in the Brillouin zone. Both post-DFT methods produce similar band feats except the difference in band gaps. The band gap values are within the range of PEC requirement for efficient hydrogen evolution. The reduction of band gap compared to its binary parent compound ($WO_3$) is the presence of Sn 5s at VBM (see Figure 6.2b). This justifies our choice of Sn in band gap reduction. Despite the significant presence of Sn 5s, VBM is mostly O 2p contributed which is due to strong hybridization between Sn and O. The contributions of Zn 3d are seen only at lower energies as in $ZnWO_4$ and hence Zn does not play role in band gap reduction. However, lower energy Zn 3d should provide an uplift of conduction band which will be investigated in Section 6.3.4. In the case of conduction band region, like other tungstates, CBM is primarily W 5d contributed and degenerated as in α-$SnWO_4$. Conduction bands are mostly dispersive, a good indication of higher electron mobility.

*6.4.3 Optical Absorption*

Figure 6.3 demonstrates the DFT+U optical absorption spectrum of pristine-$ZnSnW_2O_8$. Like other tungstates, a strong absorption is observed, which validates our selection of W-based compound as a suitable solar absorber material. The optical band gap was found to be ~1.70 eV which corresponds to its electronic counterpart (see Figure 6.2a).The photo-onset can be attributed to electron transition from occupied O 2p to unoccupied W 5d orbitals. Since Sn 5s has a strong presence at VBM (see Figure 6.2b), next absorption could be due to transition s→d/p.

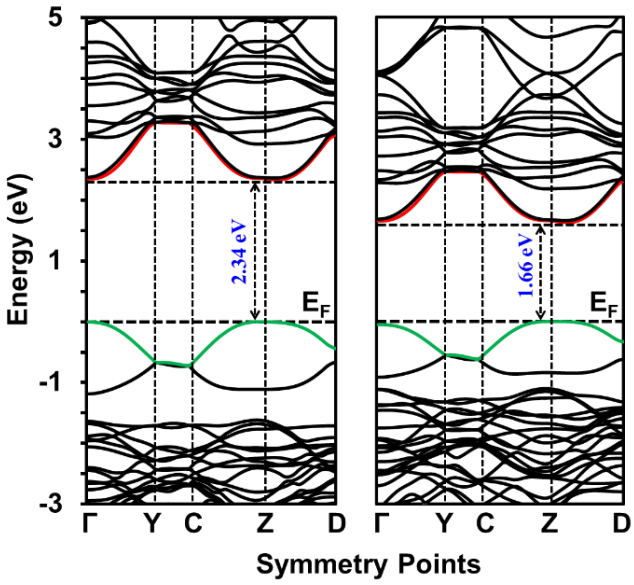


(a)

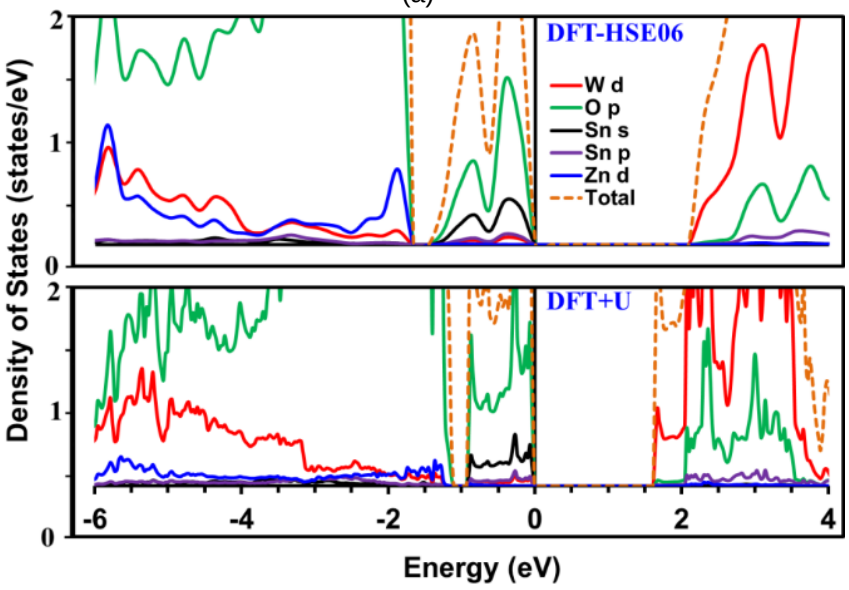


(b)

Figure 6.2 The DFT+U and DFT-HSE06: a) electronic band structures and b) projector density of states (p-DOS). The Fermi level was set to 0 eV. The overall features of band structures and p-DOS in both methods were found to be similar except band gaps which can be attributed to the difference in adopted empirical corrections in two different post-DFT methods.

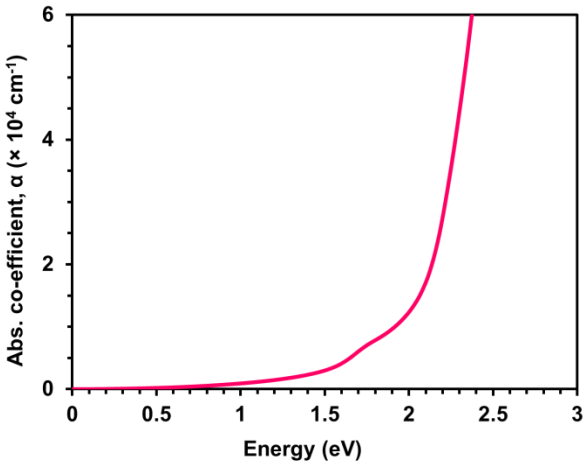


Figure 6.3 The DFT+U optical absorption spectrum of pristine-$ZnSnW_2O_8$.

*6.4.4 Band Edge Positions*

Since the band edges of a semiconductor must be positioned at right energies for hydrogen evolution through water splitting, their positions need to be checked before predicting the designed material as a suitable photocatalyst. To do this, as in Figure 6.4(left), we have compared the VBM/CBM position of $ZnSnW_2O_8$ with respect to those of Zn/Sn-tungstates and $WO_3$. The VB heights were calculated taking the relative energy difference between O 1s and VBM of the corresponding phases. On other hand, CBMs were positioned using $E_{CBM} = E_{VBM} + E_g$; where $E_g$ is the experimental/DFT-HSE06 band gaps for the existing/predicted materials. The depicted vertical heights of the VBs of $ZnSnW_2O_8$ and Zn/Sn-tungstates in Figure 6.4 were normalized to $WO_3$ counterpart. Therefore, Figure 6.4(left) visualizes the relative positions of the band edges of the considered compounds with respect to each other.

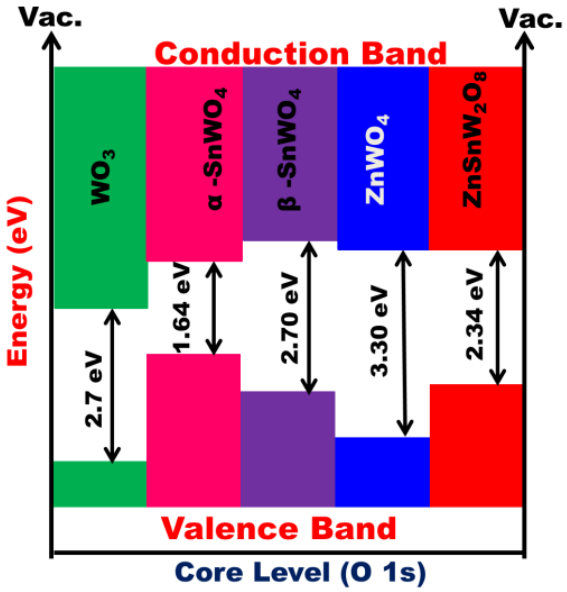


Figure 6.4 The relative band edges positions of $ZnSnW_2O_8$ and different metal-tungstates with respect to $WO_3$.

The reasons behind the approach mentioned above were (i) O is the common element in the considered compounds and (ii) O 1s lies very deep in the cores and is expected not be hybridized with other orbitals. As a result, it would not be very unrealistic considering O 1s as a reference level to determine the relative position of VBM. Note that a precise description of the band edges position may not be possible through this simplistic approach; however, a quick estimation on the relative band edge positions can be made which should be good enough in predicting a photocatalyst in time- and cost-effective manner.

In Figure 6.4(left), the CBMs of both $ZnWO_4$ and $ZnSnW_2O_8$ are positioned at the same height. Therefore, it is also expected that like $ZnWO_4$, the CB edge of $ZnSnW_2O_8$ would straddle $H_2/H^+$ redox potential as well. The relative higher positions of CBMs in those compounds with respect to that of $WO_3$ can be attributed to the upward push generated by Zn 3d. This justifies the selection Zn 3d in designing new semiconductor for

efficient hydrogen evolution process. Note that the VBM of $ZnSnW_2O_8$ has a higher position that that of $WO_3$/ $ZnSnW_2O_8$. It is due to the presence of Sn in our predicted material, causing a band gap reduction compared to $WO_3$/ $ZnSnW_2O_8$. See Reference for a comparison between experimentally measured band edges of $WO_3$, β-$SnWO_4$ and $ZnWO_4$ with respect to $O_2$ and $H_2/H_+$ redox potentials was presented on the right of Figure 6.4

*6.4.5 Stability*

6.4.5.1. Bonding Rigidity and Stability against Phase Segregation

As a first test of the predicted material's stability we determine its cohesive energy calculated with respect to the infinitely separated atomic limit; because the lower its value, the stronger the bonding between the atoms of that material. The cohesive energy per atom of $ZnSnW_2O_8$ was found to be -5.94 eV with the DFT, which is comparable to highly stable $WO_3$ (DFT: -6.77 eV). Hence, binding between atoms in $ZnSnW_2O_8$ would be stronger than that in CZTS, and this rigidity in atomic binding is comparable to $WO_3$, which justifies the selection of W oxide as a photocatalyst.

The stability of $ZnSnW_2O_8$ against phase segregation can be gauged form the negative fragmentation energy with respect to competitive binary and/or ternary oxides.[12] This determines the material's averseness to being decomposed into different competitive secondary phases: the lower its value, the higher the withstanding capability and the more robust the stability of that material. One pathway that possesses negative fragmentation energy for $ZnSnW_2O_8$ is presented below:

$$ZnSnW_2O_8 = SnO + ZnO + 2WO_3; \qquad \Delta H_{frag,ZnSnW2O8.} = -0.08 \text{ eV} \qquad (6.1)$$

The negative fragmentation energy in the above pathway indicates that $ZnSnW_2O_8$ will be stable enough to withstand at least one fragmentation processes. Since the above pathway results negative $\Delta H_{frag}$, the binary phases can be used as precursors to form stable $ZnSnW_2O_8$.

6.4.5.2. Single-phase Stability and Effective Growth Conditions

To determine the single-phase stability of $ZnSnW_2O_8$ the chemical potential landscape analysis (CPLA) was employed. The details of CPLA have been discussed at a length in Section 2.4.4. The triangles in Figure 6.5 are the CPL of $ZnSnW_2O_8$ drawn at two different set of chemical potentials ($\Delta\mu_\alpha$, α = Zn, Sn, W, and O) which represent the growth of conditions of a species α. The triangles further satisfy the following growth condition (Equation (6.2)) required to form stable $ZnSnW_2O_8$ at thermodynamic equilibrium. Within this condition may be formed as a single phase or multi-phases compound. To avoid the presence of secondary phases, the growth conditions ($\Delta\mu_\alpha$) within the triangles should be chosen such way that would prohibit the formation of secondary phases. However, not a single set of $\Delta\mu_\alpha$ in the following triangles can be set for that. This means that the formation of multi-phases $ZnSnW_2O_8$ (at least two secondary phases co-exist) would be highly probable. The role of those secondary phases on photocatalytic performance of $ZnSnW_2O_8$ needs to be investigated, which will be done in future works.

$$\Delta\mu_{Cu} + \Delta\mu_{Sn} + 2\Delta\mu_W + 8\Delta\mu_O = \Delta H_{f,CTTO} = -21.445 \text{ eV} \quad (6.2)$$

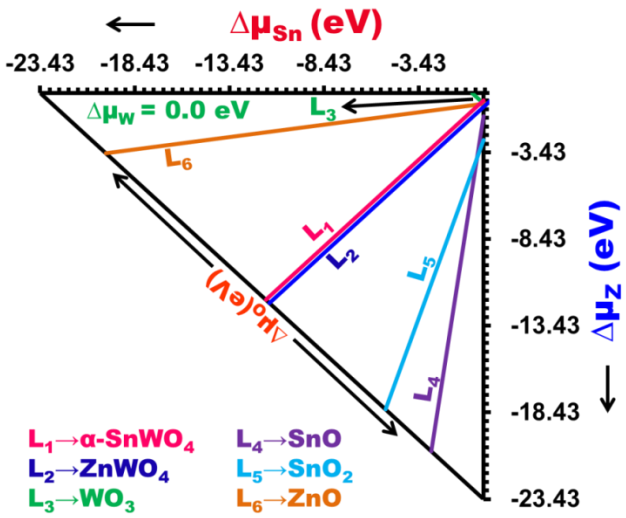


(a)

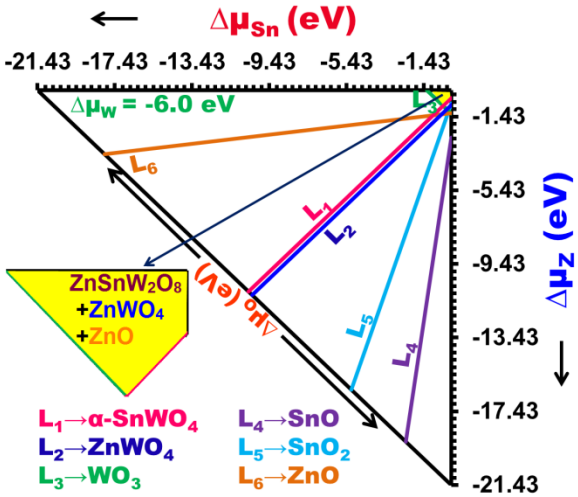


(b)

Figure 6.5 Chemical potential landscape of $ZnSnW_2O_8$ in two different W growth conditions: (a) W-rich and (b) W-poor. Yellow-bounded region represents a growth region which can be suitable for synthesizing $ZnSnW_2O_8$ with least detrimental defects. However, $ZnWO_4$ and ZnO are highly probable to be co-existed with the primary phase in this region.

Not only can the single-phase stability of a material be predicted from CPLA, but also an effective growth conditions, with the help of defect calculation, for that material can be deduced. An attempt was made for $ZnSnW_2O_8$ in this regard. An effective growth conditions should be one that would minimize unwanted defects or secondary phase. Since the role of those secondary phases in $ZnSnW_2O_8$ is not investigated yet, we would focus only on defects which may be harmful for photocatalytic performance. In this case, we consider those defects which are responsible for poor performance in existing parent compounds. One such a defect is $Sn_W$ which lowers photocatalytic activity in α-$SnWO_4$. Since the similar defect may also be present in $ZnSnW_2O_8$, we need to employ a set of growth conditions that would prohibit the formation of that defect. Such a growth conditions be the yellow region in which $Sn_W$ has formation energy of > 2.6 eV. In this growth region, all the cationic defects are also least probable; however, the formation of two other single defects $V_o$ and $W_{Sn}$ are probable, which give rise to n-type activity in $ZnSnW_2O_8$. In such a growth region, the probable co-existing secondary phases would be ZnO and $ZnWO_4$.

## 6.5 Conclusion

A new semiconductor $ZnSnW_2O_8$ was predicted based on materials design. Sn and Zn were here to modify the electronic properties of $WO_3$ while adding with it; two different cations were selected for two different reasons, one (Sn) reduce to band gap while other one (Zn) to place conduction band edge above $H_2/H^+$ potentials through an upward push. Our DFT derived results show that Sn and Zn indeed play their roles in $ZnSnW_2O_8$. It possess an almost direct band gap of 1.66 eV (2.34 eV) in DFT+U (DFT-HSE06). Further, like other tungstates, it exhibits a strong absorption. The bonding rigidity was also found be comparable with $WO_3$. As a result, this new material shows an intense

promise for PEC process. However, the chemical potential landscape analysis reveals that the formation of multi-phases-$ZnSnW_2O_8$ is highly possible. Note that all opto-electroic properties and stability were determined with respect to a crystal structure that was predicted through comprehensive mineral data base search by means of DFT+U global optimization.

# Chapter 7

## Conclusion

In the dissertation work, a systematic method to predict new functional materials has been developed. The method includes rational materials design and crystal structure predicting; prediction of single-phase stability and optimized solar-to-current/fuel efficiency growth conditions, in conjunction with opto-electronic properties calculations using DFT and post-DFT methods. Among all, the method to predict single-phase stability in the presence of a single defect as well as the optimized growth conditions has been developed for the first time. An extended and more generalized version of existing approach to predict crystal structure was presented. In addition, it was shown that a rational material design can accelerate the discovery of the desired material. The successful examples of the method are the predictions of two new quaternary oxides, $CuSnW_2O_8$ and $ZnSnW_2O_8$, respectively for PV and PEC applications; these successes are extensible to any other applications as well.

The first critical step in our method was to designing a new material. To accomplish this task successfully for PV and PEC processes, oxides are chosen as new materials because of their well-known stability. The cations Cu, Sn, Zn, and W were selected considering their orbitals' contributions in different compounds, mainly oxides. W-oxides were chosen because of proven demonstration of higher stability and strong absorption in its binary form ($WO_3$). The reason to add Cu and Sn to $WO_3$ to form $CuSnW_2O_8$ was to reduce the band gap significantly as in CZTS; dispersive conduction band feats were also expected from Sn. In case of $ZnSnW_2O_8$, Sn was selected to have contributions at VBM, expecting a band gap reduction as in α-$SnWO_4$ while Zn was chosen to provide an upward push, as in like $ZnWO_4$, placing the conduction band edge above $H_2/H^+$ redox potentials. Our DFT-derived results show that the expected feats were

indeed exhibited by the predicted materials. This concludes that if material is designed wisely based on quantum mechanical description, finding a suitable material in near future would no longer seem a distant hope.

The next critical step was to predict crystal structure precisely. Since there is no method that can predict the crystal structure with certainty, our research was mostly devoted to make the crystal structure prediction as precise as possible. In doing so, we initially predicted crystal structures of existing W-O materials of similar stoichiometry. This was done upon global optimization of ~300 possible structures using DFT, and the possible candidates were generated by means of different manipulation of existing structures in mineral database. In chapter 3, we have shown that, our approach not only can produce the crystal structure of $ABW_2O_8$ compound quite accurately, but also for other stoichiometric material. The success in crystal structure prediction for existing materials lead us to claim that the predicted structures for the new materials should be accurate enough to be relied on the predicted opto-electronic properties.

The final critical step was to develop a method that can predict the phase stability during the synthesis process and high efficiency growth conditions. Initially, the existing materials were used to verify the newly developed method which was later employed to the predicted materials. This method predicts that at thermodynamic equilibrium, the formation of multi-phases-$CuSnW_2O_8$ and $ZnSnW_2O_8$ is highly probable. The role of presences of other phases may have beneficial/detrimental effects on photovoltaic/photocatalytic performances, and hence needs to be investigated, which we intend to pursue in our future works. However, in the present work, we have attempted to predict optimized growth conditions with help of defect calculation, expecting that would minimize and maximize (prohibit) the co-existence of secondary phases and formation of benign (detrimental) defects in the predicted materials. For $CuSnW_2O_8$, we have

presented two optimized growth conditions at which preferable p-type activity through Cu-vacancy ($V_{Cu}$) formation and minimization of the co-existence of unwanted secondary phases are easily achievable. It was further shown that the presence of $V_{Cu}$ in fact enhances the absorption rate in $CuSnW_2O_8$. In the case of $ZnSnW_2O_8$, we found that at least two secondary phases are probable to be co-existed with it at thermodynamic equilibrium growth conditions. If we intend to minimize the detrimental defects such as $Sn_W$, the growth conditions those have to be chosen would facilitate the co-existence of ZnO and $ZnWO_8$ formation. Under such conditions the formation of $V_O$ and $W_{Sn}$ would be probable as well, giving rise to n-type activity in $ZnSnW_2O_8$. These defects do not deteriorate optical absorption performance compared to pristine one; however, further investigation is needed to have deeper insight on the defects influencing photocatalytic performance of $ZnSnW_2O_8$.

# Chapter 8

## Future Research

At present, my current research has been devoted in predicting an affordable solar absorber material. The success of my current method can be extended to fill the void in other technological aspects e.g. spintronics. A novel prospect of the spintronics technology is the use of the orientation of the spin of an electron to encode information, for which spin polarized materials are needed. The topological insulators (TI) are the attractive candidates for spintronics as they at the nanoscale host a spin state of an electron on the surfaces. However, the lack of an affordable TI is prolonging the spintronics technology from being a reality. Therefore, I intend to extend my expertise on prediction of sustainable solar materials to that of an affordable topological insulator in future.

Once the new affordable material is predicted, the next challenge is to synthesize it. During the synthesis process, defects are inherent in a material. Further, unwanted phases may co-exist with primary material if the growth conditions are not well chosen. These defects/mixed-phases enhance or degrade the materials' properties. A suitable choice of growth conditions during the synthesis process can maximize the efficiency of the material of interest; however, determining such a high efficient growth conditions often involves trial-and-error. An effective prediction in this regard would not only do ensure the higher efficiency of the desired material, but also save time and cost. The method I have developed to predict high efficient growth conditions in dissertation research, intend to implement to the predicted TI.

Apart from the synthesis process, defects are also induced on the heterojunction interfaces while integrating nano materials with bulk counterparts in creating a material platform for an electronic device. These defects modify the materials electronic properties

as well. Understanding the formation and nature of those defects at the interfaces are prerequisite for better engineering and hence the better controlling of the electronic properties of a device. An ab-initio calculation of defects formation can shed light in this regard. However, it's a very challenging to predict the energetics of defects at hetero-interfaces precisely. This is often done through some computational modeling whose successes are very limited. In future, I am interested to devise an effective and universal approach of computational modeling to calculate defects energetics or other electronic properties such as band offset at the interfaces.

# Appendix A

## Electronic Properties of $CuBi_2O_4$ and α-$SnWO_4$

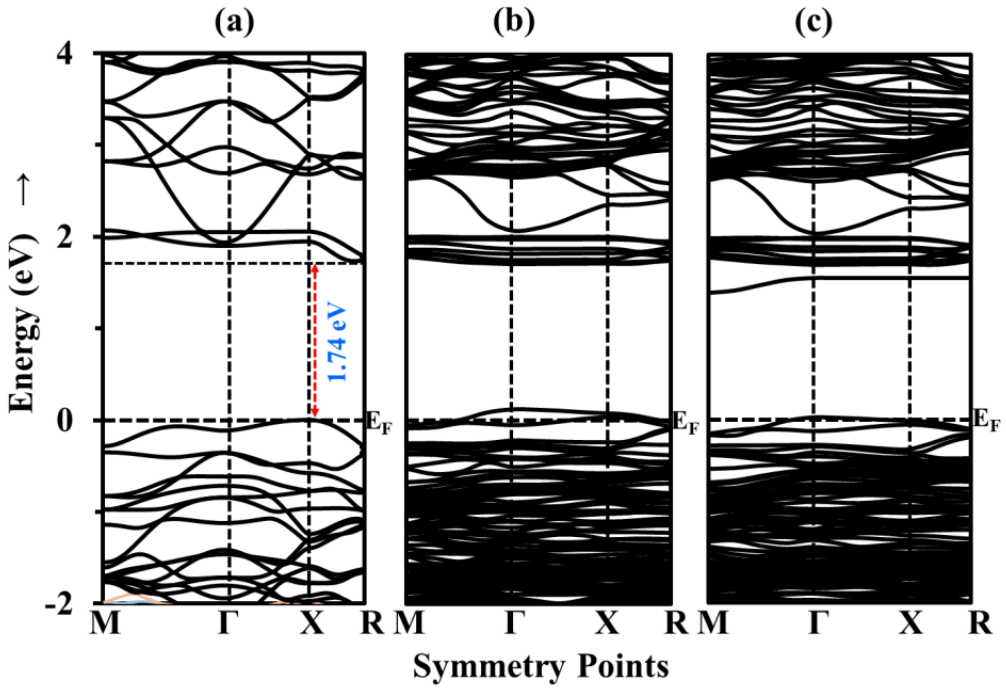


Figure 1 The DFT+U electronic band structures of a) pristine-$CuBi_2O_4$ b)$V_{Cu}$ - $CuBi_2O_4$ and c) $Cu_{Bi}$ - $CuBi_2O_4$.

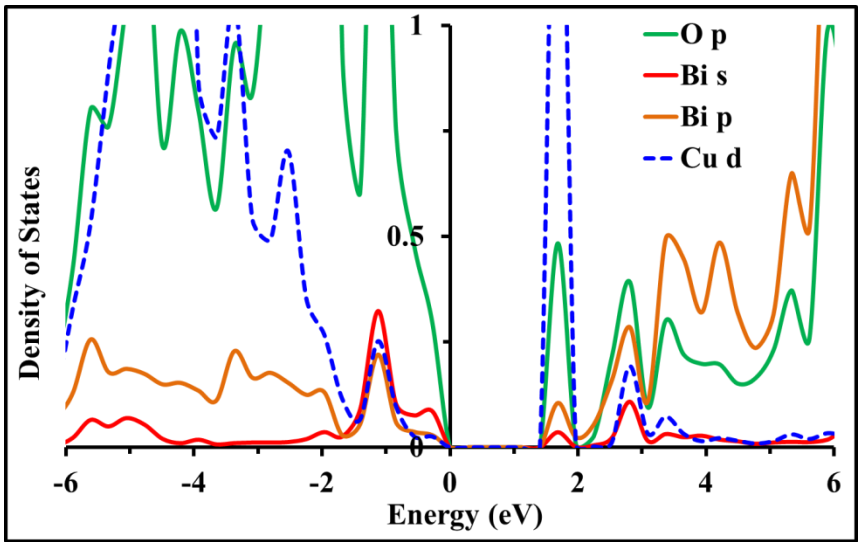


Figure 2 The DFT+U projected density of states (p-DOS) of $V_{Cu}$ - $CuBi_2O_4$.

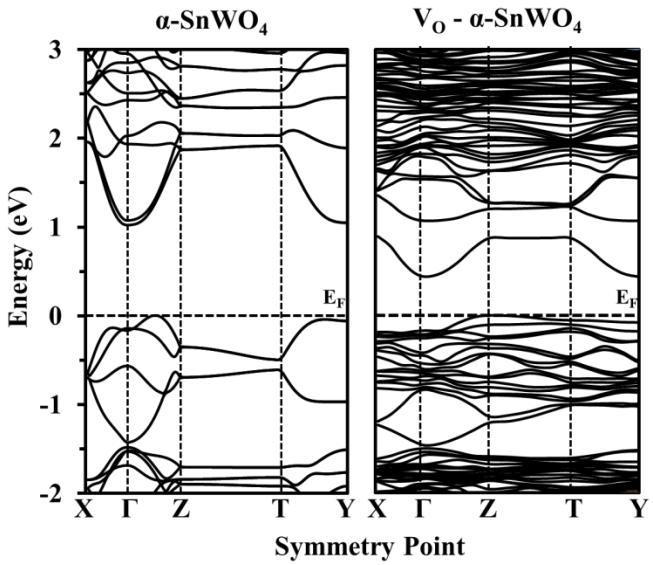


Figure 3 The DFT+U electronic band structures of (left) pristine-α-$SnWO_4$ and (right) $V_{Cu}$ – α-$SnWO_4$.

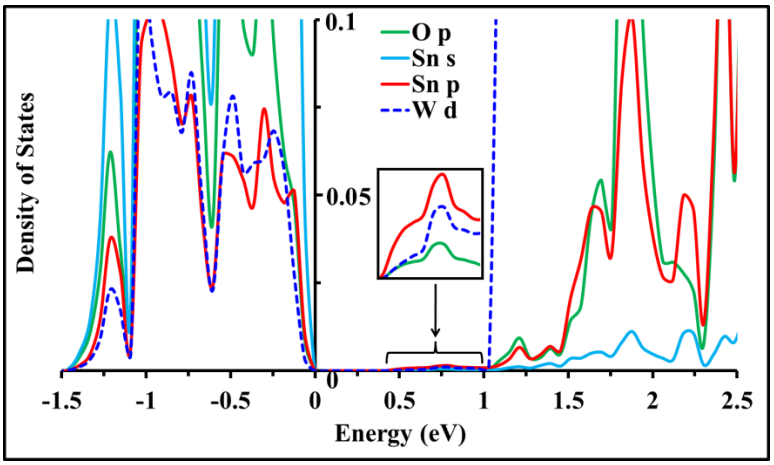


Figure 4 The DFT+U electronic band structures of (left) pristine-α-$SnWO_4$ and (right) $V_{Cu}$ – α-$SnWO_4$.

# Appendix B

## A Brief Study of $ANb_xO_y$ (A = Cu and Zn)

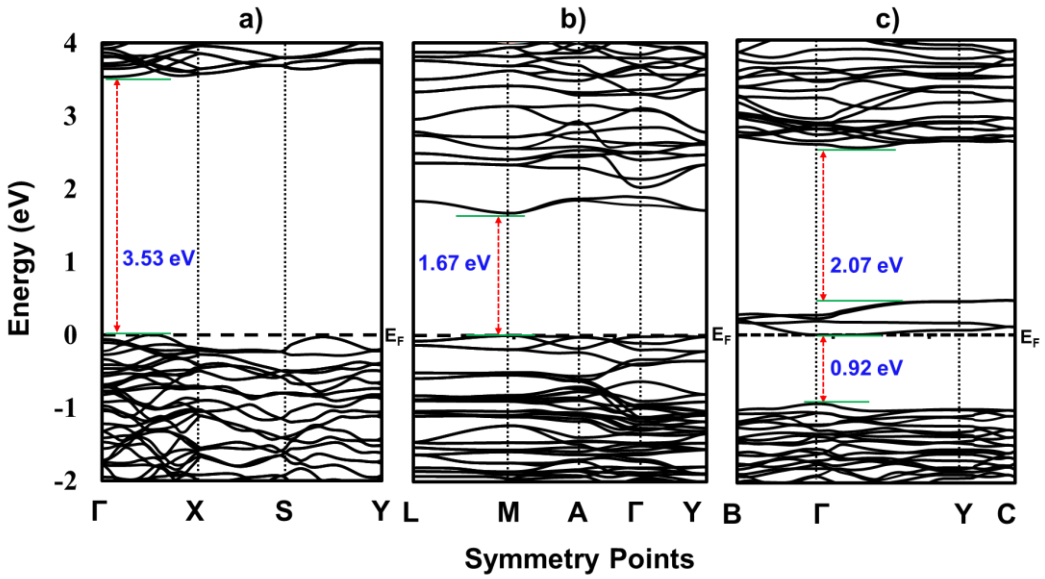


Figure 1 The DFT+U electronic band structures of (a) $ZnNb_2O_6$, (b) $CuNbO_3$, and (c) $CuNb_2O_6$.

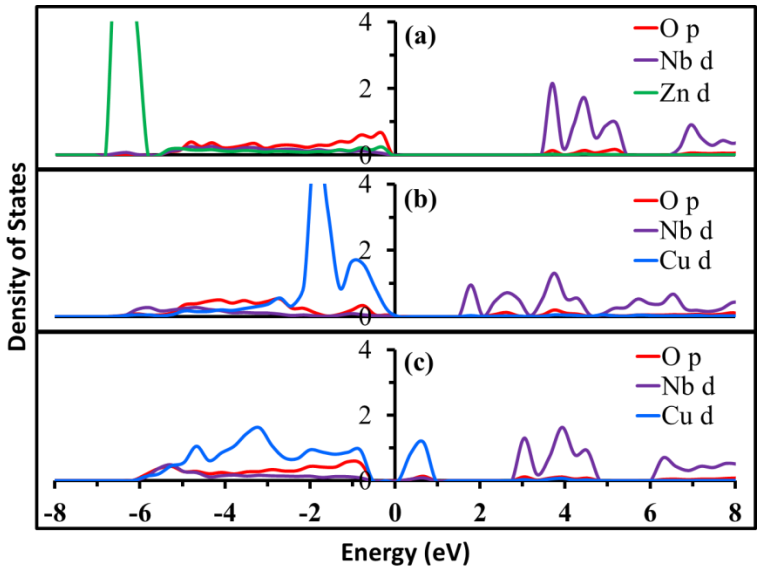


Figure 2 The DFT+U projected density of states (p-DOS) of (a) $ZnNb_2O_6$, (b) $CuNbO_3$, and (c) $CuNb_2O_6$.

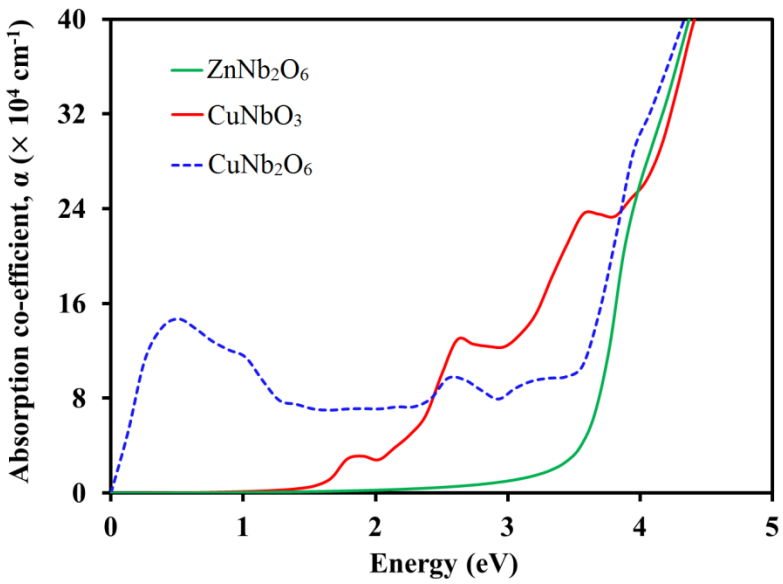


Figure 3 The DFT+U optical absorption of $ZnNb_2O_6$, $CuNbO_3$, and $ZnNb_2O_6$.

References

[1] G. Hautier, C. Fischer, V. Ehrlacher, A. Jain, and G. Ceder, Inorg. Chem. **50**, 656–663 (2011).

[2] A. Franceschetti and A. Zunger, Nature **402**, 60–63 (1999).

[3] A. Jain, S.P. Ong, G. Hautier, W. Chen, W.D. Richards, S. Dacek, S. Cholia, D. Gunter, D. Skinner, G. Ceder, and K.A. Persson, APL Mater. **1**, 011002 (2013).

[4] S. Curtarolo, W. Setyawan, G.L.W. Hart, M. Jahnatek, R. V. Chepulskii, R.H. Taylor, S. Wang, J. Xue, K. Yang, O. Levy, M.J. Mehl, H.T. Stokes, D.O. Demchenko, and D. Morgan, Comput. Mater. Sci. **58**, 218–226 (2012).

[5] W. Shockley and H.J. Queisser, J. Appl. Phys. **32**, 510 (1961).

[6] C. Janáky, K. Rajeshwar, N.R. De Tacconi, W. Chanmanee, and M.N. Huda, Catal. Today **199**, 53–64 (2013).

[7] M. Woodhouse, G.S. Herman, and B.A. Parkinson, Chem. Mater. **17**, 4318–4324 (2005).

[8] M. Woodhouse and B.A. Parkinson, Chem. Mater. **20**, 2495–2502 (2008).

[9] A. Walsh, Y. Yan, M.M. Al-Jassim, and S.-H. Wei, J. Phys. Chem. C **112**, 12044–12050 (2008).

[10] Y. Zhu, G. Chen, H. Ye, A. Walsh, C. Moon, and S.-H. Wei, Phys. Rev. B **77**, 245209 (2008).

[11] J. Da Silva, Y. Yan, and S.-H. Wei, Phys. Rev. Lett. **100**, 255501 (2008).

[12] P. Sarker, D. Prasher, N. Gaillard, and M.N. Huda, J. Appl. Phys. **114**, 133508 (2013).

[13] J. Maddox, Nautre **335**, 201 (1988).

[14] A.R. Oganov, editor , *Modern Methos of Crystal Structure Prediction*, 1st ed. (WILEY-VCH Verlag GmbH & Co. KGaA, Weinheim, 2011).

[15] H. Katayama-Yoshida, K. Sato, and T. Yamamoto, JSAP Int. **6**, 20–27 (2002).

[16] A.R. Oganov, editor , *Modern Methods of Crystal Structure Prediction* (WILEY-VCH Verlag & Co. KGaA, Weinheim, 2011).

[17] P. Sarker, M.M. Al-Jassim, and M.N. Huda, J. Appl. Phys. **117**, 035702 (2015).

[18] L.H. Thomas, Math. Proc. Cambridge Philos. Soc. **23**, 542–548 (1926).

[19] E. Fermi, Zeitschrift Für Phys. A Hadron. Nucl. **48**, 73–79 (1928).

[20] http://cmt.dur.ac.uk/sjc/thesis_ppr/node6.html.

[21] R. Jones and O. Gunnarsson, Rev. Mod. Phys. **61**, 689–746 (1989).

[22] G.D. Mahan, *Many-Particle Physics* (Plenum Press, New York and London, 1990).

[23] M.P. Marder, *Condensed Matter Physics* (John Wiley & Sons, 2000).

[24] P. Hohenberg, Phys. Rev. **136**, B864–B871 (1964).

[25] E. Engel and R.M. Dreizler, *Density Functional Theory*, 1st ed. (Springer Berlin Heidelberg, Berlin, Heidelberg, 2011).

[26] W. Khohn and L.J. Sham, Phys. Rev. **140**, A 1133– A 1138 (1965).

[27] W. Kohn and L.J. Sham, Phys. Rev. **140**, A1133–A1138 (1965).

[28] J.P. Perdew, J.A. Chevary, S.H. Vosko, K.A. Jackson, M.R. Pederson, D.J. Singh, and C. Fiolhais, Phys. Rev. B **46**, 6671–6687 (1992).

[29] D. Langreth and M. Mehl, Phys. Rev. B **28**, 1809–1834 (1983).

[30] A.D. Becke, J. Chem. Phys. **98**, 5648 (1993).

[31] B. Hammer and M. Scheffler, Phys. Rev. Lett. **74**, 3487–3491 (1995).

[32] E.I. Proynov, E. Ruiz, A. Vela, and D.R. Salahub, Int. J. Quantum Chem. **56**, 61–78 (1995).

[33] A.C. Scheiner, J.O.N. Baker, and J.A.N.W. Andzelm, J. Comput. Chem. **18**, 775–795 (1996).

[34] D. Hamann, Phys. Rev. Lett. **76**, 660–663 (1996).

[35] V. Ozoliņš and M. Körling, Phys. Rev. B **48**, 18304–18307 (1993).

[36] C. Filippi, D. Singh, and C. Umrigar, Phys. Rev. B **50**, 947–951 (1994).

[37] P.W. Anderson, Phys. Rev. **124**, 41–53 (1961).

[38] V.I. Anisimov, J. Zaanen, and O.K. Andersen, Phys. Rev. B **44**, 943–954 (1991).

[39] V.I. Anisimov, I. Solovyev, M. Korotin, M. Czyzyk, and G. Sawatzky, Phys. Rev. B **48**, 16929–16934 (1993).

[40] A.I. Liechtenstein, V.I. Anisimov, and J. Zaanen, Phys. Rev. B **52**, R5467–R5470 (1995).

[41] V.I. Anisimov, F. Aryasetiawan, and A.I. Lichtenstein, J. Phys. Condens. Matter **9**, 767–808 (1997).

[42] V.I. Anisimov, J. Zaanen, and O.K. Andersen, Phys. Rev. B **44**, 943–954 (1991).

[43] I. V. Solovyev, P.H. Dederichs, and V.I. Anisimov, Phys. Rev. B **50**, 16861–16871

(1994).

[44] S.L. Dudarev, G.A. Botton, S.Y. Savrasov, C.J. Humphreys, and A.P. Sutton, Phys. Rev. B **57**, 1505–1509 (1998).

[45] M. Cococcioni and S. de Gironcoli, Phys. Rev. B **71**, 1–16 (2005).

[46] J. Heyd, G.E. Scuseria, and M. Ernzerhof, J. Chem. Phys. **118**, 8207 (2003).

[47] J. Heyd, G.E. Scuseria, and M. Ernzerhof, J. Chem. Phys. **124**, 219906 (2006).

[48] J. Heyd and G.E. Scuseria, J. Chem. Phys. **121**, 1187 (2004).

[49] J. C. Slater, Phys. Rev. **51**, 846–851 (1937).

[50] P. M. Marcus, Int. J. Quantum Chem. **1**, 567–588 (1967).

[51] P. E. Blöchl, Phys. Rev. B **50**, 17953–17979 (1994).

[52] O. K. Andersen, Phys. Rev. B **12**, 3060–3083 (1975).

[53] G. Kresse and D. Joubert, Phys. Rev. B **59**, 1758–1775 (1999).

[54] P.E. Blöchl, Phys. Rev. **50**, 17953–17979 (1994).

[55] G. Kresse and J. Furthmüller, Phys. Rev. B **54**, 11169–11186 (1996).

[56] G. Kresse and J. Furthmüller, Comput. Mater. Sci. **6**, 15–50 (1996).

[57] J.P. Perdew, K. Burke, and M. Ernzerhof, Phys. Rev. Lett. **77**, 3865–3868 (1996).

[58] V.I. Anisimov, J. Zaanen, and O.K. Andersen, Phys. Rev. B **44**, (1991).

[59] F. Zhou, C.A. Marianetti, M. Cococcioni, D. Morgan, and G. Ceder, Phys. Rev. B **69**, 201101 (2004).

[60] M.V. Ganduglia-Pirovano, A. Hofmann, and J. Sauer, Surf. Sci. Rep. **62**, 219–270 (2007).

[61] A. Gali, T. Hornos, N. Son, E. Janzén, and W. Choyke, Phys. Rev. B **75**, 045211 (2007).

[62] F. Oba, A. Togo, and I. Tanaka, Phys. Rev. B **77**, 245202 (2008).

[63] J. To, A.A. Sokol, S.A. French, N. Kaltsoyannis, and C.R.A. Catlow, J. Chem. Phys. **122**, 144704 (2005).

[64] C. Patterson, Phys. Rev. B **74**, 144432 (2006).

[65] A.A. Sokol, S.A. French, S.T. Bromley, C.R.A. Catlow, H.J.J. van Dam, and P. Sherwood, Faraday Discuss. **134**, 267 (2007).

[66] A. Stroppa and G. Kresse, Phys. Rev. B **79**, 201201 (2009).

[67] A. Filippetti and N. Spaldin, Phys. Rev. B **67**, 125109 (2003).

[68] A. Lichtenstein and M. Katsnelson, Phys. Rev. B **57**, 6884–6895 (1998).

[69] S. Sharma, J. Dewhurst, N. Lathiotakis, and E. Gross, Phys. Rev. B **78**, 201103 (2008).

[70] K. Xiong, J. Robertson, and S.J. Clark, J. Appl. Phys. **99**, 044105 (2006).

[71] J.R. Weber, a. Janotti, P. Rinke, and C.G. Van de Walle, Appl. Phys. Lett. **91**, 142101 (2007).

[72] Y. Ma and M. Rohlfing, Phys. Rev. B **77**, 115118 (2008).

[73] M. Bockstedte, A. Marini, A. Gali, O. Pankratov, and A. Rubio, Mater. Sci. Forum **600-603**, 285–290 (2009).

[74] E. Batista, J. Heyd, R. Hennig, B. Uberuaga, R. Martin, G. Scuseria, C. Umrigar, and J. Wilkins, Phys. Rev. B **74**, 121102 (2006).

[75] S. Lany and A. Zunger, Model. Simul. Mater. Sci. Eng. **17**, 084002 (2009).

[76] P. Blöchl, O. Jepsen, and O. Andersen, Phys. Rev. B. Condens. Matter **49**, 16223–16233 (1994).

[77] H.J. Monkhorst and J.D. Pack, Phys. Rev. B **13**, 5188–5192 (1976).

[78] K. Momma and F. Izumi, J. Appl. Crystallogr. **41**, 653–658 (2008).

[79] F. Izumi and K. Momma, Solid State Phenom. **130**, 15–20 (2007).

[80] S. Chen, A. Walsh, X.-G. Gong, and S.-H. Wei, Adv. Mater. **25**, 1522–39 (2013).

[81] C. Persson, Y.-J. Zhao, S. Lany, and A. Zunger, Phys. Rev. B **72**, 035211 (2005).

[82] S. Zhang, S. Wei, A. Zunger, and H. Katayama-Yoshida, Phys. Rev. B **57**, 9642–9656 (1998).

[83] A. Nagoya, R. Asahi, R. Wahl, and G. Kresse, Phys. Rev. B **81**, 113202 (2010).

[84] C. Jacoboni, *Theory of Electron Transport in Semiconductors* (Springer Berlin Heidelberg, Berlin, Heidelberg, 2010).

[85] M.S. Dresselhaus, *Solid State Physics (Part II): Optical Properties of Solids* (n.d.).

[86] H. Akkus and A.M. Mamedov, J. Phys. Condens. Matter **19**, 116207 (2007).

[87] M. Fox, *Optical Properties of Solids* (Oxford University Press, 2001).

[88] S. Cabuk and S. Simsek, Cent. Eur. J. Phys. **6**, 730–736 (2008).

[89] M. Gajdoš, K. Hummer, G. Kresse, J. Furthmüller, and F. Bechstedt, Phys. Rev. B **73**,

1–9 (2006).

[90] A. Jain, S.P. Ong, G. Hautier, W. Chen, W.D. Richards, S. Dacek, S. Cholia, D. Gunter, D. Skinner, G. Ceder, and K.A. Persson, APL Mater. **1**, 011002 (2013).

[91] N.R. de Tacconi, H.K. Timmaji, W. Chanmanee, M.N. Huda, P. Sarker, C. Janáky, and K. Rajeshwar, Chemphyschem **13**, 2945–55 (2012).

[92] P. Sarker and M.N. Huda, Comput. Mater. Sci. **111**, 359–365 (2016).

[93] W. Koch and M.C. Holthausen, *A Chemist's Guide to Density Functional Theory*, 2nd ed. (Wiley-VCH Verlag GmbH, 2001).

[94] J.F. Dobson, K. McLennan, A. Rubio, J. Wang, T. Gould, H.M. Le, and B.P. Dinte, Aust. J. Chem. **54**, 513–527 (2001).

[95] Q. Wu and W. Yang, J. Chem. Phys. **116**, 515–524 (2002).

[96] E. Londero and E. Schröder, Phys. Rev. B - Condens. Matter Mater. Phys. **82**, (2010).

[97] D.O. Scanlon, A. Walsh, B.J. Morgan, and G.W. Watson, J. Phys. Chem. C **112**, 9903–9911 (2008).

[98] F. Corà, A. Patel, N.M. Harrison, C. Roetti, and C.R.A. Catlow, J. Mater. Chem. **7**, 959–967 (1997).

[99] D.O. Scanlon, G.W. Watson, D.J. Payne, G.R. Atkinson, R.G. Egdell, and D.S.L. Law, J. Phys. Chem. C **114**, 4636–4645 (2010).

[100] S. Grimme, J. Comput. Chem. **27**, 1787–1799 (2006).

[101] K. Govaerts, R. Saniz, B. Partoens, and D. Lamoen, Phys. Rev. B - Condens. Matter Mater. Phys. **87**, 1–7 (2013).

[102] T. Kerber, M. Sierka, and J. Sauer, J. Comput. Chem. **29**, 2088–2097 (2008).

[103] Y. Duan, Phys. Rev. B - Condens. Matter Mater. Phys. **77**, (2008).

[104] M.E. Foster and K. Sohlberg, Phys. Chem. Chem. Phys. **12**, 307–322 (2010).

[105] T. Bučko, J. Hafner, S. Lebègue, and J.G. Ángyán, J. Phys. Chem. A **114**, 11814–11824 (2010).

[106] H.J. Monkhorst and J.D. Pack, Phys. Rev. B **13**, 5188–5192 (1976).

[107] T. F. Krüger and Hk. Müller-Buschbaum, J. Alloy. Compd. **190**, L1–L3 (1992).

[108] A. Ditte, Ann. Chim. Phys. **27**, 145 (1882).

[109] A. Seko, A. Togo, F. Oba, and I. Tanaka, Phys. Rev. Lett. **100**, 045702 (2008).

[110] M. a Mäki-Jaskari and T.T. Rantala, Model. Simul. Mater. Sci. Eng. **12**, 33–41 (2004).

[111] G. Murken and M. Trömel, Zeitschrift Für Anorg. Und Allg. Chemie **397**, 117–126 (1973).

[112] K. Hasselbach, G. Murken, and M. Trömel, Zeitschrift Für Anorg. Und Allg. Chemie **397**, 127–130 (1973).

[113] M.A. Mäki-Jaskari and T.T. Rantala, Model. Simul. Mater. Sci. Eng. **12**, 33–41 (2004).

[114] A. Togo and I. Tanaka, Scr. Mater. **108**, 1–5 (2015).

[115] J. He, L. Sun, S. Chen, Y. Chen, P. Yang, and J. Chu, J. Alloys Compd. **511**, 129–132 (2012).

[116] T.K. Todorov, J. Tang, S. Bag, O. Gunawan, T. Gokmen, Y. Zhu, and D.B. Mitzi, Adv. Energy Mater. **3**, 34–38 (2013).

[117] H. Matsushita, T. Maeda, A. Katsui, and T. Takizawa, J. Cryst. Growth **208**, 416–422 (2000).

[118] J.J. Scragg, P.J. Dale, and L.M. Peter, Electrochem. Commun. **10**, 639–642 (2008).

[119] J.-S. Seol, S.-Y. Lee, J.-C. Lee, H.-D. Nam, and K.-H. Kim, Sol. Energy Mater. Sol. Cells **75**, 155–162 (2003).

[120] T. Tanaka, T. Nagatomo, D. Kawasaki, M. Nishio, Q. Guo, A. Wakahara, A. Yoshida, and H. Ogawa, in *J. Phys. Chem. Solids* (2005), pp. 1978–1981.

[121] S. Chen, A. Walsh, J.-H. Yang, X.G. Gong, L. Sun, P.-X. Yang, J.-H. Chu, and S.-H. Wei, Phys. Rev. B **83**, 125201 (2011).

[122] X.Q. Pan and L. Fu, J. Appl. Phys. **89**, 6048–6055 (2001).

[123] F. Lawson, Nature **215**, 955–956 (1967).

[124] D.N. Klushin, O.V. Nadinskaya, and K.G. Bogatina, J. Appl. Chem. USSR **32**, 284 (1959).

[125] JCPDS (International Center for Diffraction Data), (1997) 18.

[126] F. Gauzzi, B. Verdini, A. Maddalena, and G. Principi, Inorganica Chim. Acta **104**, 1–7 (1985).

[127] A.F. Holleman, N. Wiberg, and E. Wiberg, *Lehrbuch Der Anorganischen Chemie* (Walter de Gruyter, Berlin, 1995).

[128] M.S. Moreno, G. Punte, G. Rigotti, R.C. Mercader, A.D. Weisz, and M.A. Blesa, Solid State Ionics **144**, 81–86 (2001).

[129] S. Cahen, N. David, J.M. Fiorani, A. Maître, and M. Vilasi, Thermochim. Acta **403**, 275–285 (2003).

[130] H. Giefers, F. Porsch, and G. Wortmann, Solid State Ionics **176**, 199–207 (2005).

[131] J.P. Allen, D.O. Scanlon, S.C. Parker, and G.W. Watson, J. Phys. Chem. C **115**, 19916–19924 (2011).

[132] J.P. Allen, D.O. Scanlon, L.F.J. Piper, and G.W. Watson, J. Mater. Chem. C **1**, 8194 (2013).

[133] J. Heyd, G.E. Scuseria, and M. Ernzerhof, J. Chem. Phys. **118**, 8207 (2003).

[134] D.M. Adams, A.G. Christy, J. Haines, and S.M. Clark, Phys. Rev. B **46**, 11358–11367 (1992).

[135] M.S. Moreno and R.C. Mercader, Phys. Rev. B **50**, 9875–9881 (1994).

[136] W.J. Moore and L. Pauling, J. Am. Chem. Soc. **63**, 1392–1394 (1941).

[137] J. Pannetier and G. Denes, Acta Crystallogr. Sect. B Struct. Crystallogr. Cryst. Chem. **36**, 2763–2765 (1980).

[138] J. Geurts, S. Rau, W. Richter, and F.J. Schmitte, Thin Solid Films **121**, 217–225 (1984).

[139] Y. Ogo, H. Hiramatsu, K. Nomura, H. Yanagi, T. Kamiya, M. Hirano, and H. Hosono, Appl. Phys. Lett. **93**, 032113 (2008).

[140] L.Y. Liang, Z.M. Liu, H.T. Cao, Z. Yu, Y.Y. Shi, A.H. Chen, H.Z. Zhang, Y.Q. Fang, and X.L. Sun, J. Electrochem. Soc. **157**, H598 (2010).

[141] M.H.M. Reddy, S.R. Jawalekar, and A.N. Chandorkar, Thin Solid Films **169**, 117–126 (1989).

[142] W.K. Choi, H. Sung, K.H. Kim, J.S. Cho, S.C. Choi, H.-J. Jung, and S.K. Koh, J. Mater. Sci. Lett. **16**, 1551–1554 (1997).

[143] W.H.S. M.R. Soares, P.H. Dionísio, I.J.R. Baumvol, Thin Solid Films **214**, 6–16 (1992).

[144] M. Batzill and U. Diebold, Prog. Surf. Sci. **79**, 47–154 (2005).

[145] N.T. Hahn, V.C. Holmberg, B.A. Korgel, and C.B. Mullins, J. Phys. Chem. C **116**, 6459–6466 (2012).

[146] T. Arai, M. Yanagida, Y. Konishi, Y. Iwasaki, H. Sugihara, and K. Sayama, J. Phys. Chem. C **111**, 7574–7577 (2007).

[147] T. Arai, Y. Konishi, Y. Iwasaki, H. Sugihara, and K. Sayama, J. Comb. Chem. **9**, 574–581 (2007).

[148] R. Arpe and H. Müller-Buschbaum, Zeitschrift Für Anorg. Und Allg. Chemie **426**, 1–6

(1976).

[149] H.S. Park, C.-Y. Lee, and E. Reisner, Phys. Chem. Chem. Phys. **16**, 22462–22465 (2014).

[150] G. Sharma, Z. Zhao, P. Sarker, B.A. Nail, J. Wang, M.N. Huda, and F.E. Osterloh, (n.d.).

[151] I. Cho, C. Kwak, and D. Kim, J. Phys. Chem. C **113**, 10647–10653 (2009).

[152] A. Walsh, Y. Yan, M.N. Huda, M.M. Al-Jassim, and S.-H. Wei, Chem. Mater. **21**, 547–551 (2009).

[153] A. Walsh, S. Chen, S.-H. Wei, and X.-G. Gong, Adv. Energy Mater. **2**, 400–409 (2012).

[154] J. Paier, R. Asahi, A. Nagoya, and G. Kresse, Phys. Rev. B **79**, 115126 (2009).

[155] T.K. Todorov, K.B. Reuter, and D.B. Mitzi, Adv. Mater. **22**, E156–9 (2010).

[156] D.A.R. Barkhouse, O. Gunawan, T. Gokmen, T.K. Todorov, and D.B. Mitzi, Prog. Photovoltaics Res. Appl. **20**, 6–11 (2012).

[157] W. Wang, M.T. Winkler, O. Gunawan, T. Gokmen, T.K. Todorov, Y. Zhu, and D.B. Mitzi, Adv. Energy Mater. **4**, n/a–n/a (2014).

[158] I. Repins, M.A. Contreras, B. Egaas, C. DeHart, J. Scharf, C.L. Perkins, B. To, and R. Noufi, Prog. Photovoltaics Res. Appl. **16**, 235–239 (2008).

[159] J.J. Scragg, P.J. Dale, L.M. Peter, G. Zoppi, and I. Forbes, Phys. Status Solidi **245**, 1772–1778 (2008).

[160] S. Chen, J.H. Yang, X.G. Gong, A. Walsh, and S.H. Wei, Phys. Rev. B **81**, 245204 (2010).

[161] S. Delbos, EPJ Photovoltaics **3**, 35004Delbos, S. (2012). Kësterite thin films for p (2012).

[162] S. Chen, A. Walsh, X.-G. Gong, and S.-H. Wei, Adv. Mater. **25**, 1522–39 (2013).

[163] S. Chen, X.G. Gong, A. Walsh, and S.-H. Wei, Appl. Phys. Lett. **96**, 021902 (2010).

[164] B.G. Mendis, M.C.J. Goodman, J.D. Major, A. a. Taylor, K. Durose, and D.P. Halliday, J. Appl. Phys. **112**, 124508 (2012).

[165] H. Wang, Int. J. Photoenergy **2011**, 1–10 (2011).

[166] D.B. Mitzi, O. Gunawan, T.K. Todorov, K. Wang, and S. Guha, Sol. Energy Mater. Sol. Cells **95**, 1421–1436 (2011).

[167] W. Ki and H.W. Hillhouse, Adv. Energy Mater. **1**, 732–735 (2011).

[168] H. Katagiri, K. Jimbo, M. Tahara, H. Araki, and K. Oishi, MRS Proc. **1165**, 1165–M04–01 (2011).

[169] K. Tanaka, M. Oonuki, N. Moritake, and H. Uchiki, Sol. Energy Mater. Sol. Cells **93**, 583–587 (2009).

[170] A. Ennaoui, M. Lux-Steiner, A. Weber, D. Abou-Ras, I. Kötschau, H.-W. Schock, R. Schurr, A. Hölzing, S. Jost, R. Hock, T. Voß, J. Schulze, and A. Kirbs, Thin Solid Films **517**, 2511–2514 (2009).

[171] B. Shin, O. Gunawan, Y. Zhu, N.A. Bojarczuk, S.J. Chey, and S. Guha, Prog. Photovoltaics Res. Appl. **21**, 72–76 (2013).

[172] K. Tanaka, Y. Fukui, N. Moritake, and H. Uchiki, Sol. Energy Mater. Sol. Cells **95**, 838–842 (2011).

[173] S. Botti, D. Kammerlander, and M.A.L. Marques, Appl. Phys. Lett. **98**, 241915 (2011).

[174] D. Huang, Y.-J. Zhao, S. Li, C.-S. Li, J.-J. Nie, X.-H. Cai, and C.-M. Yao, J. Phys. D. Appl. Phys. **45**, 145102 (2012).

[175] P. Lukashev and W. Lambrecht, Phys. Rev. B **76**, 1–14 (2007).

[176] P. Li, S. Deng, L. Zhang, G. Liu, and J. Yu, Chem. Phys. Lett. **531**, 75–79 (2012).

[177] M. Huda, Y. Yan, S.-H. Wei, and M. Al-Jassim, Phys. Rev. B **78**, 195204 (2008).

[178] A. Janotti and C.G. Van de Walle, Phys. Rev. B **76**, 165202 (2007).

[179] D. Han, Y. Sun, J. Bang, Y. Zhang, H.-B. Sun, X.-B. Li, and S. Zhang, Phys. Rev. B **87**, 155206 (2013).

[180] D.R. Lide, editor , *CRC Handbook of Chemistry and Physics*, 84th ed. (CRC Press, Boca Raton, 2003).

[181] A. Nagaoka, K. Yoshino, H. Taniguchi, T. Taniyama, K. Kakimoto, and H. Miyake, Phys. Status Solidi **210**, 1328–1331 (2013).

[182] Y.-T. Zhai, S. Chen, J.-H. Yang, H.-J. Xiang, X.-G. Gong, A. Walsh, J. Kang, and S.-H. Wei, Phys. Rev. B **84**, 075213 (2011).

[183] K. Wang, B. Shin, K.B. Reuter, T. Todorov, D.B. Mitzi, and S. Guha, Appl. Phys. Lett. **98**, 051912 (2011).

[184] X. Fontané, L. Calvo-Barrio, V. Izquierdo-Roca, E. Saucedo, A. Pérez-Rodriguez, J.R. Morante, D.M. Berg, P.J. Dale, and S. Siebentritt, Appl. Phys. Lett. **98**, 181905 (2011).

[185] P.A. Fernandes, P.M.P. Salomé, and A.F. da Cunha, J. Alloys Compd. **509**, 7600–7606 (2011).

[186] A. Redinger, K. Hönes, X. Fontané, V. Izquierdo-Roca, E. Saucedo, N. Valle, A. Pérez-Rodríguez, and S. Siebentritt, Appl. Phys. Lett. **98**, 101907 (2011).

[187] J. Just, D. Lützenkirchen-Hecht, R. Frahm, S. Schorr, and T. Unold, Appl. Phys. Lett. **99**, 262105 (2011).

[188] V. Kosyak, N.B. Mortazavi Amiri, A. V. Postnikov, and M.A. Scarpulla, J. Appl. Phys. **114**, 124501 (2013).

[189] A. Nagoya, R. Asahi, and G. Kresse, J. Phys. Condens. Matter **23**, 404203 (2011).

[190] T. Minemoto, T. Matsui, H. Takakura, Y. Hamakawa, T. Negami, Y. Hashimoto, T. Uenoyama, and M. Kitagawa, Sol. Energy Mater. Sol. Cells **67**, 83–88 (2001).

[191] M. Banavoth, S. Dias, and S.B. Krupanidhi, AIP Adv. **3**, 082132 (2013).

[192] W. Wang, M.T. Winkler, O. Gunawan, T. Gokmen, T.K. Todorov, Y. Zhu, and D.B. Mitzi, Adv. Energy Mater. **4**, 1301465 (2014).

[193] Y.S. Lee, T. Gershon, O. Gunawan, T.K. Todorov, T. Gokmen, Y. Virgus, and S. Guha, Adv. Energy Mater. **5**, 1401372 (2015).

[194] D.B. Mitzi, O. Gunawan, T.K. Todorov, and D.A.R. Barkhouse, Philos. Trans. A. Math. Phys. Eng. Sci. **371**, 20110432 (2013).

[195] M. a. Green, Solid. State. Electron. **24**, 788–789 (1981).

[196] M.T. Winkler, W. Wang, O. Gunawan, H.J. Hovel, T.K. Todorov, and D.B. Mitzi, Energy Environ. Sci. **7**, 1029 (2014).

[197] T. Gershon, T. Gokmen, O. Gunawan, R. Haight, S. Guha, and B. Shin, MRS Commun. **4**, 159–170 (2014).

[198] K. Timmo, M. Altosaar, J. Raudoja, K. Muska, M. Pilvet, M. Kauk, T. Varema, M. Danilson, O. Volobujeva, and E. Mellikov, Sol. Energy Mater. Sol. Cells **94**, 1889–1892 (2010).

[199] M. Tsega and D.-H. Kuo, J. Alloys Compd. **557**, 142–146 (2013).

[200] J. Timo Wätjen, J. Engman, M. Edoff, and C. Platzer-Björkman, Appl. Phys. Lett. **100**, (2012).

[201] T. Gokmen, O. Gunawan, T.K. Todorov, and D.B. Mitzi, Appl. Phys. Lett. **103**, (2013).

[202] T. Gershon, B. Shin, T. Gokmen, S. Lu, N. Bojarczuk, and S. Guha, Appl. Phys. Lett. **103**, 4–7 (2013).

[203] S. Bag, O. Gunawan, T. Gokmen, Y. Zhu, T.K. Todorov, and D.B. Mitzi, Energy Environ. Sci. **5**, 7060 (2012).

[204] O. Gunawan, Y. Virgus, and K.F. Tai, Appl. Phys. Lett. **106**, 062407 (2015).

[205] O. Gunawan, T. Gokmen, and D.B. Mitzi, in *Copp. Zinc Tin Sulfide-Based Thin-Film Sol. Cells*, edited by K. Ito (John Wiley & Sons, Ltd., Chichester, UK, 2015), pp. 387–411.

[206] I. Repins, C. Beall, N. Vora, C. DeHart, D. Kuciauskas, P. Dippo, B. To, J. Mann, W.-C. Hsu, A. Goodrich, and R. Noufi, Sol. Energy Mater. Sol. Cells **101**, 154–159 (2012).

[207] B. Shin, O. Gunawan, Y. Zhu, N.A. Bojarczuk, S.J. Chey, and S. Guha, Prog. Photovoltaics Res. Appl. **21**, 72–76 (2013).

[208] M. Kumar, H. Zhao, and C. Persson, Thin Solid Films **535**, 318–321 (2013).

[209] A. Khare, B. Himmetoglu, M. Cococcioni, and E.S. Aydil, J. Appl. Phys. **111**, 123704 (2012).

[210] S. Chen, L.W. Wang, A. Walsh, X.G. Gong, and S.H. Wei, Appl. Phys. Lett. **101**, (2012).

[211] J. Ruiz-Fuertes, D. Errandonea, a. Segura, F.J. Manjón, Z. Zhu, and C.Y. Tu, High Press. Res. **28**, 565–570 (2008).

[212] N.R. de Tacconi, H.K. Timmaji, W. Chanmanee, M.N. Huda, P. Sarker, C. Janáky, and K. Rajeshwar, Chemphyschem **13**, 2945–55 (2012).

[213] A. Jain, G. Hautier, C.J. Moore, S. Ping Ong, C.C. Fischer, T. Mueller, K. a. Persson, and G. Ceder, Comput. Mater. Sci. **50**, 2295–2310 (2011).

[214] P. Sarker, M.M. Al-Jassim, and M.N. Huda, Appl. Phys. Lett. **107**, (2015).

[215] M. Aroyo, J. Perez-Mato, D. Orobengoa, E. Tasci, G. de la Flor, and A. Kirov, Bulg. Chem. Commun. **43**, 183–197 (2011).

[216] M.I. Aroyo, J.M. Perez-Mato, C. Capillas, E. Kroumova, S. Ivantchev, G. Madariaga, A. Kirov, and H. Wondratschek, Zeitschrift Für Krist. **221**, 15–27 (2006).

[217] M.I. Aroyo, A. Kirov, C. Capillas, J.M. Perez-Mato, and H. Wondratschek, Acta Crystallogr. A. **62**, 115–28 (2006).

[218] M.I. Aroyo, D. Orobengoa, G. de la Flor, E.S. Tasci, J.M. Perez-Mato, and H. Wondratschek, Acta Crystallogr. Sect. A, Found. Adv. **70**, 126–137 (2014).

[219] L. Yu and A. Zunger, Phys. Rev. Lett. **108**, 068701 (2012).

[220] M.A. Contreras, K. Ramanathan, J. AbuShama, F. Hasoon, D.L. Young, B. Egaas, and R. Noufi, Prog. Photovoltaics Res. Appl. **13**, 209–216 (2005).

[221] B.V. Van Zeghbroeck, *Principles of Semiconductor Devices* (University of Colorado, 2011).

## Biographical Information

Pranab Sarker has received his bachelor in physics from Department of Physics university of Dhaka, Bangladesh. Then he successfully completed master's degree in theoretical physics with specialization on condensed matter physics from Department of Theoretical Physics, university of Dhaka, Bangladesh. The title of his master's thesis was "A Theoretical Study of Surface Tension of Crude Oil". After graduation he started teaching physics at undergraduate level. It was a very enjoyable and memorable period of his life; however, he had to shorten the teaching career to start the most exciting and challenging phase of life as a Ph.D. student in the University of Texas at Arlington (UTA). He came to Department of physics, UTA in the fall of 2010, in quest of being engaged in cutting-edge researches in theoretical condensed matter physics. He joined to the group led by Prof. Muhammad N. Huda, which was engaged in discovering new sustainable solar energy materials in bid to meet ever-increasing energy, and to stop global warming. He embraced that challenge joining Dr. Huda's group and continued his unabated passion to work in theoretical condensed matter physics. He has earned another master's degree here in theoretical condensed matter physics. After that he continued the theoretical research on sustainable solar materials to chase the dream of being a humanitarian scientist since childhood. At the end of his Ph.D. degree he intends to be an independent researcher through postdoctoral experience, and being ended up an accomplished career by conveying the gathered knowledge and expertise over the years to the emerging scientists through teaching and mentoring.